EUROPEAN ORGANIZATION FOR NUCLEAR RESEARCH


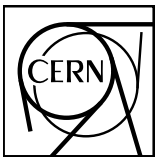


ALICE-PUBLIC-2023-004
04 September 2023

# Physics performance of the ALICE Forward Calorimeter upgrade

ALICE Collaboration *

**Abstract**

The ALICE Collaboration proposes to instrument the existing ALICE detector with a forward calorimeter system (FoCal), planned to take data during LHC Run 4 (2029–2032). The FoCal detector is a highly-granular Si+W electromagnetic calorimeter combined with a conventional sampling hadronic calorimeter, covering the pseudorapidity interval of $3.2 < \eta < 5.8$. The FoCal design is optimized to measure isolated photons at forward rapidity for $p_{\mathrm{T}} \gtrsim 4$ GeV/$c$, as well as neutral hadrons, vector mesons, and jets. Measurements of the inclusive distributions and correlations of these observables probe the structure of matter down to $x \sim 10^{-6}$, providing incisive tests of linear and non-linear QCD evolution at low $x$. This document presents current projections of the FoCal measurement performance for these observables.



*See Appendix C for the list of collaboration members

## Contents

**1 Introduction** **4**

**2 Design and simulations** **5**
2.1 FoCal design overview . . . . . 5
2.2 Simulations . . . . . 5
2.3 Reconstruction . . . . . 7
2.4 MC matching . . . . . 10

**3 Calorimetry performance** **11**
3.1 Calibration . . . . . 11
3.2 Response to electrons . . . . . 12
3.3 Response to charged hadrons . . . . . 13
3.4 Response to photons . . . . . 14

**4 Isolated and direct photon measurements** **17**
4.1 Background rejection . . . . . 17
4.1.1 Isolation . . . . . 17
4.1.2 Invariant mass tagging . . . . . 19
4.1.3 Shower-shape tagging . . . . . 19
4.2 Photon reconstruction efficiency . . . . . 20
4.3 Physics performance of FoCal isolated prompt photon measurements . . . . . 22
4.3.1 Statistical uncertainties . . . . . 23
4.3.2 Systematic uncertainties . . . . . 23
4.3.3 Nuclear modification of inclusive prompt–photon production: $R_{\mathrm{pPb}}$ . . . . . 24

**5 Neutral mesons** **27**
5.1 Reconstruction in single $\pi^0$ events . . . . . 27
5.2 Measurement of $\pi^0$, $\eta$, and $\omega$ in pp collisions . . . . . 30
5.3 Pileup effects . . . . . 33

**6 Jets** **36**
6.1 Jet reconstruction . . . . . 36
6.2 Geometric considerations . . . . . 37
6.3 Single-particle jet showers . . . . . 38
6.4 Jet response in pp collisions . . . . . 39
6.5 Neutral Energy Fraction . . . . . 40

**7 Di-hadron correlations** **44**

**8 Photon-hadron correlations** **50**
8.1 Measurement of raw correlation function and projection to full luminosity . . . . . 50
8.2 Extraction of direct photon-$\pi^0$ correlations . . . . . 53

**9 Vector meson photoproduction in ultra-peripheral collisions** **55**

**10 Summary** **60**

**References** **61**

**A Event generators** **65**

**B Clusterization algorithm performance** **65**
B.1 Single-photon performance . . . . . 65
B.2 Neutral pion performance . . . . . 68

**C The ALICE Collaboration** **69**

## 1 Introduction

This note presents the projected physics performance of the ALICE Forward Calorimeter (FoCal) upgrade, which will be installed during the LHC Long-Shutdown 3 (LS3) and take data during LHC Run 4 [1].

Due to the non-Abelian nature of QCD, the gluon density of matter is expected to saturate at low momentum fraction $x$, and QCD evolution is expected to be non-linear. FoCal will explore these novel phenomena, probing the low-$x$ structure of matter and the nature of QCD evolution through forward measurements of direct photons, neutral mesons, vector mesons, jets, Z-bosons, and their correlations, in hadronic pp and p–Pb collisions and in ultra-peripheral p–Pb and Pb–Pb collisions [2].

The FoCal design is optimized for this program. FoCal is a highly-granular Si+W electromagnetic calorimeter (FoCal-E) combined with a conventional sampling hadronic calorimeter (FoCal-H), covering pseudorapidity interval $3.4 < \eta < 5.5$ over full azimuth and $3.2 < \eta < 5.8$ with partial azimuthal coverage. The most stringent detector performance constraint in this program is imposed by the forward measurement of direct photons at low $p_{\mathrm{T}}$, which requires excellent discrimination of single-photon electromagnetic (EM) showers from merged EM showers arising from neutral meson decays. This is achieved by excellent spatial resolution in the separation of adjacent showers from $\pi^0$ decays, and by placing the front face of the detector 7 m from the interaction point, with inner radius about 5 cm from the beam line. Additional discrimination is provided by good FoCal-H energy resolution, and good linearity for photon isolation. These requirements result then also in good performance for jets, $\pi^0$ and $\eta$, quarkonia, $\mathrm{Z}^0$ bosons, and other observables.

This note is a companion to Ref. [2], which describes the FoCal physics program and its context relative to other current and planned facilities and experiments. The performance presented in this note represents the collaboration's assessment of FoCal performance at the time of preparing the Technical Design Report (TDR) of FoCal. It may be updated (or subsequent notes will be published), as new studies provide further insight into the FoCal physics performance.

Performance projections in this note assume that the integrated luminosity $\mathscr{L}_{\mathrm{int}}$ that will delivered during Run 4 is 100 $\mathrm{pb}^{-1}$ for pp collisions at $\sqrt{s} = 14\ TeV$, 300 $\mathrm{nb}^{-1}$ for p–Pb collisions at $\sqrt{s_{\mathrm{NN}}} = 8.8$ TeV split equally between the p–Pb and Pb–p beam configurations, about 3 $\mathrm{pb}^{-1}$ for pp collisions at the same energy, and 7 $\mathrm{nb}^{-1}$ for Pb–Pb collisions at 5.5 TeV.

This note is organized as follows. Section 2 provides details on the detector design, Monte-Carlo simulations, and reconstruction. Section 3 discusses the calibration procedures employed to go from simulated hits in the detector sensitive material to actual measured energy and basic performance of the calorimeter. Section 4, 5, and 6 discuss the physics performance expected for photons, neutral mesons, and jets, respectively. Sections 7 and 8 present the performance for di–hadron and $\gamma_{\mathrm{dir}}$–$\pi^0$ correlations. Section 9 presents the performance of measurements in ultra-peripheral collisions.

## 2 Design and simulations

### 2.1 FoCal design overview

The location of the FoCal is on the A-side of the experimental setup outside of the ALICE solenoid and in front of the compensator magnet, where there is sufficient space longitudinally (about 1.5 m) to place both the electromagnetic (FoCal-E) and hadronic (FoCal-H) calorimeters. The transverse size of the front-face of the calorimeters is roughly $90 \times 90$ cm$^2$, covering a pseudorapidty range of $3.2 < \eta < 5.8$ at $z = 7$ m. The transverse extent of the calorimeters at this position is not severely limited by integration issues. However, for safety reasons the transverse size of the calorimeter cannot exceed 120 cm.

FoCal-E is designed as a Si+W sampling calorimeter, in order to maintain a compact setup with a small effective Molière radius, and with a fine lateral granularity readout [1]. Due to the longitudinal boost at forward angles the single-particle energy is large and the constant term dominates the resolution; its value should be below 5% [1]. This can be achieved with a sampling layer thickness of $\approx 1\ X_0$. Tungsten is chosen as absorber due to its small Molière radius $R_{\mathrm{M}}$ and radiation length $X_0$, with values of $R_{\mathrm{M}} = 9\,\mathrm{mm}$ and $X_0 = 3.5\,\mathrm{mm}$. A total depth of around $20\ X_0$ is needed to provide sufficient linearity at large energy, leading to a total depth of about 20 cm, which includes also the necessary readout electronics and services.

The FoCal-E detector is a Si+W sampling calorimeter with hybrid design which uses two different Si readout technologies:

- 18 pad layers, with silicon pad sensors of transverse cell sizes of $1\,\mathrm{cm}^2 \approx R_{\mathrm{M}}^2$; readout with the HGCROC chip [3], which digitizes the analog signals providing accurate amplitude and time, as well as trigger information.
- 2 pixel layers, with digital readout and a cell size of $\approx 30 \times 30\,\mu\mathrm{m}^2$, i.e. much smaller than the Molière radius, using the ALPIDE MAPS and adapted readout from the ITS [4].

The data obtained in each layer will be read out individually. The two pixel layers are positioned at the 5th and 10th layer. Optimization of the positioning of the pixel layers requires a balance between the spatial separation of two showers, for which it is better to sample the shower early in its development, and energy resolution of the individual showers in the overlapping pair. The latter is better around the shower maximum, which depends on the energy of the particles.

FoCal-H, which is placed directly behind FoCal-E, is a conventional sampling hadronic calorimeter with similar transverse extent as FoCal-E, and a length of $\Delta z \sim 1.1\,\mathrm{m}$. FoCal-H has transverse but not longitudinal segmentation. The energy resolution requirements of FoCal-H are moderate. Due to the boost at very forward rapidity, the resolution is determined primarily by the constant term. The planned design foresees a "spaghetti- type" (scintillator fibers) calorimeter. The absorber material is composed of copper tubes with an inner radius of 1.1 mm and outer radius of 2.5 mm, with scintillator fibers running through the whole length of the tubes. Depending on the filling fill factor that can be achieved FoCal-H will have depth of about 5–6 nuclear interaction lengths ($\lambda_{\mathrm{int}}$).

### 2.2 Simulations

In order to assess FoCal performance for various physics observables, as described in the later sections, a simulation chain based on ALICE software and resources is used. The chain consists of a physics event generator, a detector model, a particle transport model, and reconstruction from raw signals (hits) to high-level physics analysis objects, such as energy calibrated clusters. The running of the whole chain is done using existing ALICE software packages which rely on AliRoot [5], together with a dedicated software package which implements FoCal geometry for simulations and the algorithm required to obtain reconstructed and calibrated clusters out of the hits simulated by GEANT3 [6].[1] Both the simulation and

[1] Using GEANT4 [7] simulations is under development, and differences in the performance will be studied in the future.

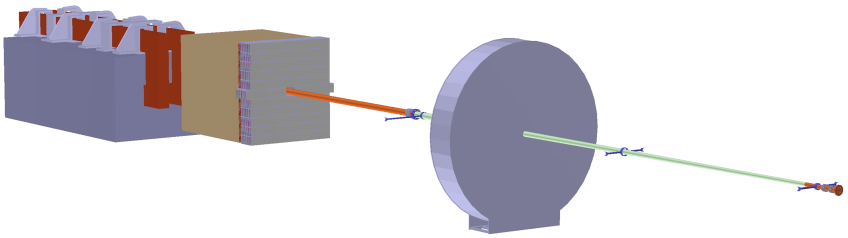

**Fig. 1:** FoCal geometry implemented in the ALICE simulation at 7 m from the interaction point and in front of the compensator magnet. For visibility, the figure shows only the details of the beam pipe, the FIT-A detector, FoCal, and the compensator magnet.

reconstruction parts are run on the ALICE grid infrastructure. Details on the event generators used in the note are given in Sec. A.

The evaluation of the FoCal performance utilizes both single-particle simulations which are uniform in $p_{\mathrm{T}}$ and $\eta$, and full event simulations based on the PYTHIA [8] and HIJING [9] event generators for pp, p–Pb, and Pb–Pb collisions. An idealized FoCal geometry based on the description in Sec. 2.1 was implemented in AliRoot. The FoCal detector is positioned at $z = 7$ m from the interaction point, as shown in Fig. 1. The detector is implemented with a nearly square transverse shape, with side length of $d = 0.9$ m, and with a square opening of dimension $5 \times 5$ cm$^2$ in the center for the beam pipe. The resulting rapidity coverage is approximately $3.2 < \eta < 5.8$ with the range $3.4 < \eta < 5.5$ having full azimuthal coverage.

**Table 1:** Material components of a FoCal-E pixel layer included in the simulation

| Material | Thickness (cm) |
|---|---|
| W alloy (94% W) | 0.35 |
| Aluminium carrier | 0.2 |
| Sensitive silicon sensor | 0.003 |
| Insensitive silicon | 0.047 |
| Air | 0.25 |
| Total | 0.85 |

Longitudinally, FoCal-E consists of 20 layers. Each layer includes a sheet of tungsten with a thickness of 3.5 mm. The total thickness of each layer is 8.5 mm, which includes the tungsten sheet, the sensitive silicon, insensitive supporting materials and a layer of air, reserved for services. To save computing time, the two pixel layers are each divided into pixels with a granularity of $50 \times 50$ μm$^2$ (i.e. almost factor 2 larger than the granularity of the ALPIDE pixels). At reconstruction they are further summed into $0.5 \times 0.5$ mm$^2$ cells or macro-pixels. No explicit simulation of charge diffusion and sharing between pixels is implemented, but to simulate the fluctuations in the deposited charge, the sensitive layer has a thickness of 30 μm (supported by a "bulk" of 470 μm Si).

**Table 2:** Material components of a FoCal-E pad layer included in the simulation

| Material | Thickness (cm) |
|---|---|
| W alloy (94% W) | 0.35 |
| PCB | 0.16 |
| Sensitive silicon sensor | 0.03 |
| Copper | 0.014 |
| Air | 0.296 |
| Total | 0.85 |

The pixel layers are located at depths of 5 $X_0$ and 10 $X_0$. As detailed in Tab. 1, besides the silicon material, each pixel layer includes two layers of 1 mm thick aluminium carrier in front and behind the silicon and

about 2.5 mm of air. The pad layers are instrumented with silicon pad readout. As detailed in Tab. 2, the silicon sensitive material has a thickness of 300 $\mu$m placed between two layers of Printed Board Circuit material (PCB) of 0.8 mm each. Additionally, each pad layer includes a 140 μm thick sheet of copper and about 3 mm of air, reserved for services.

In the transverse plane, FoCal-E has $2 \times 11$ modules, spanning a transverse size of about $90 \times 90$ cm$^2$, with each module having a transverse size of about $45 \times 8$ cm$^2$. The GEANT detector model includes the expected dead areas for both the pixel and pad layers. The modules are separated by a distance of 0.2 mm in the $x$-direction and 8 mm in the $y$-direction. The 8 mm distance between neighboring modules, which constitutes the largest dead area, is simulated as a rectangular aluminum volume representing a cooling plate. In the pixel layers, each module is divided into $15 \times 3$ regions which stand for the ALPIDE sensors. The sensors are placed starting with an offset in $x$ of 1.2 cm from the inner edge of each module and a 0.9 mm offset in the $y$ direction. The pad modules include $1 \times 5$ pad wafers, with each wafer containing $9 \times 8$ square pads each of an area of 1 cm$^2$. Each wafer has a skin of 2 mm to accommodate the guard ring of the sensor and safety distance between the sensors.

The implementation of FoCal-H consists of capillary tubes made of copper, with an inner diameter of 1.1 mm, an outer diameter of 2.5 mm, and a length of 110 cm, filled with a scintillator fiber of diameter 1 mm. These tubes are stack in a hexagonal pattern inside a $6.55 \times 6.55$ cm$^2$ copper module with a thickness of 3 mm. FoCal-H comprises $15 \times 15$ modules, with the module in the center removed to accommodate the beam pipe.

To save computational cost, we also consider a sandwich-type (scintillator plates) design, as in Ref. [1]. The sandwich implementation of FoCal-H in the simulation consists of 34 layers of 3 cm Pb layers interleaved with 0.2 cm scintillator as the sensitive material. The transverse segmentation in the simulation is $2.5 \times 2.5$ cm$^2$, and the simulated hits are summed longitudinally per tower. While the spaghetti-type design is being developed for the final FoCal design, the performance studies in this note are based mostly on the the sandwich-type design. This is done because simulations with the spaghetti-type FoCal-H are significantly more computationally expensive than for the sandwich-type FoCal-H, which would limit the simulated data-set for analysis. As reported below, it was checked that the difference in the designs does not have a large effect on the performance results reported in this note. If anything, the performance of the simulated sandwich design for lower energies is worse than that of the planned spaghetti design.

Although the reconstruction chain includes a digitization step, at the moment no electronics response effects or triggers were implemented in the simulations. Implementation of these effects is currently in progress. However, preliminary test beam results show good agreement with simulations for shower energies above 100 GeV, suggesting that implementing the electronic response functions will not change the performance assessment significantly.

The beam pipe, the instrumentation along the beamline, and all Run 4 detectors located between the interaction point and FoCal (notably the Fit-A detector [10]), are implemented in the GEANT model, to provide a realistic simulation of the material upstream of FoCal, as already described in Ref. [1].

### 2.3 Reconstruction

The simulated signals are based on the modeling of the shower development and the energy deposition by GEANT3. No additional detector response simulation or smearing is introduced since their effects are expected to be negligible for high-energy photons and hadrons at forward rapidity, as suggested by the beam tests of FoCal prototypes [11]. In the case of FoCal-E, an improvement which is under development is the charge diffusion in the pixel layers. In the current simulations the cluster size for a secondary track from the shower is essentially one pixel, though it is larger in practice. This effect was studied in detail in the test beam analysis with the pixel detector prototype. It mainly affects the shower profile very close to the shower axis and is not expected to degrade the two-shower separation power. Noise effects are

important only for low energy showers, and therefore have negligible impact on forward measurements where shower energies are large ($> 50$ GeV).

The analog readout of the pad layers uses the energy deposition generated by GEANT3 directly as the detector signal, while the signals in the pixel layers are digitized (any signal above a threshold of 4 keV is counted as a pixel hit).

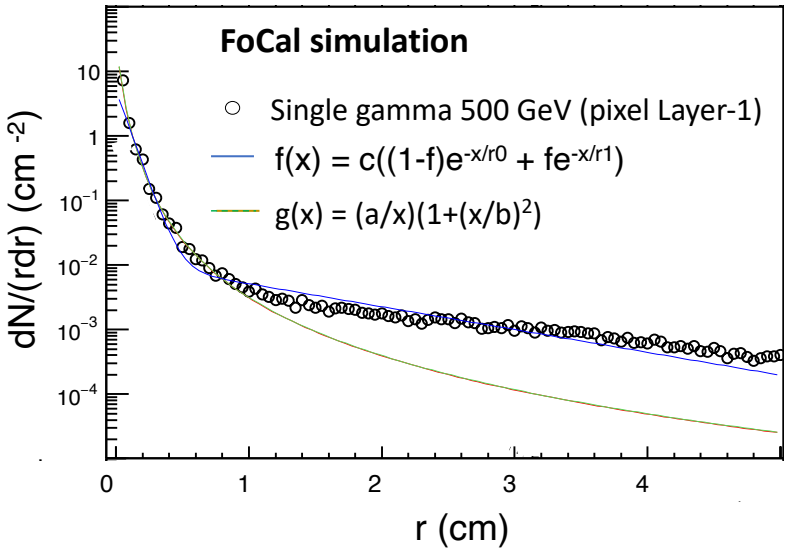


**Fig. 2:** The typical shower shape, $\mathrm{d}N/r\mathrm{d}r$ (where, $r$ is the radial distance from the seed to the neighboring cells), of 500 GeV photons for the first pixel layer (at position 5) fitted with the double exponential $f(x)$ and Cauchy $g(x)$ distributions. The parameters obtained from $f(x)$ are used in the clustering.

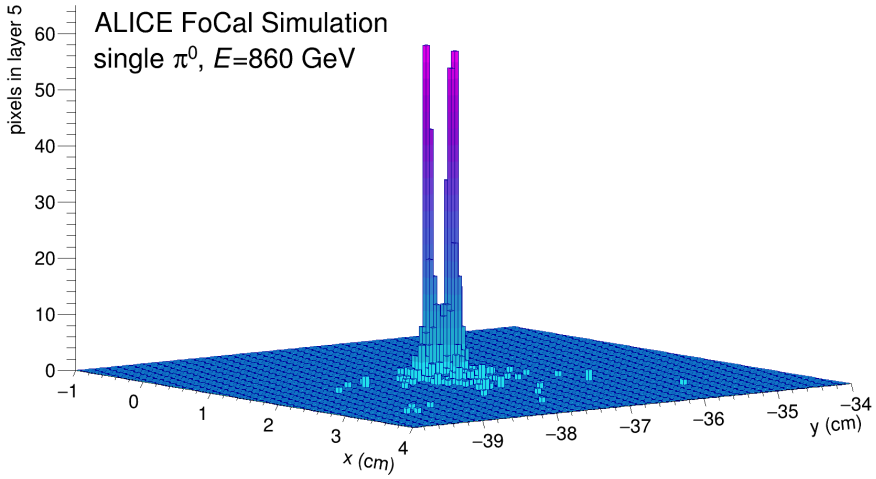


**Fig. 3:** Event display for a resolved single $\pi^0$ event with an energy of 860 GeV. The distribution shows the number of fired pixels in layer 5 as a function of the transverse coordinates, zoomed into the region where the $\pi^0$ hits FoCal.

A clustering algorithm is then applied to the simulated detector signals. Logically, the detector signals are first grouped into 6 segments. Each pixel layer itself forms a segment, while the information from layers 1–4, 6–9, 11–15 and 16–20, respectively, form a pad segment. The algorithm, which is described in

detail in Ref. [1], has been developed to run both on the low (pad) and high (pixel) granularity segments, and can be applied to high-occupancy Pb–Pb collisions as well as pp collisions. For Pb–Pb collisions, more restrictive parameter settings are used.

The clustering algorithm uses grids of equally spaced cells. Although the clustering procedure can be applied for every layer, in the analyses reported here the clustering is applied per segment. The cells are constructed from deposited hits, which are in turn obtained by summing hits which occur in the spatial range of a given cell. The size of the cells are 1 $cm^2$ in the pad layers and $500\times500$ $\mu m^2$ in the pixel segments. In the pad segments, the cell energy is obtained by summing the energy in all the layers belonging to the segment.

The procedure starts by finding clusters in each segment independently, and consists of a few steps. Firstly, cluster seeds are found from an energy-sorted list of cells, using only the front three segments. Only cells exceeding a minimum energy threshold (*SeedThreshold*) are considered as a seed. A minimum distance between cluster seeds (*MinRing*) is also imposed at this stage. For each seed, all the cells within the cluster radius (*MaxRing*) are summed to form a cluster. The creation, merging, and splitting of the clusters is based on weights assigned by seeds to all nearby cells. These weights are calculated using a parameterised shower shape for each segment, based on a double exponential function which has been fitted to single-photon simulations (see Fig. 2). The weights are proportional to the energy of the seed and depend on the distance between the cell and the seed. For the back three FoCal-E segments, so-called pre-seeds are used, i.e. seed positions that are determined by clusters found in the front segments. Seeds created in such a way cannot be rejected during the clusterization procedure. The parameters *MinRing*, *MaxRing*, *SeedThreshold*, and the 3 parameters for the shower shape parametrisation are tuned to obtain a good efficiency and a reasonably low fake rate due to shower splitting.

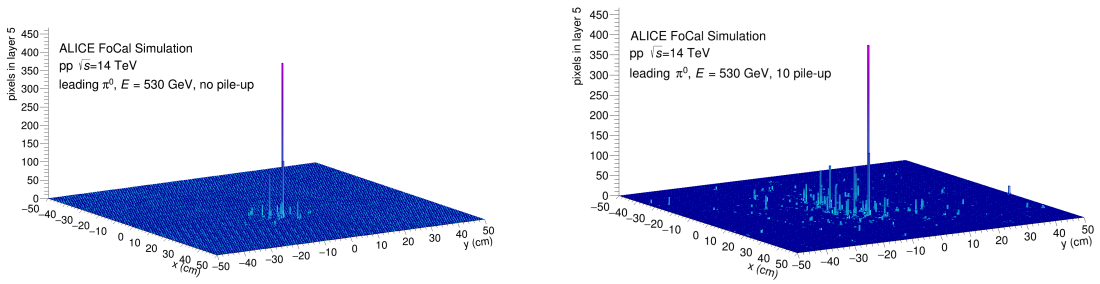


**Fig. 4:** Event display showing a pp collision with a leading $\pi^0$ of 530 GeV. The distribution shows the number of fired pixels in layer 5 as a function of the transverse coordinates. Left panel shows only the triggered pp collision and the right panel shows the same collision but with 10 embedded pileup minimum bias pp collisions.

After the clusters have been found in each of the segments, they are combined into full-detector clusters. The algorithm first loops over the pad layer segments separately. The clusters found in the different pad segments are matched and combined into full-depth pad clusters. Then, the clusters in the individual pixel layers are also matched and combined into summed pixel clusters. In the final step, the summed pixel clusters are used to separate showers that cannot be distinguished in the pad segments: a geometrical matching of the pixel and pad clusters is performed and if more than one pixel cluster is found in the same area as a pad cluster, the pad cluster is split into the corresponding number of pixel clusters, with the energy partitioned according to the relative energies of the clusters found in the pixel layers. The final shower position is calculated as the average of the positions found in the two pixel layers.

To illustrate the reconstruction performance for separating photon showers from $\pi^0$ decays, Fig. 3 shows an event display of a single $\pi^0$ measured in FoCal-E. The two-dimensional distribution zoomed in the region where the $\pi^0$ hits FoCal shows the number of fired pixels in the 5th FoCal-E layer. Furthermore,

Fig. 4 shows an event display of a single pp collision at $\sqrt{s} = 14$ TeV which contains an energetic $\pi^0$ (left panel) and the same event but with 10 minimum bias pp events superimposed (right panel), to illustrate the effect of pileup (see Sec. 5 for more details on the expected pileup).

Details on the performance of this clusterization algorithm applied to single photon box simulations are given in Appendix B. The clustering algorithm and its parameters will be improved in the future to take into account dead regions in the readout, and to adjust for different analysis purposes.

### 2.4 MC matching

In order to assess the resolution of various quantities, and to estimate the reconstruction efficiency for a given object, a procedure for the matching of the reconstructed object (detector level) to the corresponding object simulated by the physics generator (generator level) is necessary. This procedure is often called MC matching.

For clusters, the matching procedure has typically two steps. The first step identifies the closest primary or secondary MC particle to the cluster, based on the distance in the transverse plane between the cluster position and the position where the MC particle intersects the transverse plane at the longitudinal ($z$) position of the cluster.

As an optional second step, depending on the type of particle to be matched, if the closest MC particle as determined in the first step is a secondary particle generated in material or is a decay product, the particle history is followed using the mother–daughter relationship, down to the point where certain criteria are met. Typical criteria include finding the primary particle, a mother particle of a specified species to differentiate between physics processes, or finding a secondary particle generated in material upstream of FoCal (usually to identify converted photons before reaching FoCal).

In the case of jets, the matching is done between reconstructed jets at the detector and generator levels by requiring that the matched detector–generator jet pair has a phase space separation $\Delta R = \sqrt{\Delta\varphi^2 + \Delta\eta^2} < 0.6$. In the case of multiple matches, the jet with smallest value of $\Delta R$ is selected.

There are ongoing developments which will provide MC particles matched to each cluster already during the reconstruction, based on the GEANT3 information of the hits contributing to a given cluster. This will provide an unambiguous matching procedure, and will allow accurate allocation of the energy of contributing particles to overlapping showers.

# 3 Calorimetry performance

## 3.1 Calibration

Calibration of the MC detector-level response of the calorimeter is carried out using single mono-energetic charged pions and electrons, which are generated using a box generator that covers the entire detector acceptance. The electrons will deposit most of their energy in FoCal-E, with a small fraction in FoCal-H. The charged pions deposit most of their energy in FoCal-H and have large fluctuations of the position, where the shower is initiated, which can occur both in FoCal-E and FoCal-H as illustrated in Fig. 5. The energy is calibrated by determining the scaling factors for a linear combination of FoCal-E and FoCal-H shower energies,

$$E_{\mathrm{tot}} = \alpha E_{\mathrm{em}} + \beta E_{\mathrm{had}}, \tag{1}$$

where $E_{\mathrm{tot}}$ is the calibrated total energy deposited in the full calorimeter, $\alpha$ and $\beta$ are the calibration parameters, and $E_{\mathrm{em}}$ and $E_{\mathrm{had}}$ are the sum of energies deposited in FoCal-E and FoCal-H before the calibration, respectively. This calibration procedure has been carried out for FoCal-E with both sandwich and spaghetti implementations of FoCal-H.

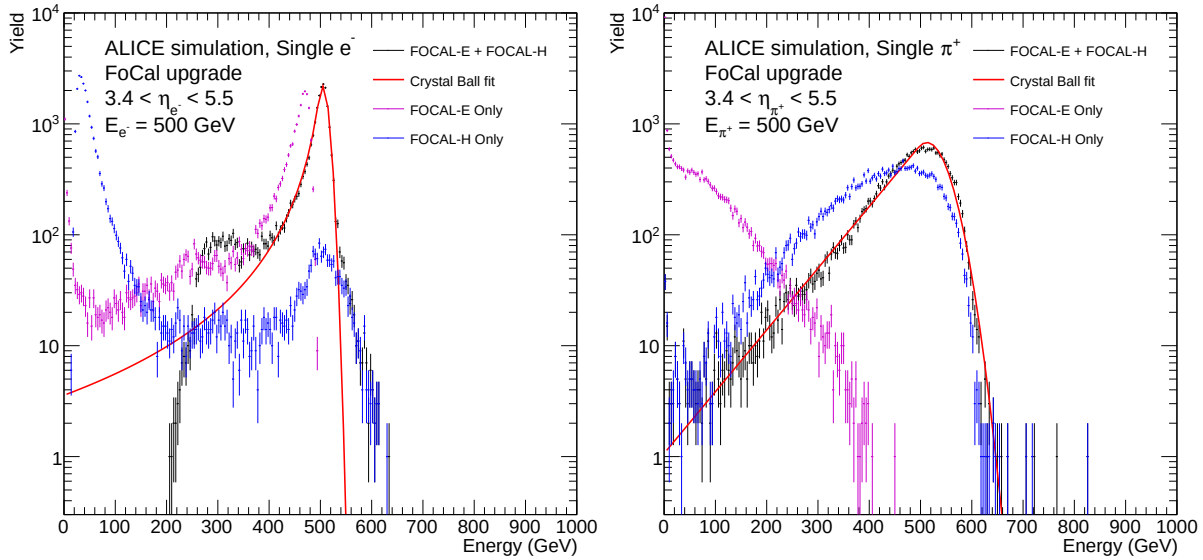


(a) Electrons (b) Pions

**Fig. 5:** Distribution of $\alpha E_{\mathrm{em}}$ (FoCal-E only), $\beta E_{\mathrm{had}}$ (FoCal-H only), and $E_{\mathrm{tot}}$ (FoCal-E and FoCal-H), for electrons (left panel) and charged pions (right panel) with initial energy of $E = 500$ GeV. The lines are fits of the Crystal Ball function to the total distribution.

Figure 5 shows the distribution of $\alpha E_{\mathrm{em}}$, $\beta E_{\mathrm{had}}$, and $E_{\mathrm{tot}}$, for electrons and charged pions with energy $E = 500$ GeV. In Fig. 5(a), the peak at 500 GeV in the distribution of energy deposited in FoCal-H is due to punch-through electrons, which traverse FoCal-E in the cold plate, depositing only a small amount of energy, and then showering mostly in FoCal-H. For electrons, there is a small plateau at around 300 GeV, which corresponds to the electrons losing a part of their energy in the dead material around the focal-E modules. The peak of the FoCal-H distribution at about 30 GeV is due to the electromagnetic showers leaking into FoCal-H.

To assign the values for $\alpha$ and $\beta$, the calibration procedure utilizes a fit of the Crystal Ball function [12] to the total distribution ($E_{\mathrm{tot}}$), as shown in Fig. 5. The Crystal Ball function can be written as following:

$$f(x;\mu,\sigma,\gamma,n) = N \begin{cases} \exp(-\frac{(x-\mu)^2}{2\sigma^2}), & \text{for } \frac{x-\mu}{\sigma} \geq -\gamma \\ A\,.\,(B - \frac{x-\mu}{\sigma})^{-n}, & \text{for } \frac{x-\mu}{\sigma} < -\gamma \end{cases} \tag{2}$$

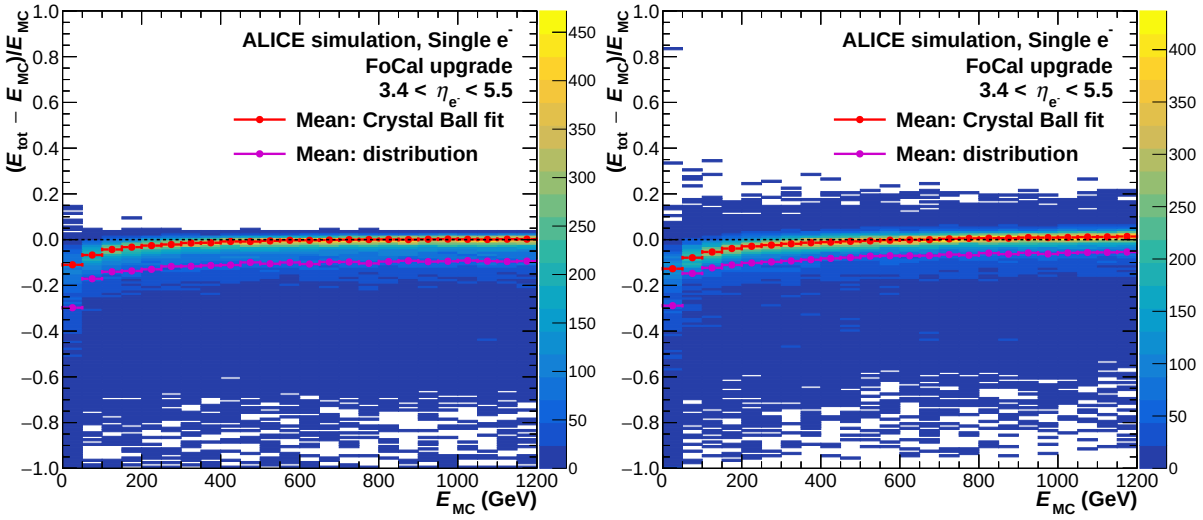


(a) Sandwich FoCal-H design (b) Spaghetti FoCal-H design

**Fig. 6:** Distribution of $\Delta E/E_{\mathrm{MC}}$, the relative difference of particle-level and detector level response to electrons (see text). Left: sandwich FoCal-H design; right: spaghetti FoCal-H design. The red line is the mean extracted from a fit of the Crystal Ball [12] function to the energy distribution in each $E_{\mathrm{MC}}$ bin. The magenta line is the mean of the distribution in each $E_{\mathrm{MC}}$ bin.

with:

$$A = (\frac{n}{|\gamma|})^n . \exp{-\frac{|\gamma|}{2}}, \quad \text{and} \quad B = \frac{n}{|\gamma|} - |\gamma|$$

where $N$ is the normalization constant, $\mu$ is the mean of the Gaussian, $\sigma$ is the standard deviation of the Gaussian, $\gamma$ is a parameter that determines the transition point from the Gaussian distribution to the power-law tail, and $n$ is the exponent of the power-law tail.

The values of $\alpha$ and $\beta$ of Eq. (1) are varied in an iterative process until the peak position of the fit is 500 GeV.

### 3.2 Response to electrons

The performance of FoCal for measuring electrons is studied in simulations using single electrons distributed uniformly in energy and uniformly in $(\eta, \varphi)$ within the acceptance. As shown in Fig. 5, electrons deposit most of their energy in FoCal-E, with a small fraction on average in FoCal-H. This study uses the combined energy $E_{\mathrm{tot}}$, which corresponds to the sum of cluster energies in FoCal-E and cell energies in FoCal-H.

Figure 6 shows the distribution of $\Delta E/E_{\mathrm{MC}}$ , the relative difference between particle-level and detector-level response of FoCal to electrons, where $\Delta E = E_{\mathrm{tot}} - E_{\mathrm{MC}}$ and $E_{\mathrm{MC}}$ is the particle energy. Both the peak of the fitted Crystal Ball function and the mean of the distribution exhibit non-linearity of up to 10% for $E < 200$ GeV; at higher energy the response is linear to a good precision. The response of the sandwich and spaghetti designs is similar for this performance metric.

The FoCal-E resolution is estimated from the distribution in Fig. 6 by fitting the Crystal Ball function to each bin in $E_{\mathrm{MC}}$ and extracting the Gaussian width parameter of the fit function as "resolution" parameter ($\sigma$). Figure 7(a) shows the relative electron energy resolution, which achieves 2% at high energy.

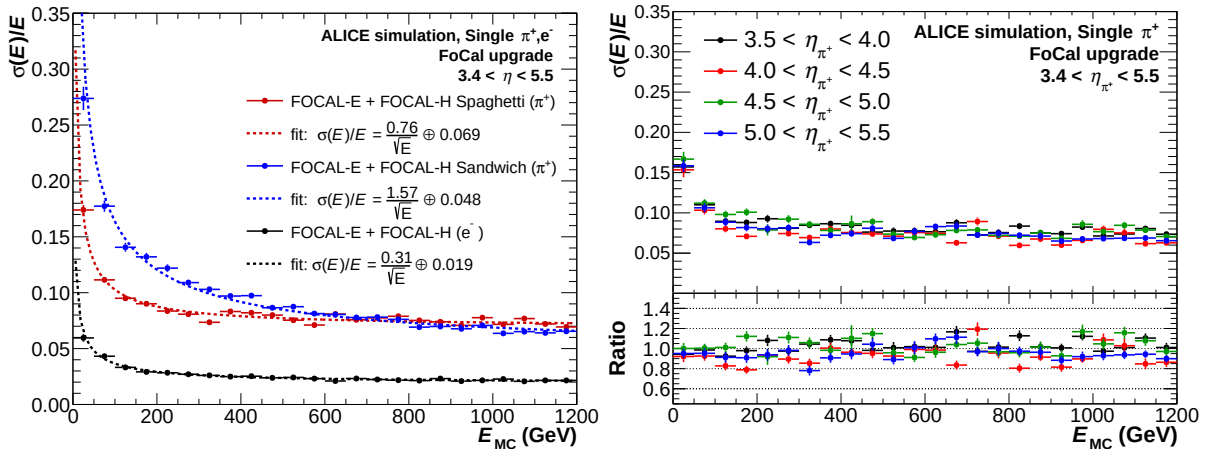


(a) Resolution comparison

(b) Resolution in rapidity bins

**Fig. 7:** Left: Relative energy resolution of charged pions and electrons versus particle energy estimated with the Gaussian width of the CB fits, as explained in the text. The resolution for charged pions is shown for both sandwich and spaghetti designs for FoCal-H. Right: $\eta$ dependence of energy resolution for charged pions with the spaghetti design of FoCal-H. The bottom panel corresponds to the ratio of the $\eta$ dependent resolution over the general spaghetti FoCal-H resolution of the left panel.

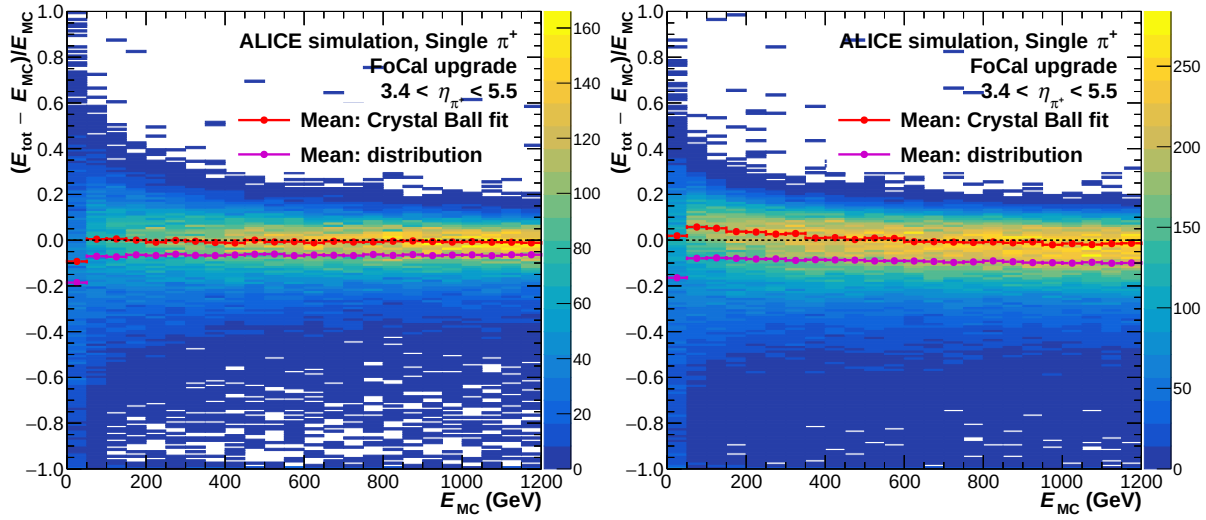


(a) Sandwich FoCal-H design

(b) Spaghetti FoCal-H

**Fig. 8:** Same as Fig. 6 but for charged pions.

### 3.3 Response to charged hadrons

The performance of FoCal-H is evaluated in simulations using single charged pions, likewise distributed uniformly in energy and uniformly in $(\eta, \varphi)$ within the acceptance. As shown in Fig. 5, most of the pion energy is deposited in FoCal-H, with a smaller fraction in FoCal-E. For this study we similarly utilize $(E_{\mathrm{tot}})$, the sum of cluster energy in FoCal-E and cell energy in FoCal-H.

Figure 8 shows the distribution of $\Delta E/E_{\mathrm{MC}}$ for pions. The response is, to a good approximation, linear over the full range of $E_{\mathrm{MC}}$, with the spaghetti design having a slightly larger non-linearity for low $E_{\mathrm{MC}}$ values than the sandwich design.

The resolution parameter of both FoCal-H designs was determined from the distributions in Fig. 8 by

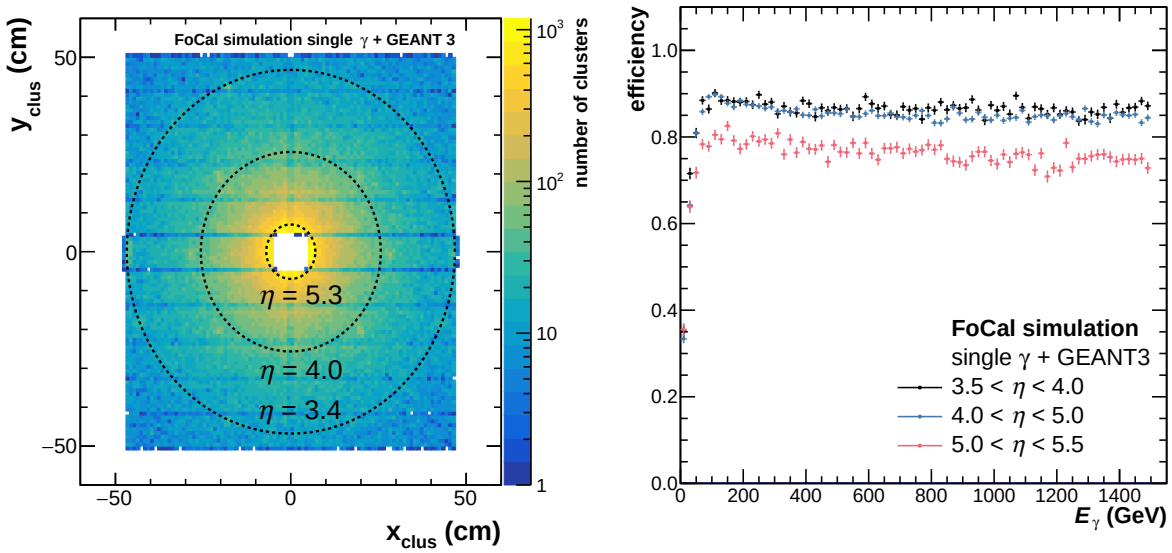


(a) cluster position

(b) photon reconstruction efficiency

**Fig. 9: Left:** Position of reconstructed photon clusters in FoCal-E. Dashed lines indicate the projection of various pseudorapidity selections in the $x-y$ plane. **Right:** Photon reconstruction efficiency as a function of true photon energy $E_\gamma$ for various pseudorapidity ranges indicated in the legend.

fitting the Crystal Ball function to each bin in $E_{\mathrm{MC}}$ and using the width of the Gaussian core of the fit function as an estimate of the resolution.

Figure 7(a) compares the energy resolution of pions for the two implementations of FoCal-H. The resolution of the spaghetti setup is better at low energy, while the resolution of the two designs is similar for $E > 600$ GeV, achieving 8%. Figure 7(b) shows the $\eta$ dependence of the resolution parameter for charged pions for the spaghetti setup which is independent of $\eta$ to a good approximation.

### 3.4 Response to photons

The response of the FoCal detector to photons is studied using a box simulation of events containing a single photon (see Sec. 2.2). The photons are generated using a flat momentum distribution of $0 < p < 1.5\,\mathrm{TeV}$ in order to ensure sufficient statistical precision for the covered momentum range. The simulated single photon events are then further propagated through the implementation of the detector geometry in GEANT3. Signals in the active detector material are then combined into clusters, following the reconstruction procedure outlined in Sec. 2.3.

Figure 9(b) shows the reconstruction efficiency of photons in the FoCal-E acceptance as a function of the true photon energy $E_\gamma$ for various pseudorapidity ranges. A reconstruction efficiency of about 90 % is observed over almost the full inspected energy range of up to 1.5 TeV. A lower efficiency of around 80 % is observed for the most forward range, $5.0 < \eta < 5.5$, which can be attributed to the reduced azimuthal coverage due to the empty space in the centre of the detector to accomodate the beampipe, which is not azimuthally uniform. This is illustrated in Fig. 9(a), which shows the $(x,y)$ position of photon clusters in FoCal-E as well as contours at several values of pseudorapidity. In addition, the reconstruction efficiency includes the effect of acceptance losses due to gaps in FoCal-E to accommodate the cooling support of the readout electronics, which are visible as horizontal stripes in Fig. 9(a). A decreasing efficiency is observed for $E_\gamma \lesssim 100\,\mathrm{GeV}/c$, which is attributable to the performance of clustering algorithms whose parameters have been optimized for higher photon energies to avoid cluster splitting.

The photon energy resolution of FoCal-E is obtained from simulations of single photons by studying the relative difference of the reconstructed cluster energy $E_{\mathrm{clus}}$ and true photon energy $E_\gamma$ as a function

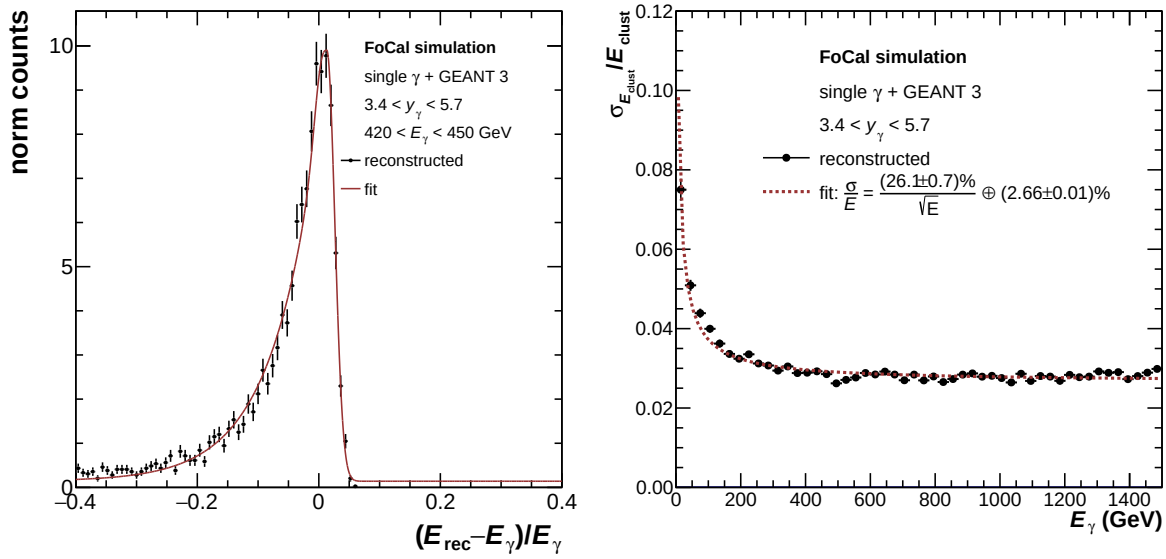


(a) energy response (b) energy resolution

**Fig. 10: Left:** Relative difference of reconstructed ($E_{\text{rec}}$) cluster energy and true photon energy ($E_\gamma$) shown for a representative photon energy interval. The red line denotes a fit of by a Gaussian function with exponential tail on the left side, which is used to extract the energy resolution $\sigma$. **Right:** Energy resolution $\sigma_{E_{\text{clust}}}/E_{\text{clust}}$ as a function of true photon energy $E_\gamma$. A fit of the energy dependence is denoted by a red line and also given in Eq. 3.

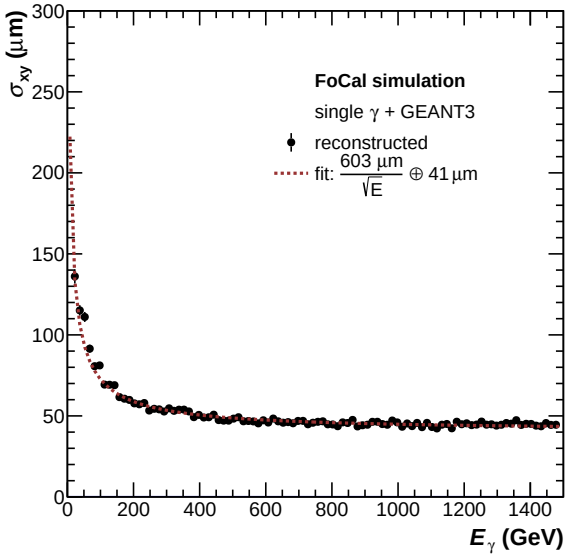


**Fig. 11:** Position resolution $\sigma_{xy}$ as a function of true photon energy $E_\gamma$, obtained from the simulation of single photon events.

of the true photon energy. This is illustrated in Fig. 10(a) for a representative photon energy interval of $420\,\text{GeV} < E_\gamma < 450\,\text{GeV}$. The response of the detector is fitted using a Gaussian function with an exponential tail on the left side, as illustrated by the red line. The energy resolution in each $E_\gamma$ interval is then quantified using the FWHM of the fit function converted to one standard deviation $\sigma$. The resulting energy resolution $\sigma_{E_{\text{clust}}}/E_{\text{clust}}$ as a function of $E_\gamma$ is shown in Fig. 10(b). A fit of the energy dependence

of the resolution yields:

$$\frac{\sigma}{E} = \frac{(26.1 \pm 0.7)\%}{\sqrt{E}} \oplus (2.66 \pm 0.01)\%, \tag{3}$$

where the energy is given in units of GeV and $\oplus$ denotes addition in quadrature. This energy resolution estimate is purely based on the information from GEANT3 and does not include additional detector effects such as channel-by-channel variation in gain, non–linearity, and electronic noise, which are expected to worsen the constant term 2.62 %.

The position resolution of the FoCal-E detector is also studied using these single-photon simulations, by comparing the cluster position (energy weighted centroid) at the detector level with the position of the parent photon at the generator (or particle) level. The latter is obtained by extrapolating the trajectory of the photon as a straight line from the nominal collision point to the FoCal surface. Figure 11 shows the spatial difference position resolution in the $(x,y)$ plane as a function of true photon energy $E_\gamma$. There is no significant difference in the resolution in $x$ and $y$ direction, which both have a constant term of about 41 μm at high photon energy.

# 4 Isolated and direct photon measurements

## 4.1 Background rejection

An overview of prompt photon measurements at collider energies is provided in Ref. [13], and a first look at photon identification in the FoCal, including isolation, is presented in Ref. [2]. This section provides a more detailed discussion of the performance of the FoCal for prompt photon measurements.

One of the key challenges for the measurement of prompt–photon production is the discrimination of signal photons, originating directly from the hard scattering of the collisions, from photons originating from particle decays, where the latter are the dominant source of photons produced in a collision. In addition, prompt photons have contributions from the direct (Compton) process and the fragmentation of scattered partons. For precise comparison to theoretical calculations, it is desirable to suppress the fragmentation component, since its description requires the weakly-constrained photon fragmentation function.

Prompt–photon measurements in the FoCal detector will utilize three techniques to enhance the signal contribution:

1. Isolation: measurement of the isolation energy in FoCal-E and FoCal-H in a cone of given radius around the photon candidate, with rejection of candidates with isolation energy above a specified threshold.

2. Invariant mass: rejection of photons originating from $\pi^0$ decays using the invariant mass of cluster pairs.

3. Shower shape: rejection of elongated clusters originating from decay photons with small opening angle.

The performance of this approach is studied using simulations of pp and p–Pb collision events at $\sqrt{s} = 14$ TeV and $\sqrt{s_{\mathrm{NN}}} = 8.8$ TeV, respectively. Details about simulations are given in Sec. 2.2.

### *4.1.1 Isolation*

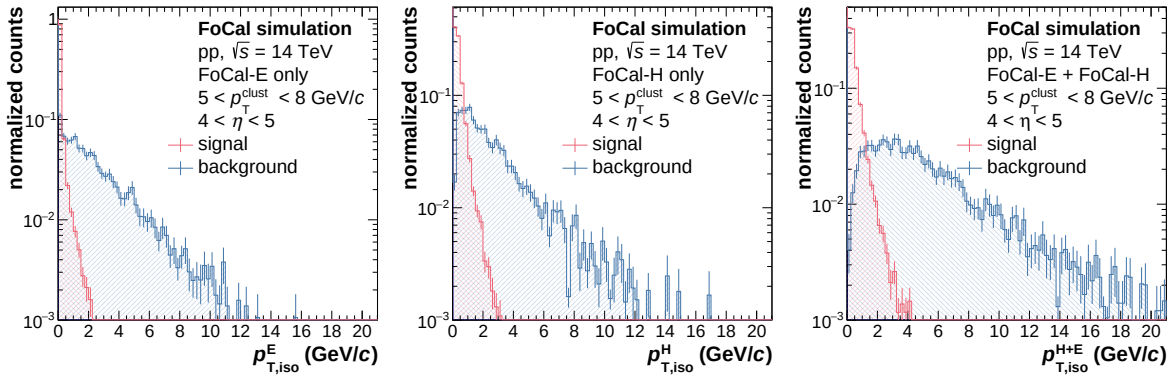


(a) FoCal-E only (b) FoCal-H only (c) FoCal-E + FoCal-H

**Fig. 12:** Distribution of isolation energy $p_{\mathrm{T,iso}}$ of photon clusters with $p_{\mathrm{T}} > 5\,\mathrm{GeV}/c$ in $\sqrt{s} = 14$ pp collisions simulated by PYTHIA, using Eq. 4 with $R = 0.4$. Left: FoCal-E only; center: FoCal-H only; right: FoCal-E+FoCal-H. Blue distributions: isolation energy of all photon clusters; red: isolation energy of signal photons, obtained by only simulating hard scatterings with photons in final state. Both distributions normalized to unity.

Measurement of the energy in the vicinity of a photon candidate provides significant suppression of decay and fragmentation photons, and has been commonly used in measurements of prompt–photon production at the LHC (see e.g. Ref. [14]). This is usually done by calculating the sum of the transverse momentum $p_{\mathrm{T}}$ of particles within a cone around the given photon and requiring that the sum does not exceed a given

threshold. The isolation energy $p_{\mathrm{T,iso}}$ is defined as:

$$p_{\mathrm{T,iso}} := \sum_i p_{\mathrm{T},i}\,\theta(R - R_i) \quad \text{with} \quad R_i = \sqrt{(\eta_\gamma - \eta_i)^2 + (\varphi_\gamma - \varphi_i)^2}, \tag{4}$$

where $\eta_i$ and $\varphi_i$ are the pseudorapidity and azimuthal angle of a particle or calorimeter cell $i$, respectively, which are used to calculate the radial distance $R_i$ with respect to the position $(\eta_\gamma, \varphi_\gamma)$ of the given photon.

Figure 12 shows the distribution of isolation energy $p_{\mathrm{T,iso}}$ in a cone of radius $R = 0.4$ for simulated pp collision events at $\sqrt{s} = 14\,\mathrm{TeV}$. The isolation energy is calculated according to Eq. 4 for all photon clusters with $5\,\mathrm{GeV} < p_{\mathrm{T}} < 8\,\mathrm{GeV}/c$ found within $4 < \eta < 5$. Distributions are shown for FoCal-E or FoCal-H only, and their sum. Discrimination is provided by the difference between the red and blue curves, which denote signal and background-dominated samples, respectively (see Sec. 2.2). A clear separation between signal and background is observed; signal photons are more isolated than background photons.

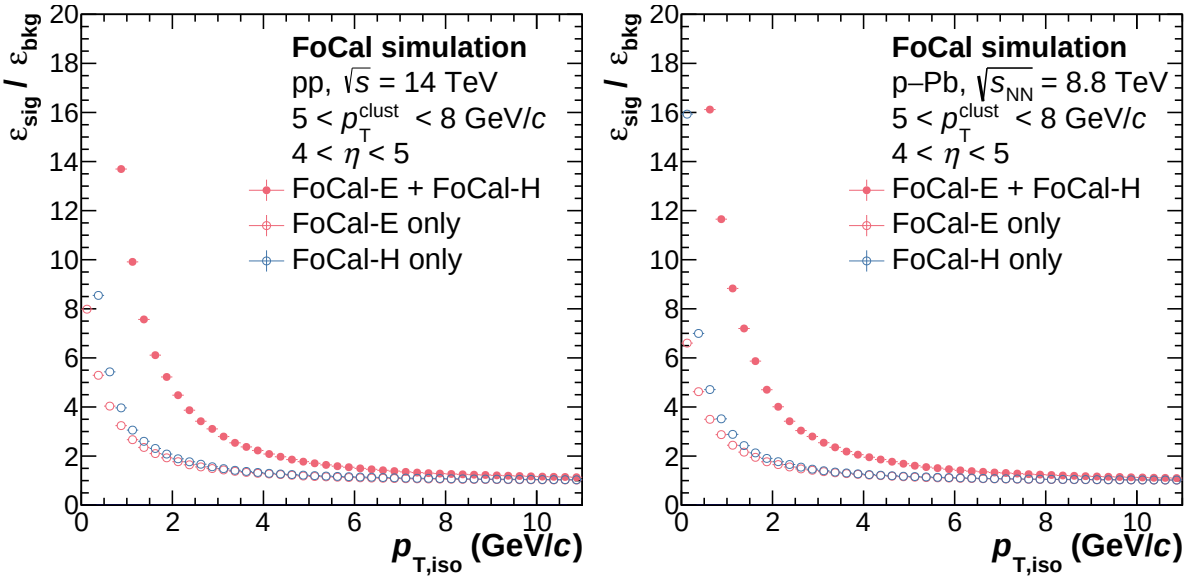


(a) pp collisions at $\sqrt{s} = 14\,\mathrm{TeV}$

(b) p–Pb collisions at $\sqrt{s_{\mathrm{NN}}} = 8.8\,\mathrm{TeV}$

**Fig. 13:** Signal-to-background efficiency ratio ($\varepsilon_{\mathrm{sig}}/\varepsilon_{\mathrm{back}}$) as a function of the isolation threshold $E_{\mathrm{T,cut}}$ for simulated pp and p–Pb collision events at $\sqrt{s_{\mathrm{NN}}} = 14\,\mathrm{TeV}$ and $8.8\,\mathrm{TeV}$, respectively. Different colors and markers denote the detectors used to calculate the isolation energy.

The discrimination power of the isolation energy is quantified by calculating the ratio of the signal and background efficiency ($\varepsilon_{\mathrm{sig}}/\varepsilon_{\mathrm{back}}$) as a function of the isolation threshold $E_{\mathrm{T,cut}}$, which is shown in Fig. 13 for simulated pp and p–Pb collision events at $\sqrt{s_{\mathrm{NN}}} = 14\,\mathrm{TeV}$ and $8.8\,\mathrm{TeV}$, respectively. The signal and background efficiencies are the fraction of clusters fulfilling the given isolation threshold criterion in the respective sample. A clear increase of the signal to background efficiency ratio is observed for increasingly strict isolation thresholds in both collision systems. In addition, the combined signal from FoCal-E and FoCal-H for photon isolation provides markedly better discrimination than FoCal-E or FoCal-H separately.

Slightly smaller signal-to-background efficiency ratios are obtained for p–Pb collisions with respect to pp collisions, which can be attributed to the overall slightly larger underlying event in p–Pb collisions leading to a slightly reduced background efficiency, as shown later in Fig. 16(d). An isolation requirement of $p_{\mathrm{T,iso}}^{\mathrm{H+E}} < 2\,\mathrm{GeV}$ improves the signal-to-background efficiency ratio in the pp sample by about a

factor of five. For the p–Pb sample, an isolation requirement of $p_{\mathrm{T,iso}}^{\mathrm{H+E}} < 3\,\mathrm{GeV}$ is used to account for the underlying event subtraction.

### 4.1.2 Invariant mass tagging

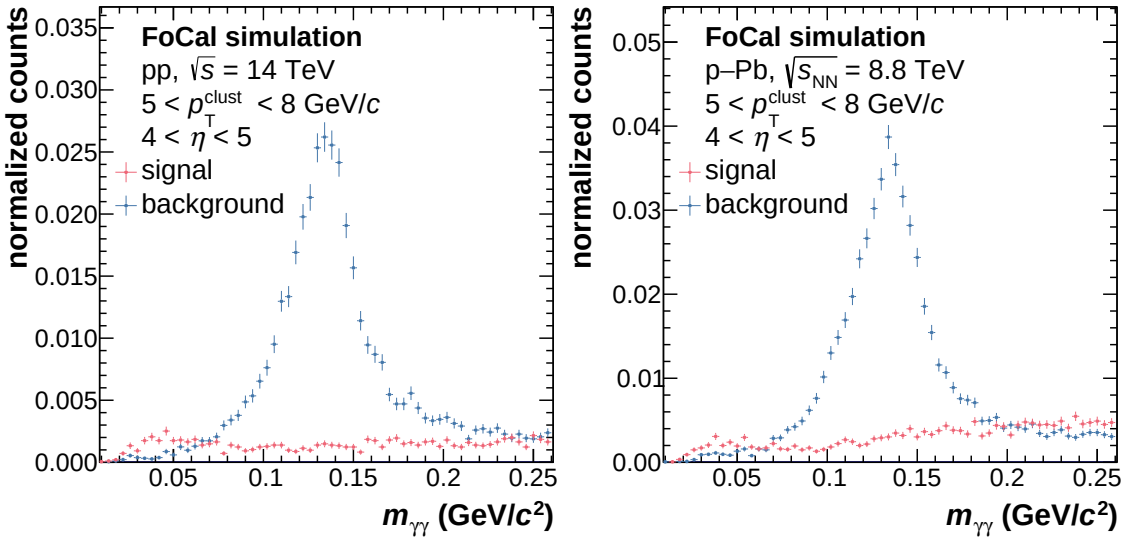


(a) pp collisions at $\sqrt{s} = 14\,\mathrm{TeV}$ (b) p–Pb collisions at $\sqrt{s} = 8.8\,\mathrm{TeV}$

**Fig. 14:** Invariant mass distribution $m_{\gamma\gamma}$ of all cluster pairs with an invariant mass closest to the nominal $\pi^0$ mass, for signal and background-dominated simulated samples of pp and p–Pb collisions at $\sqrt{s_{\mathrm{NN}}} = 14\,\mathrm{TeV}$ and 8.8 TeV, respectively.

Enhancement of the signal-to-background ratio using the invariant mass of cluster pairs has been studied using simulations of pp and p–Pb collision events at $\sqrt{s_{\mathrm{NN}}} = 14$ and 8.8 TeV, respectively. Figure 14 shows the invariant mass distribution, $m_{\gamma\gamma}$, of cluster pairs in the signal and background-dominated simulation samples. For each cluster with an energy above 2 GeV the invariant mass of all pairs containing a given cluster is calculated via

$$m_{\gamma\gamma} = \sqrt{2E_{\gamma_1}E_{\gamma_2}(1-\cos\theta_{12})}, \tag{5}$$

where $E_{\gamma_{1,2}}$ are the energies of the respective clusters and $\theta_{12}$ is the opening angle between the clusters in the laboratory frame. The invariant mass closest to the nominal $\pi^0$ mass is assigned as the invariant mass associated with the given cluster, resulting in the distributions shown in Fig. 14. A clear peak in the vicinity of the nominal $\pi^0$ mass is visible for the background-dominated sample, whereas no such peak is visible for signal photons. This allows usage of the invariant mass to "tag" photons originating from $\pi^0 \to \gamma\gamma$ decays by rejecting all clusters with an associated invariant mass of $70\,\mathrm{MeV}/c^2 < m_{\gamma\gamma} < 180\,\mathrm{MeV}/c^2$.

### 4.1.3 Shower-shape tagging

Enhancement of the signal-to-background ratio using shower shape in FoCal-E has been studied using the same simulated data. The shape of an electromagnetic shower is expressed as an ellipse, representing the covariance matrix of the shower energy distribution in $(\eta, \varphi)$. The covariance matrix has terms $\sigma^2_{\varphi\varphi}$, $\sigma^2_{\eta\eta}$, and $\sigma^2_{\varphi\eta}$, which are calculated using the energy distributions along the $\eta$ and $\varphi$ directions with respect to the leading cell of the cluster via:

$$\sigma^2_{\alpha\beta} = \sum_i \frac{w_i\alpha_i\beta_i}{w_{\mathrm{tot}}} - \sum_i \frac{w_i\alpha_i}{w_{\mathrm{tot}}} \sum_j \frac{w_j\beta_j}{w_{\mathrm{tot}}} \quad \text{with} \quad w_{\mathrm{tot}} = \sum_i w_i, \tag{6}$$

where $\alpha_i$ and $\beta_i$ are tower indices along the $\eta$ and $\phi$ direction. The weighting factors $w_i$ are defined as:

$$w_i = \max(0, w_{\text{max}} + \ln(E_i^{\text{cell}}/E_{\text{clus}})) \quad \text{with} \quad w_{\text{max}} = 4.5, \tag{7}$$

where $E_i^{\text{cell}}$ and $E_{\text{clus}}$ are the energy of cell $i$ and of the cluster, respectively. Finally, the long and short axes of the shower-shape ellipse are calculated for each FoCal-E pad and pixel layer individually via:

$$\sigma^2_{\text{long}} = 0.5 \cdot (\sigma^2_{\varphi\varphi} + \sigma^2_{\eta\eta}) + \sqrt{0.25 \cdot (\sigma^2_{\varphi\varphi} - \sigma^2_{\eta\eta})^2 + \sigma^4_{\eta\varphi}}, \tag{8}$$

$$\sigma^2_{\text{short}} = 0.5 \cdot (\sigma^2_{\varphi\varphi} + \sigma^2_{\eta\eta}) - \sqrt{0.25 \cdot (\sigma^2_{\varphi\varphi} - \sigma^2_{\eta\eta})^2 + \sigma^4_{\eta\varphi}}. \tag{9}$$

Figure 15 shows the distribution of the long axis of the shower-shape ellipse for FoCal-E pad layers, $\sigma^2_{\text{long}}$, in simulated pp and p–Pb collision events at $\sqrt{s_{\text{NN}}} = 14\,\text{TeV}$ and 8.8 TeV, respectively. Its value is the sum of $\sigma^2_{\text{long}}$ calculated for each pad layer, weighted by the cluster energy found in the given layer.

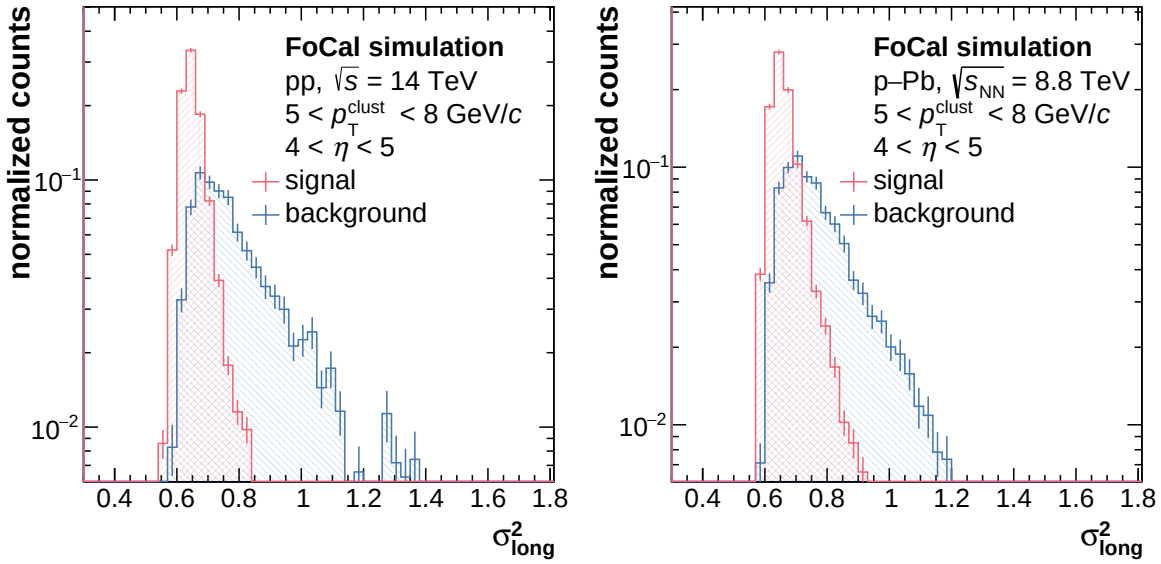


(a) pp collisions at $\sqrt{s} = 14\,\text{TeV}$

(b) p–Pb collisions at $\sqrt{s_{\text{NN}}} = 8.8\,\text{TeV}$

**Fig. 15:** Distribution of the long axis $\sigma^2_{\text{long}}$ of the shower shape ellipse calculated according to Eq. 8 for simulated pp and p–Pb collisions at $\sqrt{s_{\text{NN}}} = 14\,\text{TeV}$ and 8.8 TeV, respectively, using only pad layers of the FoCal-E. The red and blue distributions show the signal and background photon clusters, respectively.

One finds that clusters from the background sample are elongated with respect to signal photons, which can be attributed to the overlap of electromagnetic showers from multiple particles that get reconstructed as a single cluster in the less granular pad layers. The high granularity of the pixel layers significantly reduces shower overlaps, which is in turn exploited for the invariant mass tagging discussed in the previous section. A signal selection of $\sigma^2_{\text{long}} < 0.8$ in the pad layers is imposed in the prompt photon analyses, where the threshold is chosen to optimize the signal and background discrimination while maintaining a sufficient signal efficiency.

### 4.2 Photon reconstruction efficiency

Figure 16 shows the signal and background efficiency as a function of cluster $p_{\text{T}}$ in simulated pp collisions at $\sqrt{s} = 14$ TeV and p–Pb collisions at $\sqrt{s_{\text{NN}}} = 8.8$ TeV. Background rejection utilizes decay rejection, isolation, and shower-shape cuts, as indicated. A high prompt–photon signal reconstruction

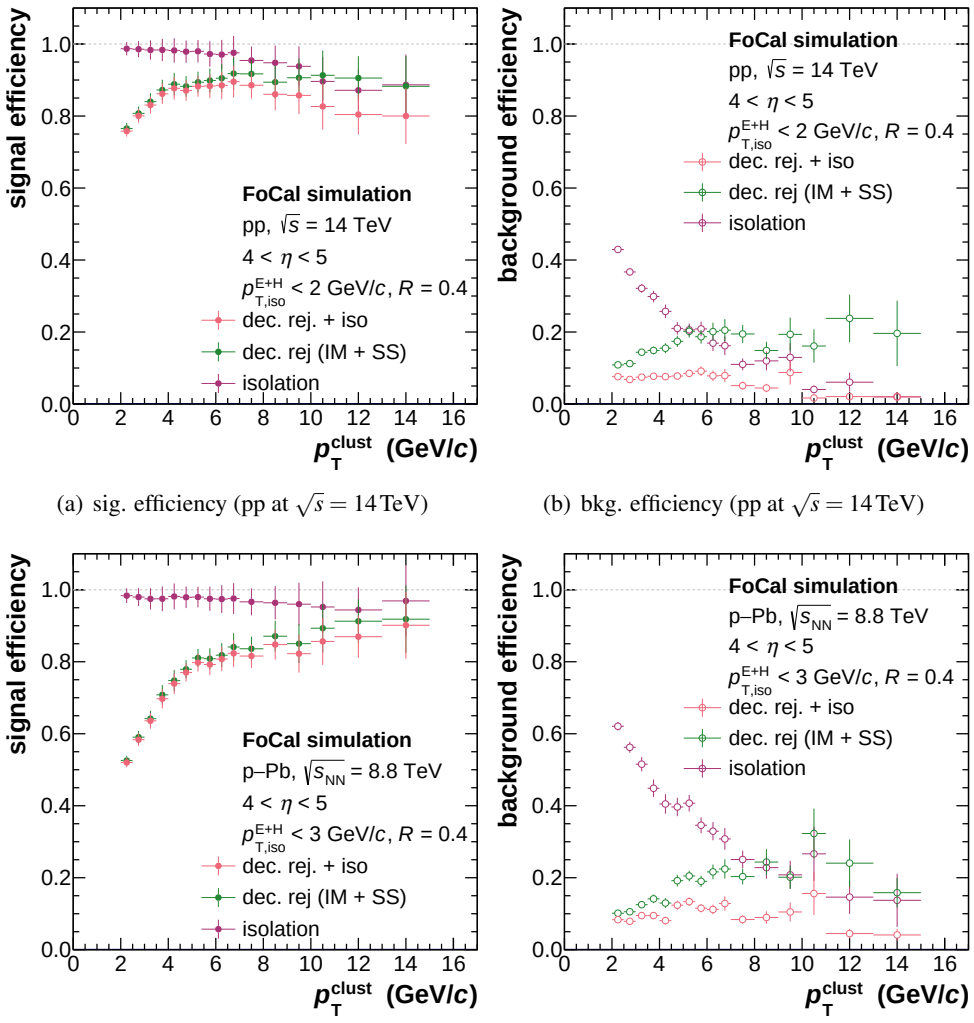


(a) sig. efficiency (pp at $\sqrt{s} = 14\,\text{TeV}$)

(b) bkg. efficiency (pp at $\sqrt{s} = 14\,\text{TeV}$)

(c) sig. efficiency (p–Pb at $\sqrt{s_{\text{NN}}} = 8.8\,\text{TeV}$)

(d) bkg. efficiency (p–Pb at $\sqrt{s_{\text{NN}}} = 8.8\,\text{TeV}$)

**Fig. 16:** Signal and background photon reconstruction efficiency as a function of cluster $p_{\text{T}}$, for pp collisions at $\sqrt{s} = 14$ TeV (upper) and p–Pb collisions at $\sqrt{s_{\text{NN}}} = 8.8$ TeV (lower). Background rejection is shown for various combinations of decay rejection, isolation, and shower-shape cuts. Low background efficiency and high signal efficiency are desirable.

efficiency and low background reconstruction efficiency are desirable, the latter corresponding to a large background rejection.

In pp collisions, the invariant mass rejection (IM) of $\pi^0 \to \gamma\gamma$ decays and shower-shape selection remove about 87 % of background clusters for $p_{\text{T}} < 15$ GeV/$c$ (Fig. 16(b)). The isolation requirement in a cone with radius $R = 0.4$, $E_{\text{T,iso}}^{\text{H+E}} < 2\,\text{GeV}$, is most efficient at large $p_{\text{T}}$, with background rejection of up to 91 %. An overall background rejection of up to 97 % is achieved by combining decay rejection and isolation.

The corresponding prompt–photon signal reconstruction efficiency is shown in Fig. 16(a). No significant inefficiencies are introduced from the isolation requirement, with signal efficiencies above 90 %. The SS and IM rejection removes less than 25 % of the signal photons, mainly attributed due to the overlap of signal and background distributions (Fig. 15) and the contribution of combinatorial background to the invariant mass distribution.

A similar picture is found for p–Pb collisions (Fig. 16, lower panels): The signal efficiency after all

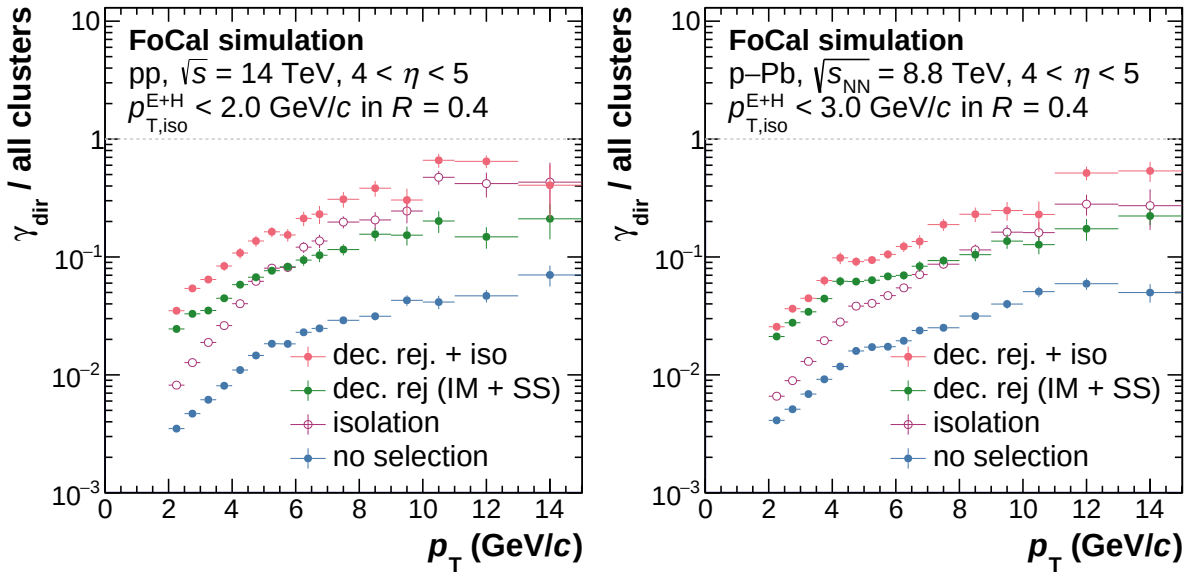


(a) pp collisions at $\sqrt{s} = 14\,\text{TeV}$ (b) p–Pb collisions at $\sqrt{s_{\text{NN}}} = 8.8\,\text{TeV}$

**Fig. 17:** Fraction of clusters produced by a prompt signal photon with respect to all clusters produced in simulated pp collisions at $\sqrt{s} = 14$ TeV and p–Pb collisions at $\sqrt{s_{\text{NN}}} = 8.8$ TeV. Fractions are shown for various combinations of decay rejection, isolation, and shower shape cuts.

cuts is between about 50 % and 90 %, slightly smaller than in the pp sample due to larger combinatorial background and absence of event-by-event underlying event subtraction. Strong background suppression is observed, with background efficiency of at most a few percent.

Figure 17 shows the fraction due to prompt–photon production of all reconstructed clusters, for pp and p–Pb collisions. The ratio is obtained by first converting the observed counts of reconstructed clusters fulfilling the various selection criteria to cross sections using the information from PYTHIA of the hard scattering cross section and number of trials. The thus obtained cross sections for the signal ($\gamma$-jet MC) and background (jet-jet MC) dominated samples are added, resulting in a combined sample of clusters from signal and background processes that satisfy the (leading order) expectation of the signal-to-background ratio.

Prior to background rejection the signal fraction is low, ranging from about 2 % up to 6 % in both collision systems. After application of all three sets of cuts the signal fraction increases to 72 % at $p_{\text{T}} = 14\,\text{GeV}$, corresponding to improvement by a factor 11.

### 4.3 Physics performance of FoCal isolated prompt photon measurements

As discussed in Ref. [2], FoCal measurements of forward prompt–photon production provide incisive probes of the low-$x$ structure of matter, and play a key role in the search for evidence of non-linear QCD evolution at low $x$. An important element of this program is the constraint of PDFs at low $x$. However, the projection of future measurements to provide such constraints is complex because it depends crucially on unknown factors, notably the ultimate systematic precision achieved for such measurements, and complementary constraints imposed by other measurements and other experiments.

To simplify the discussion, this section focuses on the impact of isolated prompt photon measurements on existing PDFs, using Bayesian inference. This is achieved by constructing FoCal pseudo-data, making reasonable assumptions for the expected statistical and systematic uncertainties. These pseudo-data are used to re-weight existing PDFs sets, following the procedure outlined in Ref. [15].

### 4.3.1 *Statistical uncertainties*

Projected statistical uncertainties of isolated prompt photon measurements with the FoCal are estimated using JETPHOX calculations at NLO of production cross sections in pp and p–Pb collisions at $\sqrt{s_{\mathrm{NN}}} =$ 8.8 TeV. Cross sections are converted to yields using the expected integrated luminosity for LHC Run 4 (Sec. 1). Yields are scaled by the signal efficiencies in Fig. 16, which are due to cuts based on shower isolation, shower shape, and invariant mass tagging.

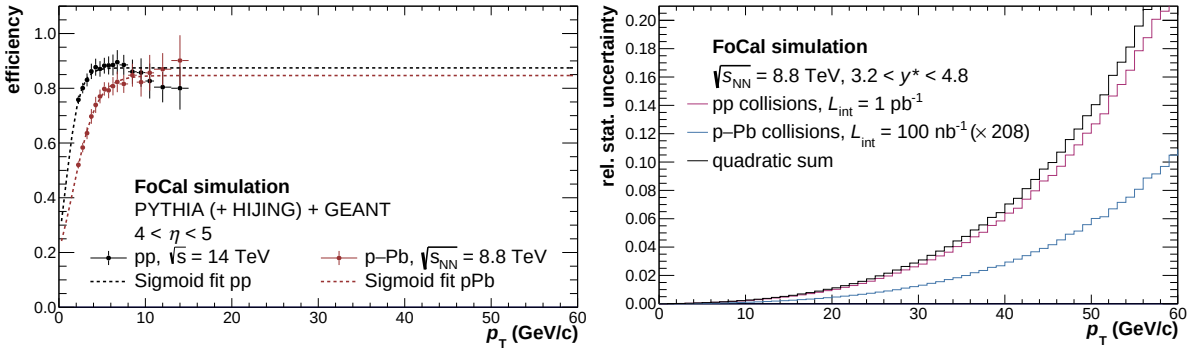


(a) Signal reconstruction efficiency

(b) statistical uncertainties

**Fig. 18: Left:** Prompt–photon signal reconstruction efficiency for pp and p–Pb collisions at $\sqrt{s_{\mathrm{NN}}} = 14\,\mathrm{TeV}$ and 8.8 TeV, respectively, obtained using PYTHIA (+ HIJING) simulations. The clusters are required to fulfill an isolation requirement, shower shape selection, and invariant mass tagging, as outlined in the text. **Right:** Expected statistical uncertainties of prompt photon measurements with the FoCal detector.

Figure 18(a) shows the signal reconstruction efficiency for both collision systems. The efficiency is fit with an exponential function,

$$f(p_{\mathrm{T}}) = \frac{a_0}{1+\exp(-a_1 \cdot (p_{\mathrm{T}} - a_2))}, \tag{10}$$

which is used to extrapolate to larger $p_{\mathrm{T}}$ than is covered by current simulations. The yield $N$ in a given $p_{\mathrm{T}}$ bin is assigned statistical uncertainty $\sigma = \sqrt{N}$, which is shown as a function of cluster $p_{\mathrm{T}}$ for pp and p–Pb collisions in Fig. 18.

The figure also shows the quadratic sum of the statistical uncertainties in pp and p–Pb collisions, which is the projected statistical uncertainty of the nuclear modification factor $R_{\mathrm{pA}}$ at $\sqrt{s_{\mathrm{NN}}} = 8.8\,\mathrm{TeV}$. A statistical uncertainty of less than 2% is achieved for $p_{\mathrm{T}} \lesssim 25\,\mathrm{GeV}/c$, even though the pp reference data at $\sqrt{s} = 8.8\,\mathrm{TeV}$ corresponds to only one week of data-taking. A statistical uncertainty of less than 14% is achieved for $p_{\mathrm{T}} \sim 50\,\mathrm{GeV}/c$, indicating that FoCal measurements of prompt photon $R_{\mathrm{pPb}}$ will not be limited by the achievable statistical precision.

### 4.3.2 *Systematic uncertainties*

Accurate projection of systematic uncertainties is challenging, as it requires detailed understanding of the experimental data and potential deviations from the description in the simulation. Nonetheless, the simulation studies presented in the previous sections can be used to obtain an estimate of the expected systematic uncertainties.

For these projections, the INCNLO program is used to obtain the expected photon production rates in pp collisions at $\sqrt{s} = 14$ TeV and and p–Pb collisions at $\sqrt{s} = 8$ TeV. The calculations are carried out at NLO, where the expected decay-photon rate, corresponding to measurement background, is derived from the calculated $\pi^0$ yield. These yields are then scaled with the signal and background efficiency shown in Fig. 16. For both photon sources (decay photons and prompt photons) an uncertainty of about 5 % is expected at the level of extracted yields, which is dominated by the efficiency determination and the uncertainty of the energy scale. This choice is rather conservative, and is obtained assuming that the

dominant background from $\pi^0$ decays can be reconstructed with an efficiency of about 80 % and is only known with uncertainties of up to 25 %.

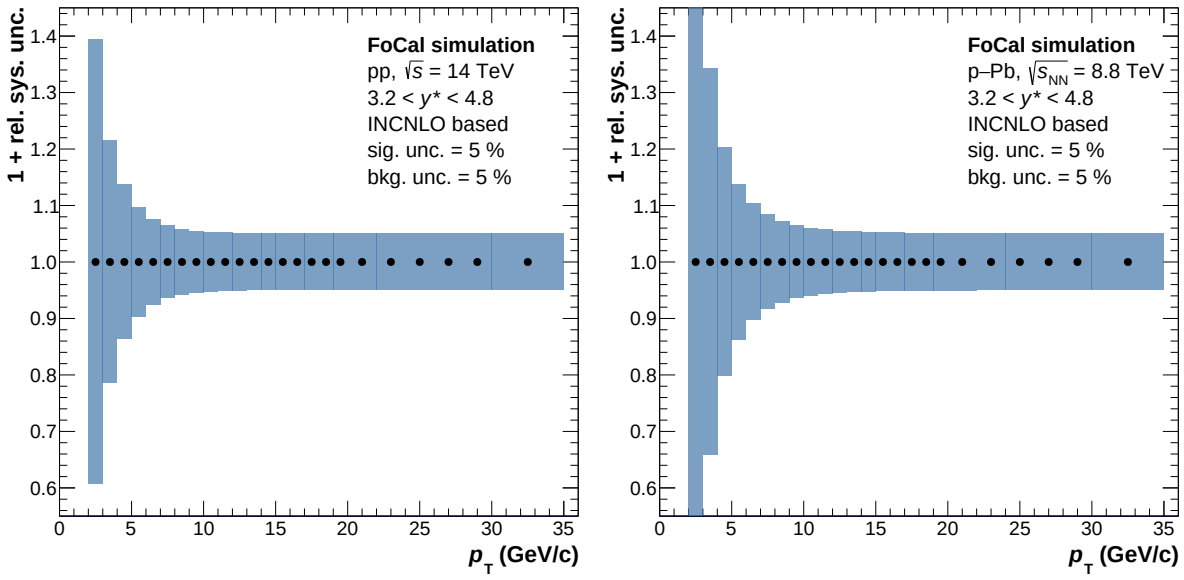


(a) pp collisions at $\sqrt{s} = 14\,\text{TeV}$ (b) p–Pb collisions at $\sqrt{s_{\text{NN}}} = 8.8\,\text{TeV}$

**Fig. 19:** Expected relative systematic uncertainty (shown as an offset to unity) for an isolated prompt photon measurement in pp and p–Pb collision at $\sqrt{s_{\text{NN}}} = 14\,\text{TeV}$ and 8.8 TeV, respectively. The estimation is based on calculations by the INCNLO program and efficiencies in Fig. 16.

Figure 19 shows the resulting systematic uncertainties at the level of the measured prompt–photon cross section, which are determined by propagating the uncertainties of the signal and background sources to the level of the background-subtracted measurement. The overall systematic uncertainty is driven by the signal-to-background ratio obtained from NLO, resulting in a systematic uncertainty reaching of less than 20 % for $p_{\text{T}} \geq 5\,\text{GeV}/c$. Below 5 GeV, driven by the increasing background, the systematic uncertainties further increase, exceeding to 40 % at $p_{\text{T}} = 2\,\text{GeV}/c$.

#### *4.3.3 Nuclear modification of inclusive prompt–photon production: $R_{\text{pPb}}$*

A key FoCal measurement for constraining nPDFs is $R_{\text{pPb}}$, the ratio of inclusive prompt–photon yields measured in p–Pb and pp collisions, normalized by a geometric factor such that $R_{\text{pPb}} = 1$ in the absence of nuclear modification of prompt–photon production. Simulations of $R_{\text{pPb}}$ utilize INCNLO [16–20] calculations at NLO, including modifications of the code to improve numerical stability at forward rapidities[2]. Statistical and systematic uncertainties are obtained as outlined in the previous sections. All scales are chosen to be equal to the photon $p_{\text{T}}$. The photon is required to be within the FoCal acceptance. The nNNPDF30 [21] nuclear PDF is used to describe the proton ($A = 1$) and lead ($A = 208$) beams.

Figure 20 shows the calculated distribution of isolated prompt photon $R_{\text{pPb}}$. The statistical uncertainty corresponds to the assumed values of $\mathscr{L}_{\text{int}}$ for p–Pb and pp data at $\sqrt{s_{\text{NN}}} = 8.8$ TeV during LHC Run 4 1, while the shaded band shows the estimated systematic uncertainty. The procedure to obtain the systematic uncertainties for the measurement in pp and p–Pb collisions is outlined in Sec. 4.3.2. Assuming conservatively no correlation of systematic uncertainties between both collision systems, the systematic uncertainty of the $R_{\text{pA}}$ is obtained by addition of the respective uncertainties in quadrature. Partial cancellation of systematic uncertainties between both collision systems is likely for a future measurement, especially given that the p–Pb and pp reference data will be taken in close proximity in time. The suppression has a mild $p_{\text{T}}$ dependence, with larger suppression at lower $p_{\text{T}}$. A suppression factor of 80% is

[2] In particular, modifications of `hadlib.f` contained in INCNLO v1.4 were provided by Ilkka Helenius.

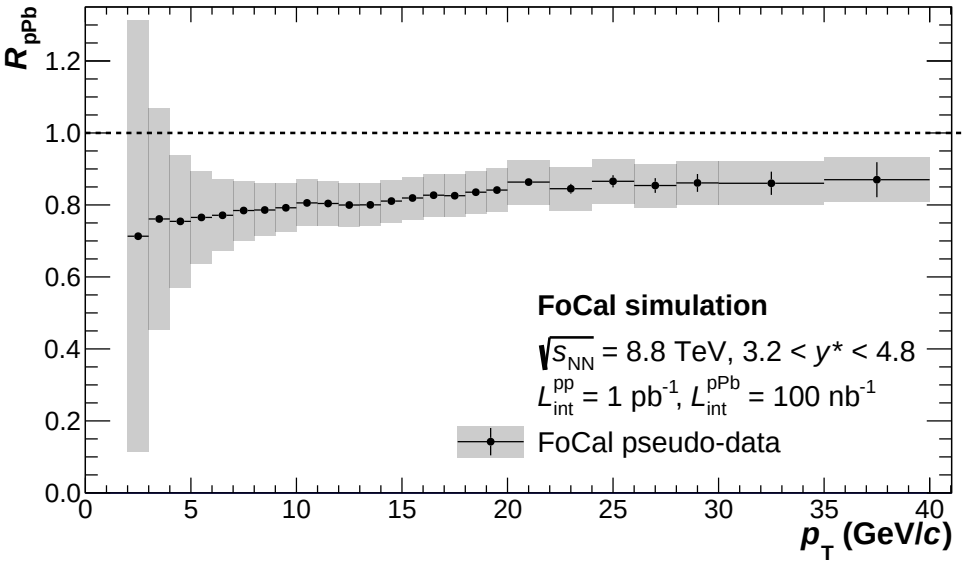


**Fig. 20:** FoCal pseudo-data of the inclusive prompt–photon yield ratio $R_{\mathrm{pPb}}$ at $\sqrt{s_{\mathrm{NN}}} = 8.8\,\mathrm{TeV}$. The central values are obtained at NLO using the INCNLO program. The nNNPDF30 is used with $A = 1$ and $A = 208$ to calculate prompt–photon yields in pp and p–Pb collisions. Vertical boxes show the statistical error and shaded boxes show the systematic uncertainty; see text for details.

found at $p_{\mathrm{T}} = 5\,\mathrm{GeV}/c$.

This $R_{\mathrm{pPb}}$ distribution from pseudo-data is compared with NLO calculations using recent PDFs [21] by the NNPDF collaboration, which are made available as MC replica sets that encode the PDF uncertainties and enable a Bayesian re-weighting procedure. This procedure requires the calculation of isolated prompt photon $R_{\mathrm{pPb}}$ for each MC replica $k$, which are then used to determine the $\chi^2$ of the comparison of distributions from the calculation and pseudo-data,

$$\chi^2_k = \frac{1}{N_{\mathrm{dat}}} \sum_{i=1}^{N_{\mathrm{dat}}} \frac{\left(R_i^{(\mathrm{th}),(\mathrm{k})} - R_i^{(\mathrm{exp})}\right)^2}{\Delta^2_{\mathrm{tot}}}, \tag{11}$$

where $N_{\mathrm{dat}}$ are the total number of data points and $\Delta^2_{\mathrm{tot}}$ is the quadratic sum of the systematic uncertainty and statistical error of each data point. The values of $R_i^{(\mathrm{exp})}$ and $R_i^{(\mathrm{th}),(\mathrm{k})}$ denote the inclusive prompt–photon yield ratio $R_{\mathrm{pPb}}$ of the pseudo-data and theoretical prediction, respectively. New posterior weights then are assigned for each PDF member component based on the value of $\chi^2$, as outlined in Ref. [15]. Calculations of the nuclear modification factor $R_i^{(\mathrm{th}),(\mathrm{k})}$ are performed using the INCNLO program at NLO. The chosen $\chi^2$ definition currently does not yet take into account the correlation of uncertainty sources in $p_{\mathrm{T}}$, which may impact the constraining power of the measurement. Nonetheless, these studies should allow for a good first estimate of the expected physics impact of prompt photon measurements in the low-$x$ regime.

Figure 21 shows $R_{\mathrm{pPb}}$ for inclusive prompt photons at $\sqrt{s_{\mathrm{NN}}} = 8.8$ TeV, compared to QCD calculations performed with INCNLO incorporating nNNPFD3.0 without constraint from LHCb D-mesons, together with reweighted distributions incorporating LHCb D-mesons [22] or FoCal prompt–photon pseudo–data. The black line and grey shaded band show the theoretical prediction and corresponding PDF uncertainty prior to any reweighting, where one finds PDF uncertainties of $\sim$30 % at $p_{\mathrm{T}} = 5\,\mathrm{GeV}/c$.

The inclusion of FoCal pseudo-data by the reweighting procedure reduces the PDF uncertainties significantly, as shown by the red line and corresponding shaded band. A reduction in nPDF uncertainties of

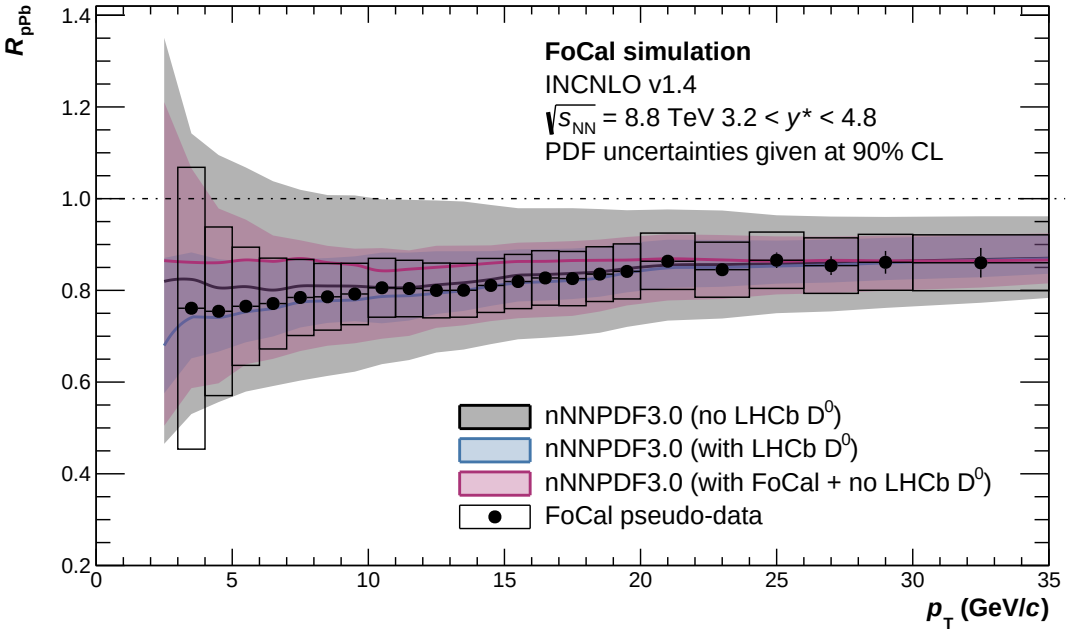


**Fig. 21:** Distribution of $R_{\mathrm{pPb}}$ for inclusive prompt photons at $\sqrt{s_{\mathrm{NN}}} = 8.8$ TeV for FoCal pseudo-data and for QCD calculations with various nPDF versions, with and without inclusion of LHCb D-meson measurements and FoCal pseudo-data, as indicated. The prior prediction for nNNPDF3.0 (no LHCb) (gray band) is reweighted using Bayesian inference, taking into account the FoCal pseudo-data (see Fig. 20). The red line and shaded band denote the resulting posterior distribution and its uncertainty. Recent constrains provided by D-meson measurements by the LHCb experiment [22] are denoted by a blue shaded band for reference.

about 50 % is observed when including the FoCal data, illustrating the potential of FoCal measurements to constrain global PDF fits.

The blue line and shaded band show the effect of the inclusion of recent measurements of D-meson production at forward rapidity by the LHCb experiment [22], which likewise results in significant reduction of nPDF uncertainties [21]. While this achievement is notable, it does not lessen the importance of a complementary measurement based on isolated prompt photons, which provides a meaningfully independent probe of low-$x$ structure and dynamics.

The isolation procedure suppresses the fragmentation photon contribution, making the measurement of isolated prompt photons a theoretically clean probe of the underlying gluon distributions, without the need to incorporate hadronic fragmentation functions, which are not constrained with high precision. This is not the case for D-mesons, where fragmentation functions are required to describe the hadronization process and other final-state effects might become relevant [23].

In our view, exploration of the low-$x$ phase-space, where gluon saturation is expected to be sizeable, requires a multi-messenger approach [2]. This is in line with the philosophy of nPDFs, which require a *global* analysis of all available data. Furthermore, the inclusion of FoCal prompt–photon data in global PDF fits will provide new insight into factorization and universality in nuclear environments. In particular, corrections due to final state re-scattering of the outgoing partons propagating in the nuclear medium [24, 25] are not required for prompt photons. This issue has been noted by the authors of the nCTEQ15 nPDF [26].

## 5 Neutral mesons

Neutral mesons decaying fully into photons or electrons can be reconstructed using the electromagnetic showers in FoCal-E. The most abundant mesons decaying electromagnetically are $\pi^0$, $\eta$, and $\omega$. Vector mesons decaying via di-electrons, such as $\phi$, J/$\psi$, $\psi(2S)$, and $\Upsilon$, and the $W^{\pm}$ and $Z^0$ weak bosons can also be reconstructed.

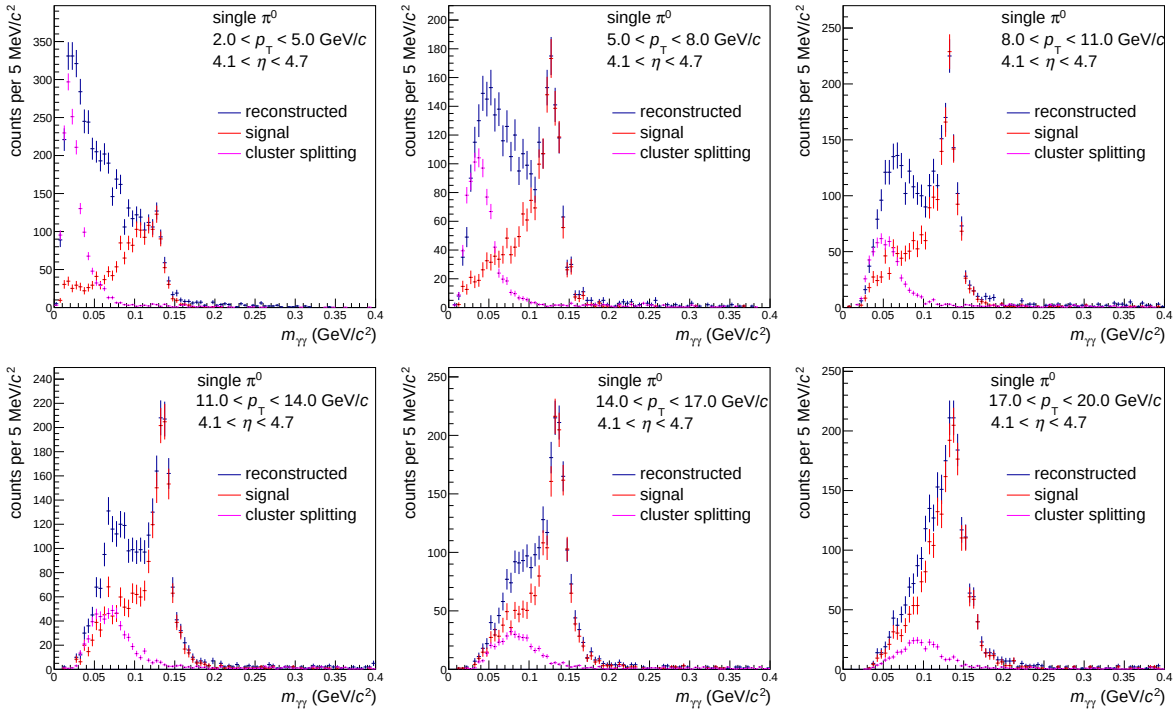


**Fig. 22:** FoCal invariant mass distribution for two-cluster pairs reconstructed from the single-$\pi^0$ simulation in $4.1 < \eta < 4.7$, in successive $p_{\mathrm{T}}$ intervals. Statistical errors are due to the statistical precision of the simulated dataset.

### 5.1 Reconstruction in single $\pi^0$ events

The reconstruction performance of $\pi^0$ is important both for $\pi^0$ measurements themselves and the for prompt photon analysis, and is discussed in detail in this section. This study uses single-$\pi^0$ simulated events generated by a box simulation with the magnitude of the momentum vector of the generated mesons distributed uniformly between 0 and 2.5 TeV. The $\pi^0$ mesons are decayed using their natural decay branching, where the two-photon channel dominates. Since the decay is electromagnetic, the resulting photon pair behave as primary particles, which appear to originate from the nominal interaction vertex. After reconstruction, all clusters passing basic quality checks are combined into pairs.

Figures 22 and 23 show the invariant mass distribution obtained by this procedure for several $p_{\mathrm{T}}$ intervals in $4.1 < \eta < 4.7$ and $4.7 < \eta < 5.3$. All distributions exhibit a peak near the PDG $\pi^0$ mass, but with distribution shape depending on the $p_{\mathrm{T}}$ of the cluster pair. The distribution shape varies both in the $\pi^0$ mass region and below, where a distinct peak is observed at low $p_{\mathrm{T}}$.

To clarify its origin, a fit of these distributions is performed. A template for the primary component of the invariant mass distribution is formed using cluster pairs, which best match the two photons from the $\pi^0$ decay. This is called "signal" shape, and is shown in the figures as a red histogram. An additional component arises from cluster splitting for single primary photons (Sec. 2.3), which generates correlated background. For these single-$\pi^0$ events, this background component is due both to clusters from the same photon and from different photons. The single-photon component shape is determined by single-photon simulations (Sec. 2.3). The template the shape of the splitting component is shown in the figures

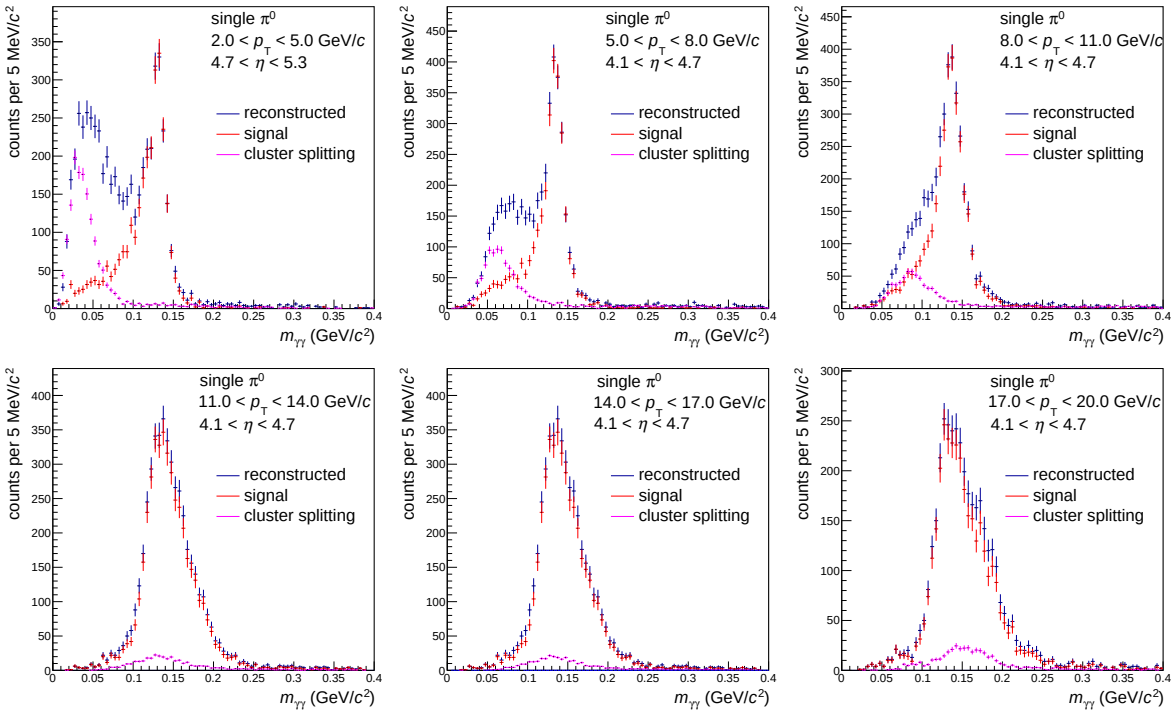


**Fig. 23:** FoCal invariant mass distribution for two-cluster pairs reconstructed from the single-$\pi^0$ simulation in $4.7 < \eta < 5.3$, in successive $p_{\mathrm{T}}$ intervals. Statistical errors are due to the statistical precision of the simulated dataset.

as the magenta distributions ("cluster splitting"), and is seen to contribute primarily to the low mass region. A fit to the invariant mass distribution using these two components shows that the invariant mass distribution is well described in the low-mass and $\pi^0$ mass ranges, but not the intermediate mass region ($0.05 < m_{\gamma\gamma} < 0.1$ GeV$/c^2$). This is due to the correlated component from pairs of split clusters from different photons, which is not accounted for in the template. This component will be studied in future.

For a specified $(p_{\mathrm{T}}, \eta)$ intervals the product of reconstruction efficiency and kinematic acceptance is defined as

$$\varepsilon(p_{\mathrm{T}}, \eta) = \frac{N^{\mathrm{rec},\pi^0}(p_{\mathrm{T}}, \eta; 70 < m_{\gamma\gamma} < 180\ \mathrm{MeV}/c^2)}{N^{\mathrm{gen},\pi^0}(p_{\mathrm{T}}, \eta)}, \tag{12}$$

where $N^{\mathrm{rec},\pi^0}$ is the number of reconstructed cluster pairs, which are matched to a photon pair from a $\pi^0$ (see Sec. 2.4) and have mass in the interval $[70, 180]$ MeV$/c^2$, and $N^{\mathrm{gen},\pi^0}$ is the number of $\pi^0$ mesons generated in the same kinematic interval and decaying to photon pairs. To suppress false matches due to cluster splitting, for a given generated $\pi^0$ only the best matching reconstructed $\pi^0$ candidate is selected, based on the quadrature sum of the energy difference at detector and generator level of the two $\pi^0$ decay photons.

Figure 24, left panel, shows the $p_{\mathrm{T}}$ dependence of the $\pi^0$ product of kinematic acceptance and reconstruction efficiency for three $\eta$ intervals. The kinematic acceptance is near unity except for $p_{\mathrm{T}} < 1$ GeV$/c$ ; the distribution therefore shows primarily the reconstruction efficiency, which has value of up to 75%, dropping towards high $p_{\mathrm{T}}$. The magnitude of the efficiency is determined by the fraction of the sensitive area of the detector and by the intrinsic efficiency of the clustering algorithm in separating two clusters from a $\pi^0$ decay. The $p_{\mathrm{T}}$ value where the efficiency starts to drop is $\eta$-dependent, with lowest value ($\sim 10$ GeV$/c$ ) at forward-most rapidity, due to the boost. The parameters of the clusterization parameters can be tuned to obtain better performance in certain kinematical regions, such as at high $\pi^0$ energy.

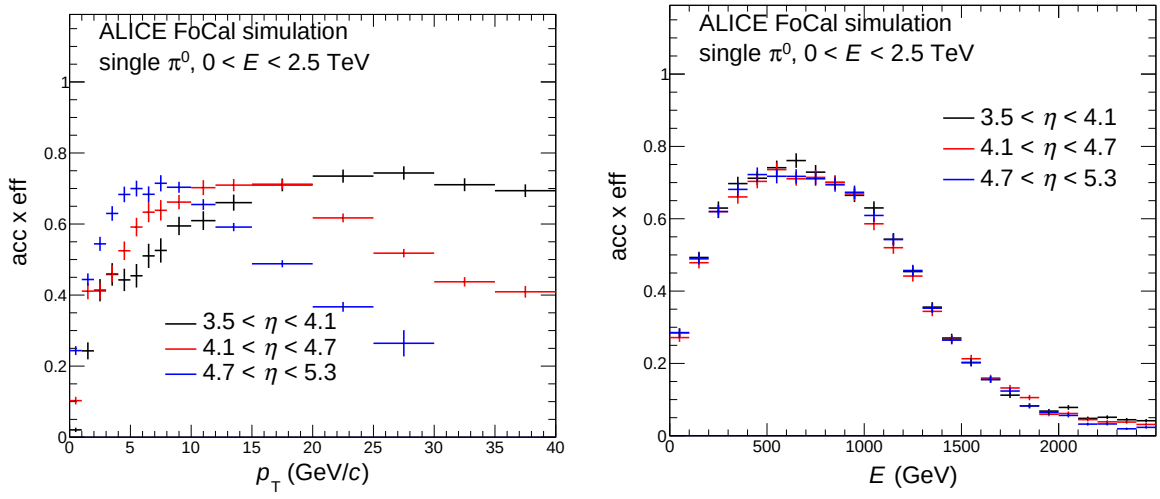


**Fig. 24:** Product of acceptance and efficiency as a function of $p_T$ (left) and energy (right). The distributions are shown for three $\eta$ intervals.

An example of such an improvement is shown in Appendix B.2.

The right panel of Fig. 24 shows the $\pi^0$ efficiency as a function of energy for the same $\eta$ ranges. It exhibits no $\eta$ dependence, as expected since the $\pi^0$ energy governs the photon decay kinematic. The efficiency has maximum of 75%, decreasing above $E = 1$ TeV due primarily to the decreasing distance between $\pi^0$ decay photons.

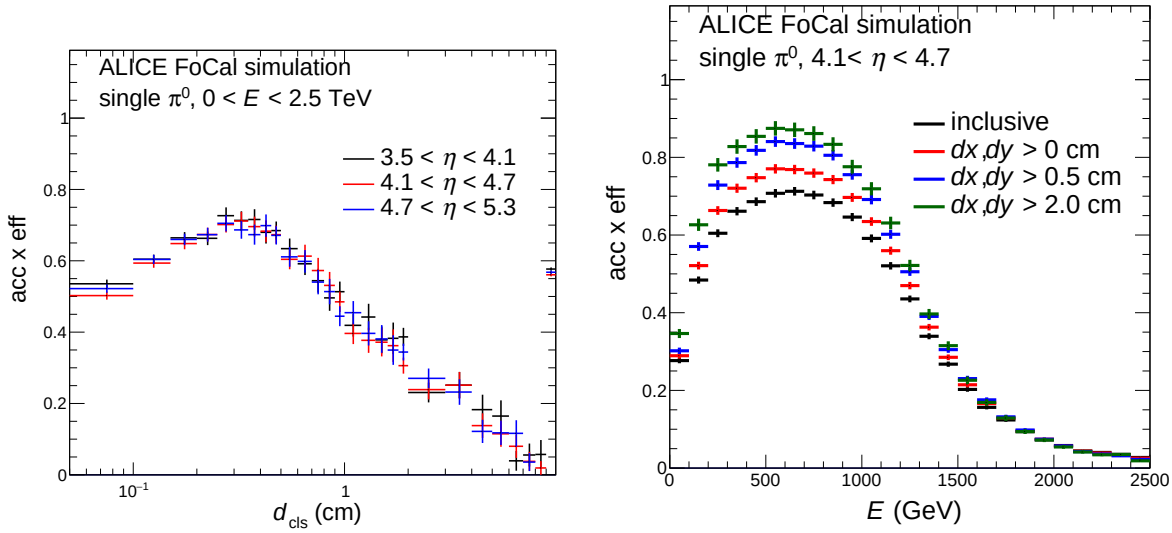


**Fig. 25:** Product of acceptance and efficiency. Left: as a function of the distance between the $\pi^0$ decay photons at the FoCal front surface ($d_{cls}$) for three $\eta$ intervals. Right: in $4.1 < \eta < 4.7$ for different intervals in distance of $\pi^0$ incidence from the tower edge (see text for details).

The left panel of Fig. 25 shows the product of acceptance and efficiency as a function of the distance between the $\pi^0$ decay photons at the FoCal front surface, $d_{cls}$. There is a strong correlation between the $\pi^0$ energy and the distance between the two decay photons, with the highest energies dominating at low $d_{cls}$, and the lowest ones at large $d_{cls}$. As expected, the $\pi^0$ efficiency drops for separation distances $d_{cls} < 1$ mm and is at its maximum for $d_{cls}$ of a few millimeter. For $d_{cls} > 1$ cm the efficiency decreases with increasing distance because, while FoCal separates clusters well at distances of more than 1 cm, $\pi^0$ mesons, which decay with such a large separation distance predominantly have one low energy photon,

which has poor resolution and is affected by cluster splitting. However, such effects impact only a small fraction of the $\pi^0$ population; the majority of the $\pi^0$ decays have inter-shower separation less than 1 cm.

The efficiency is affected by the FoCal insensitive area. The right panel of Fig. 25 illustrates this by showing the efficiency as a function of energy for different intervals in $\pi^0$ incidence of the FoCal front face relative to the edges of the FoCal modules. If no such selection is made, the efficiency is by definition the as in Fig. 24, with value 70%. For the population $\pi^0$ which are incident in the interior of a module, the efficiency increases with the increase of the distance from the edge, attaining 90% for $\pi^0$ at distance greater than 2 cm from the vertical and horizontal edges.

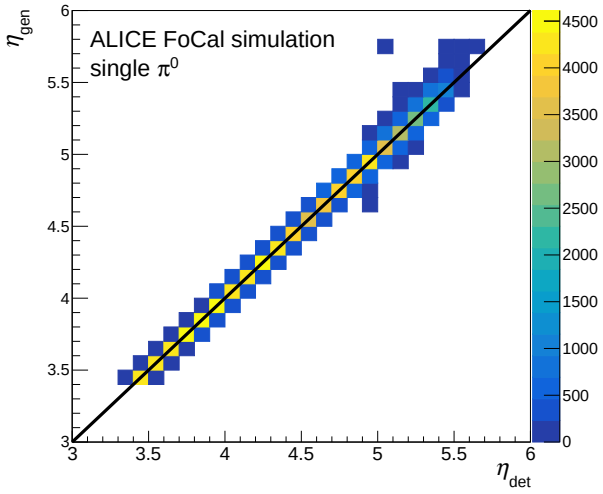


**Fig. 26:** Correlation of $\eta$ of $\pi^0$ clusters pairs at the generator and reconstructed levels.

Figure 26 shows the correlation of $\eta$ of $\pi^0$ pairs at the generator and reconstructed levels. The distribution is largely diagonal, indicating only limited detector-level smearing in $\eta$.

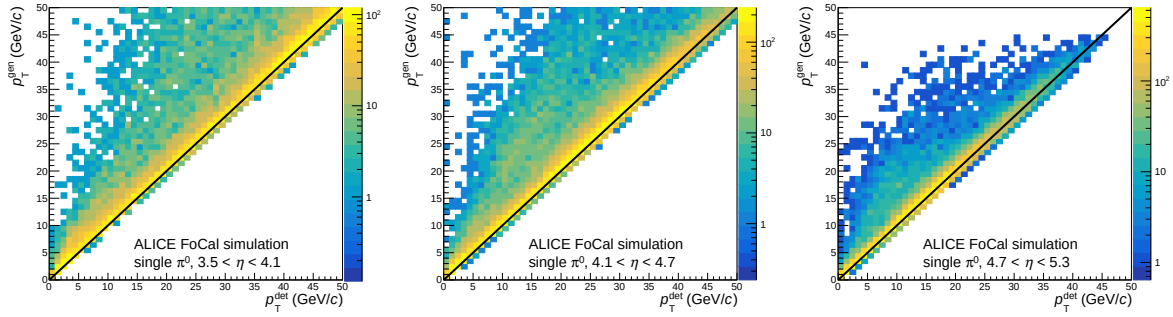


**Fig. 27:** Correlation of $p_{\mathrm{T}}$ of $\pi^0$ clusters pairs at the generator and reconstructed levels, for selected ranges in $\eta$ of the pair.

Similarly, Fig. 27 shows the correlation of generator-level and reconstructed $p_{\mathrm{T}}$ of $\pi^0$ cluster pairs, in selected $\eta$ intervals. These correlations are likewise predominantly diagonal, indicating that the main effect at play is the detector resolution, with only a small non-linearity of the reconstructed $p_{\mathrm{T}}$. However, an off-diagonal component is also observed: a fraction of the $\pi^0$ candidates are reconstructed at $p_{\mathrm{T}}$ that is systematically lower than the corresponding generator level $p_{\mathrm{T}}$. This is observed for all three $\eta$ intervals and can be ascribed to the combination of several effects, including cluster splitting, secondary interactions in the material in front of FoCal, and energy lost in insensitive detector regions.

### 5.2 Measurement of $\pi^0$, $\eta$, and $\omega$ in pp collisions

In this section, we study the reconstruction performance for $\pi^0$, $\eta$, and $\omega$ mesons in pp collisions, which differs from the previous section by taking into account environmental effects, notably the underlying

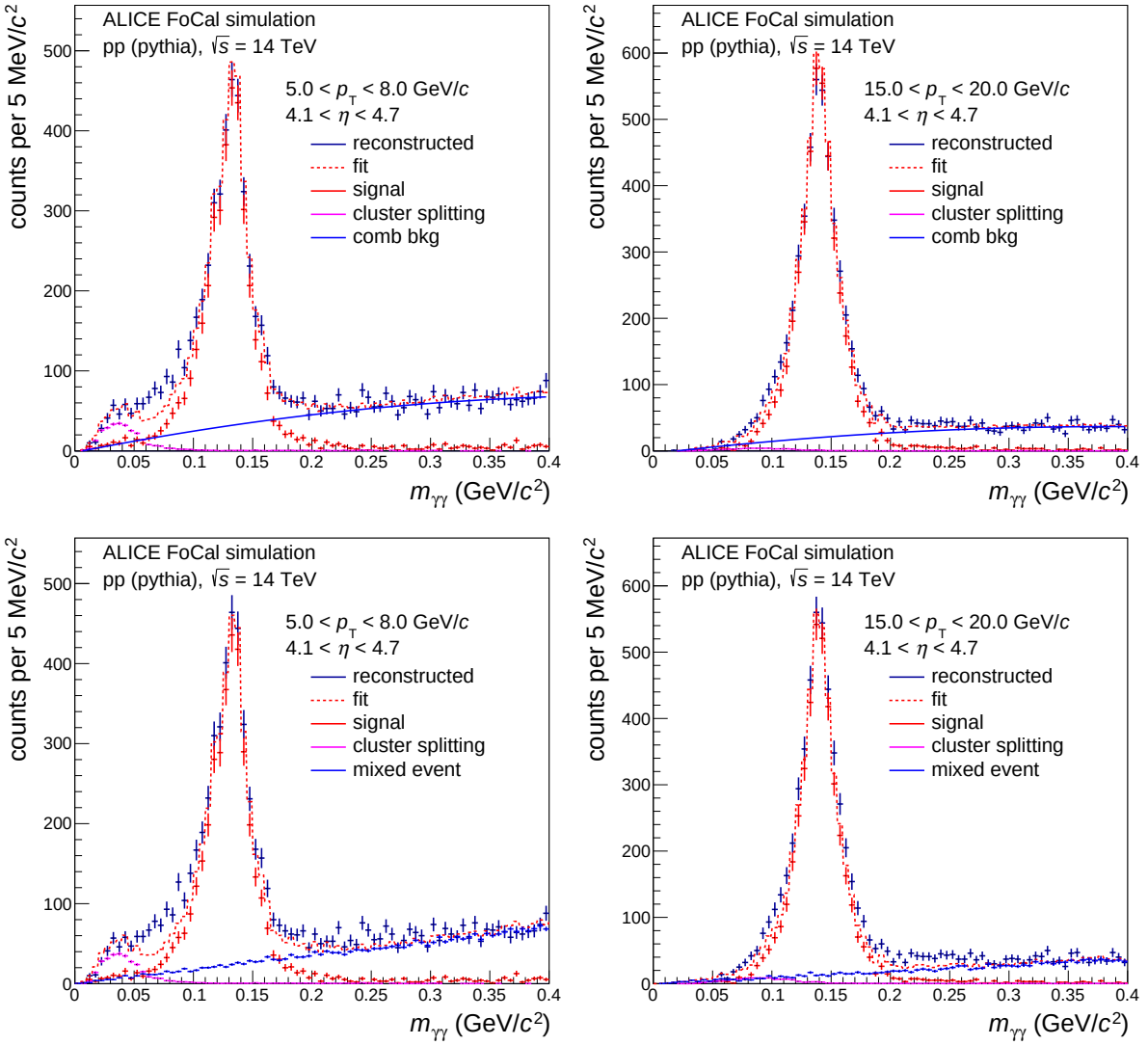


**Fig. 28:** Di-photon invariant mass distributions simulated by PYTHIA for pp collisions at $\sqrt{s} = 14$ TeV, for pairs with at least one high-$p_{\mathrm{T}}$ $\pi^0$ in the FoCal acceptance and pair $5.0 < p_{\mathrm{T}} < 8.0$ GeV$/c$ (left) and $15.0 < p_{\mathrm{T}} < 20.0$ GeV$/c$ (right). Distributions are fitted with a function accounting for signal, cluster splitting and combinatorial background. The combinatorial background is constructed using a polynomial function (upper panels) or event mixing (lower panels).

event that adds combinatorial background. Events are generated by PYTHIA triggered on the presence of one of these mesons within the FoCal acceptance and above a specified $p_{\mathrm{T}}$ threshold.

Figure 28 shows the cluster pair reconstructed invariant mass distributions in $4.1 < \eta < 4.7$ and selected $p_{\mathrm{T}}$ intervals. The signal is extracted using several fitting procedures. We focus here on fitting using a cocktail with several components accounting for signal shape, cluster splitting, and combinatorial background, motivated by the findings in the previous section for single $\pi^0$ events. The signal shape component is obtained from the distribution of cluster pairs that are matched to true photon pairs from a $\pi^0$ decays. The cluster-splitting component is obtained by performing an invariant mass analysis for single-photon events, where no signal contribution occurs. The combinatorial background is determined using three different approaches:

1. fit using a polynomial function

2. event mixing method, where underlying correlations are removed by considering only pairs of clusters formed from different collision events
3. rotational background method, where underlying correlations are removed by considering only clusters pairs from the same event with one of the cluster positions rotated with by a random azimuthal angle

Each approach to determine the combinatorial background is discussed in the following.

Figure 28 shows the signal extraction using either a polynomial function (upper panels) or the mixed-event technique (lower panels) to describe the combinatorial background. Similar performance is observed for the first two combinatorial background models, with slightly better performance for the fit, in particular at higher masses. The invariant mass distribution below the $\pi^0$ peak ($0.05 < m < 0.1$ GeV$/c^2$) is not well-described by either fit model, which could be due to unaccounted correlated background such as pairs from splitting of a single $\pi^0$ photon, or secondary clusters from the other $\pi^0$ photon. Further study is needed of both clustering algorithm and analysis selection to fully account for the background distribution.

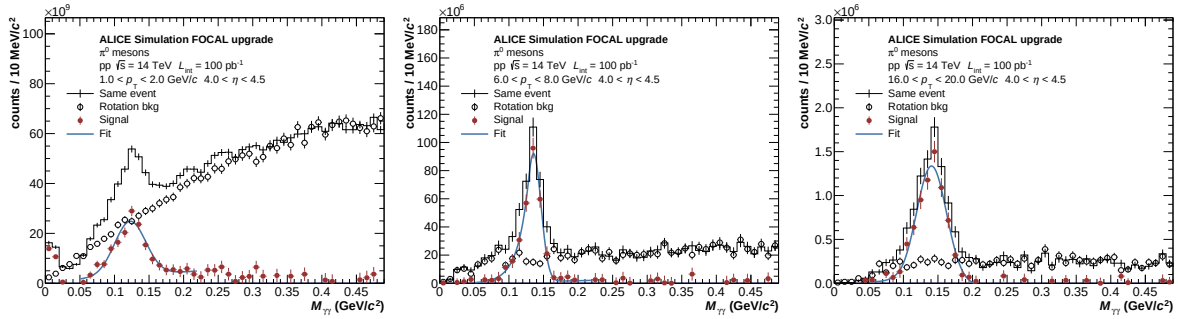


**Fig. 29:** Di-photon invariant mass distribution in pp collisions at $\sqrt{s} = 14$ TeV generated by PYTHIA, with events with at least one high-$p_{\mathrm{T}}$ $\pi^0$ within the FoCal acceptance. The background distribution is determined by random rotation of the clusters from the same event. The yield corresponds to integrated luminosity of 100 pb$^{-1}$. Vertical axis scale gives counts per bin corresponding to $\mathscr{L}_{\mathrm{int}} = 100$ pb$^{-1}$, while the jitter of the points is due to the statistical precision of the simulated dataset.

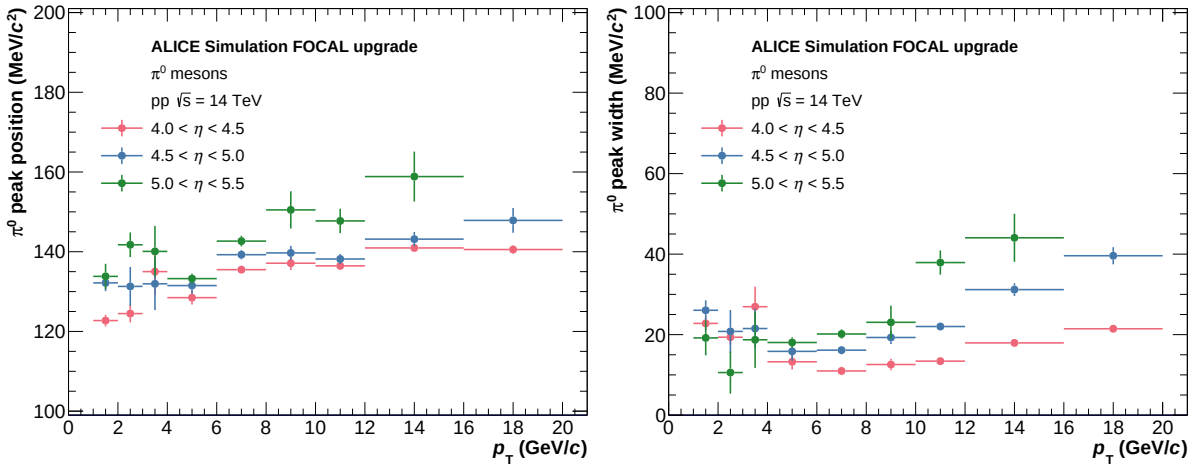


**Fig. 30:** Transverse momentum dependence of the reconstructed $\pi^0$ signal mass pole and width. Error bars are due to the statistical precision of the simulated dataset.

Figure 29 shows the signal extraction, where the combinatorial background is described using the rotation method. Good description of the background is observed and the usage of an additional background

template to describe cluster splittings it therefore not required. The background-subtracted invariant mass distribution is fitted using the Crystal Ball function [12]. Figure 30 shows the mass and Gaussian core width extracted from the fit, as a function of $p_{\mathrm{T}}$.

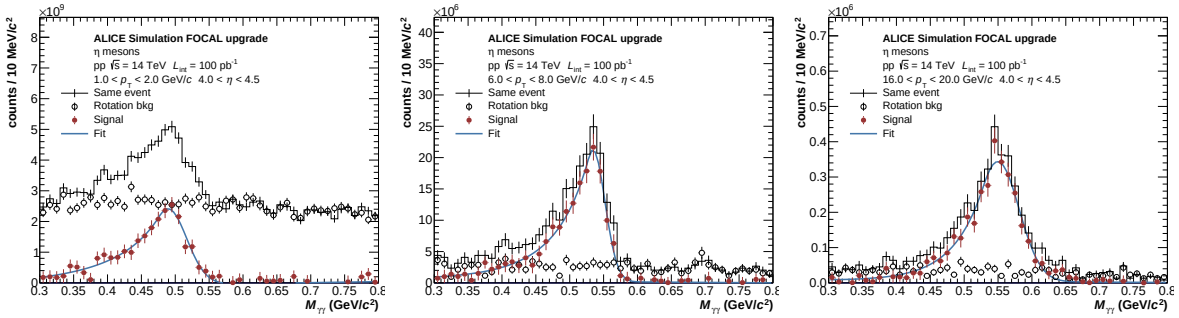


**Fig. 31:** Same as Fig. 29, for $\eta$-mesons. Vertical axis scale gives counts per bin corresponding to $\mathscr{L}_{\mathrm{int}} = 100\ \mathrm{pb}^{-1}$, while the jitter of the points is due to the statistical precision of the simulated dataset.

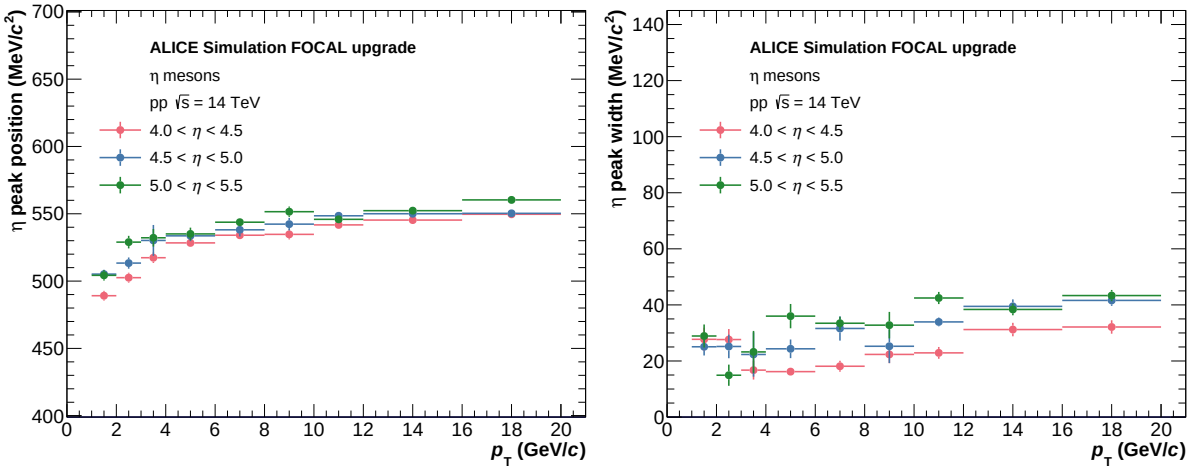


**Fig. 32:** Transverse momentum dependence of the reconstructed $\eta$ signal mass pole and width.

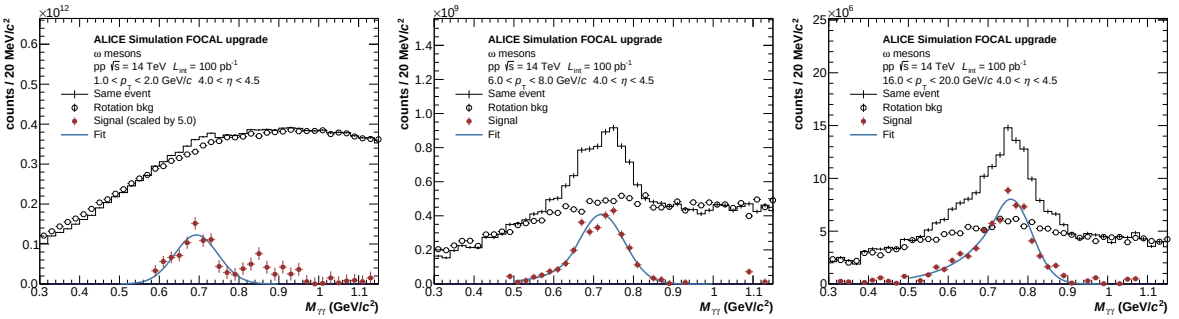


**Fig. 33:** Same as Fig. 29, for $\omega$-mesons.

Figures 31, 32 and 33 show similar analyses for $\eta$ and $\omega$ mesons. The $\eta$-meson is reconstructed from its two-photon decay mode, while the $\omega$ meson is reconstructed using the $\pi^0 + \gamma$ decay channel.

### 5.3 Pileup effects

The interaction rate during LHC Run 4 can be as high as 1 MHz for both pp and p–Pb collisions. Due to the relatively slow readout of the FoCal-E pixel layers, several collisions can overlap within the same readout window, with an average of about 10 pileup collisions. However, FoCal-E pad layers

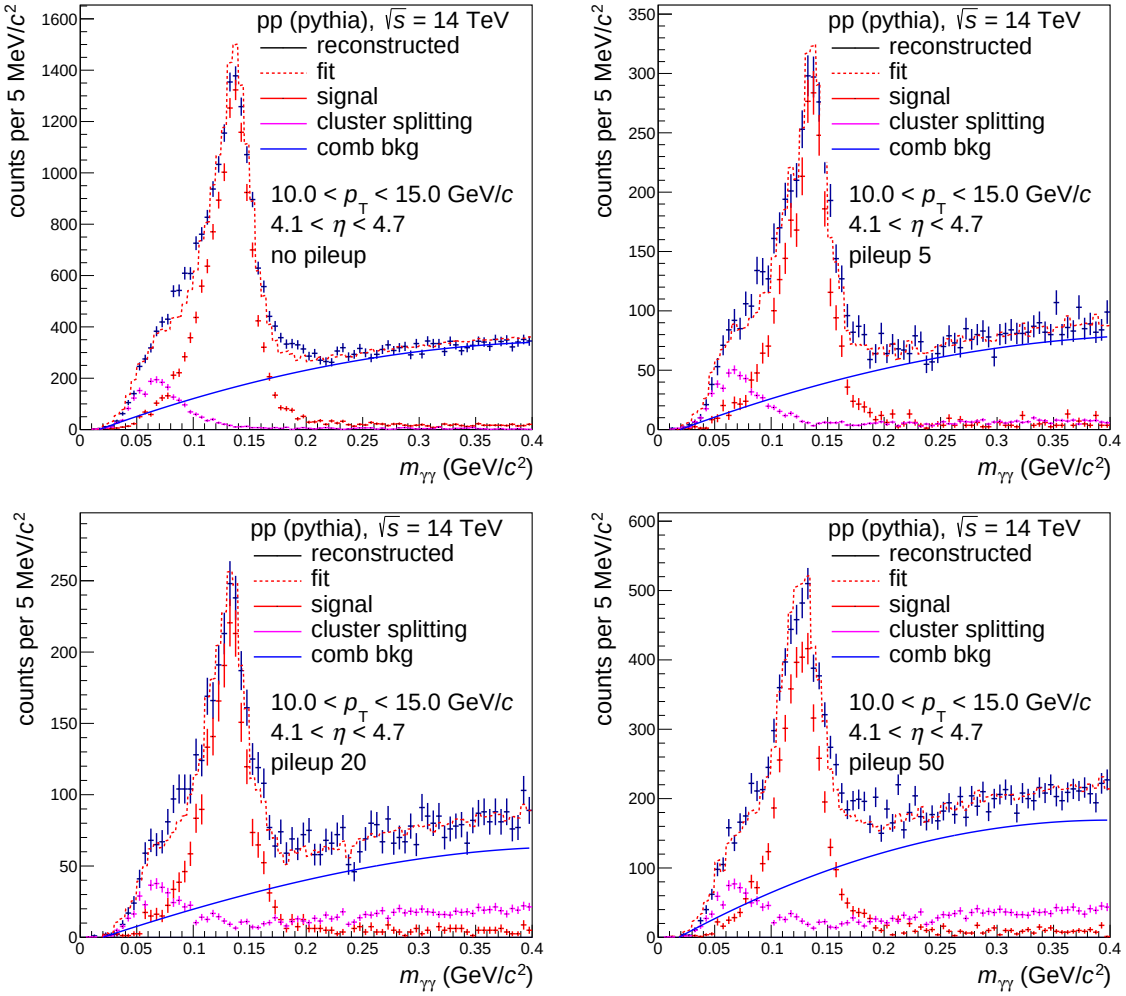


**Fig. 34:** Di-photon invariant mass distribution in pp collisions at $\sqrt{s} = 14$ TeV generated by PYTHIA, with events with at least one high-$p_T$ $\pi^0$ within the FoCal acceptance, and with pileup corresponding to multiple MB pp collisions superimposed on the triggered event (see text for details).

are sufficiently fast to resolve collisions from different bunches. While cluster energy is measured in the pad layers, the pixel layers are used to separate close clusters such as those from $\pi^0$ decay, and their performance is affected by pileup.

To study pileup effects, hybrid of pp collisions were generated based on PYTHIA, with the "signal" event being an event with a $\pi^0$ produced in the FoCal acceptance, and the "background" comprising several superimposed minimum bias pp collisions. The simulated hits for the signal event are digitized as usual, while the background hits were digitized only in the pixel layers since it the pads are not affected by pileup. All digits are then summed, and the standard clusterization algorithm is run.

Figure 34 shows the two-cluster invariant mass distribution for the cases of no pileup, 5, 20, and 50 pileup events. The fitting procedure described above, which employs signal, cluster splitting, and polynomial background components, is applied. The $\pi^0$ signal can be extracted in all cases. A decrease of the signal-to-background ratio with increasing number of pileup collisions can be observed. Detailed studies of the reconstruction performance show also an increase of the cluster size in the pixel layers, i.e. increase in the number of cells in a cluster, and an overall increase in the number of reconstructed clusters per event with increasing number of pileup events. These effects are expected due to the increase in occupancy in the pixel layers, which lead to shower overlaps and more cluster splitting.

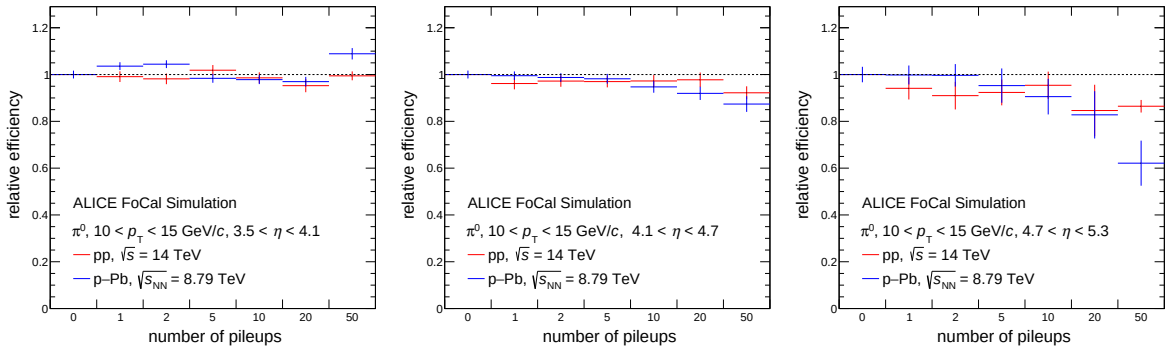


**Fig. 35:** Product of acceptance and efficiency for $\pi^0$ with $10 < p_{\mathrm{T}} < 15$ GeV/$c$ as a function of the number of pileup events, relative to the efficiency without pileup. Efficiencies are shown for both pp and p–Pb collisions differentially in $\eta$ within the FoCal acceptance. Error bars correspond to those of the MC dataset.

Figure 35 shows the relative efficiency as a function of the number of pileup collisions for pp collisions at $\sqrt{s} = 14$ TeV and p–Pb collisions at $\sqrt{s_{\mathrm{NN}}} = 8.79$ TeV in selected $\eta$ intervals, for pileup ranging from zero to 50 superimposed MB pp events. At low $\eta$ (left panel), there is no significant impact from pileup. The occupancy grows rapidly for larger $\eta$ where the relative $\pi^0$ efficiency decreases, with the largest effect for p–Pb collisions with 10 or more pileup collisions. In pp collisions, the lowest efficiency (85%) is observed at forward rapidity for 50 pileup events. The main reason for the decrease in efficiency with high pile-up is the worsening quality of the cluster reconstruction in the pixel layers (cluster splitting, attachement of additional cells from unrelated showers) which affects the reconstruction of the two-shower configurations related to the $\pi^0$ decays.

## 6 Jets

The FoCal jet performance is assessed using simulated events for pp collisions at $\sqrt{s}$=14 TeV, generated by PYTHIA8 with the hard-process selection $\hat{p}_{\mathrm{T}}^{\mathrm{min}} = 5$ GeV. Detector-level events are simulated using the FoCal-H sandwich design.

### 6.1 Jet reconstruction

Jet reconstruction at the particle level utilizes primary particles and decay daughters within the FoCal acceptance. Jet reconstruction at the detector level utilizes FoCal-E clusters ( Sec. 2.3) with zero mass assigned, and FoCal-H tower signals. No cluster or cell energy threshold cut is applied.

Jet reconstruction at both the particle and detector level utilizes the anti$-k_{\mathrm{T}}$ clustering algorithm [27] with E-scheme recombination [28]. Jets are accepted for further analysis if their centroid is within $3.4+R < \eta^{\mathrm{jet}} < 5.5-R$, where $R$ is the jet resolution parameter. For a jet of radius $R = 0.6$, this results in the pseudorapidity acceptance $4.0 < \eta^{\mathrm{jet}} < 4.9$.

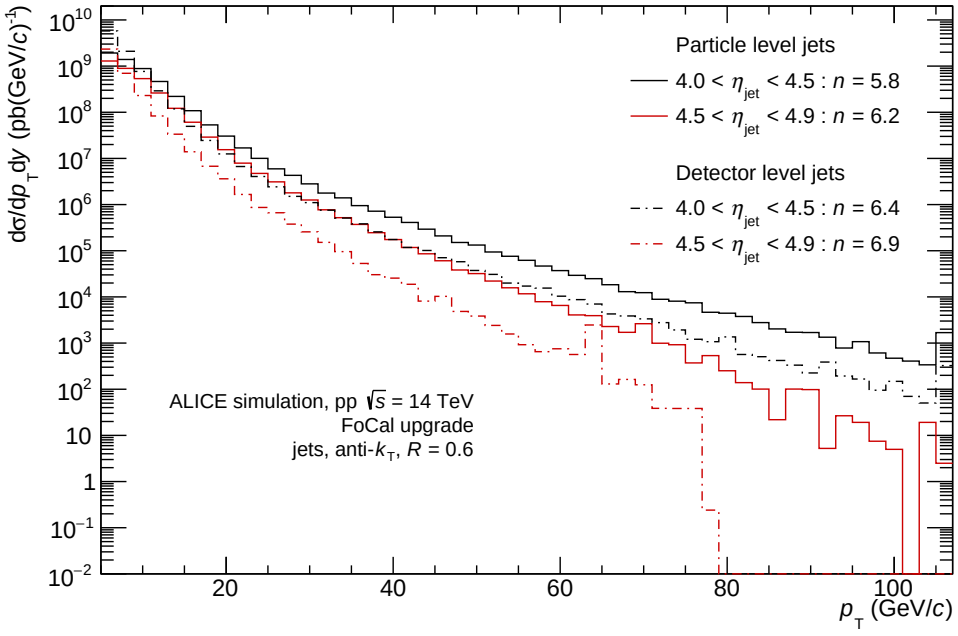


**Fig. 36:** The $p_{\mathrm{T}}$-differential inclusive jet cross section for pp collisions at $\sqrt{s}$=14 TeV, generated by PYTHIA8. Jets are reconstructed using anti$-k_{\mathrm{T}}$ with $R$=0.6 and are required to have their centroid within the FoCal acceptance. Distributions are shown for particle-level (solid) and detector-level jets (dot-dashed) in two intervals of $\eta^{\mathrm{jet}}$. The value of $n$ is the power determined by a power-law fit to spectrum.

Figure 36 shows the $p_{\mathrm{T}}^{\mathrm{jet}}$-differential inclusive jet cross section generated by PYTHIA8 for pp collisions at $\sqrt{s}$=14 TeV, for anti$-k_{\mathrm{T}}$ jets with $R$=0.6 in the FoCal acceptance. A power-law fit to the spectra yields power $n \sim 6$, which is not significantly different than the shape of the inclusive jet spectrum at midrapidity. Both particle-level and detector-level distributions are shown. While the shape of the particle-level and detector-level distributions are similar (detector level $n \sim 6.2-6.8$), the detector-level distributions are shifted downwards markedly in $p_{\mathrm{T}}^{\mathrm{jet}}$. This shift also indicates the magnitude of correction needed.

Jets at the particle and detector level in the same event are matched based on their phase-space separation $\Delta R$,

$$\Delta R = \sqrt{\Delta y^2 + \Delta\phi^2}, \tag{13}$$

where $\Delta y$ and $\Delta\phi$ are the separation of the pair in rapidity and azimuthal angle. For each detector-level jet, the particle-level jet with smallest $\Delta R$ is selected as its match. The value of $\Delta R$ is further required to be less that $0.6R$. This parameter was chosen to ensure that the jets have sufficient overlap, to reduce the contribution from fake matches.

Jet reconstruction performance is quantified by the the relative energy or $p_{\mathrm{T}}$ difference at the detector and particle levels for matched jets,

$$\Delta E = \frac{E^{\mathrm{det}} - E^{\mathrm{part}}}{E^{\mathrm{part}}},$$
$$\Delta p_{\mathrm{T}} = \frac{p_{\mathrm{T}}^{\mathrm{det}} - p_{\mathrm{T}}^{\mathrm{part}}}{p_{\mathrm{T}}^{\mathrm{part}}}. \tag{14}$$

The Jet Energy Scale (JES) is characterized by the mean of the $\Delta E$ and $\Delta p_{\mathrm{T}}$ distributions, while the Jet Energy Resolution (JER) is characterized by their RMS.

### 6.2 Geometric considerations

Jets are multi-hadron objects which subtend finite area in $(\eta, \varphi)$, governed primarily by the reconstruction resolution parameter $R$. Before discussing jet measurement performance we first consider kinematic effects for jet reconstruction in the very forward direction, taking into account their finite area.

**Table 3:** Spatial distances for phase-space intervals in a plane transverse to the beamline at the front face of FoCal ($D = 700$ cm). First column: selected values of $\eta$ in the FoCal acceptance; second column: radial distance from beamline (Eq. 15); third column: spatial distance for phase-space increment $\Delta\eta = 0.4$; fourth column: spatial distance for phase-space increment $\Delta\varphi = 0.4$.

| $\eta$ | $r$ (cm) | $r(\eta - 0.4) - r(\eta)$ (cm) | $r \cdot (\Delta\varphi = 0.4)$ (cm) |
|---|---|---|---|
| 3.4 | 46.7 | | 18.7 |
| 3.8 | 31.3 | 15.4 | 12.5 |
| 4.2 | 21.0 | 10.3 | 8.4 |
| 4.6 | 14.1 | 6.9 | 5.6 |
| 5.0 | 9.4 | 4.6 | 3.8 |
| 5.4 | 6.3 | 3.1 | 2.5 |
| 5.8 | 4.2 | 2.1 | 1.7 |

The intrinsic transverse dimensions of EM and hadronic showers in FoCal have significant impact on jet reconstruction performance, since phase space becomes spatially very compact at high $\eta$. To quantify this effect we note that, in a plane transverse to the beam at distance $D$ from the interaction vertex, the radial distance $r$ from the beamline at pseudorapidity $\eta$ is

$$r \approx \frac{2D}{e^{\eta}}, \tag{15}$$

where the small-angle approximation has been used to simplify the expression. In other words, phase-space becomes spatially exponentially small at high $\eta$. Table 3 gives representative values of $r$ as a function of $\eta$ on the front face of FoCal ($D = 700$ cm, $3.2 < \eta < 5.8$), together with spatial intervals corresponding to a characteristic jet size $\Delta\eta \sim \Delta\varphi \sim 0.4$.

Since the structure of FoCal-E and FoCal-H are uniform, the transverse extent of showers in them is independent of $\eta$. The Moliere radius of FoCal-E is about 1 cm (Sec. 2), while showers in FoCal-H have transverse extent exceeding 10 cm. Figure 37 illustrates the effect of the relationship between phase-space and spatial coordinates for FoCal-H. The figure shows the FoCal-H shower profile for charged pions averaged over 10K simulated showers, which sample the full FoCal acceptance but are aligned by

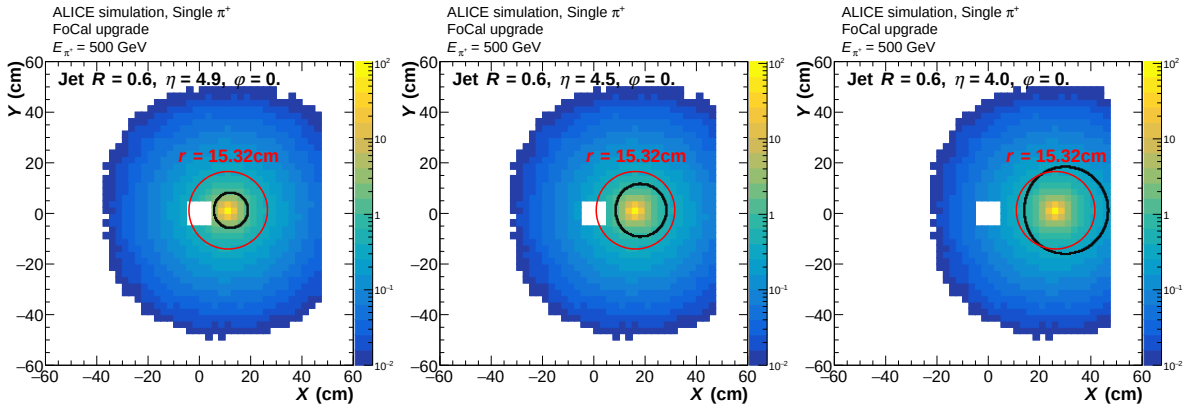


**Fig. 37:** Averaged shower profile in FoCal-H of 10K overlapping showers induced by single charged pions with energy $E = 500$ GeV. Shower profile is centered on phase space coordinates $(\eta, \varphi)$ =(4.9,0) (left), (4.5,0) (middle), or (4.0,0) (right). The $z$-axis is the average energy deposited in each FoCal-H cell of size $2.5 \times 2.5$ cm. The red circle visualizes the nuclear interaction length of Cu.

hand at the same location in the figure; this procedure therefore generates the "average" FoCal hadronic shower profile. The three panels center the shower at $(\eta, \varphi)$ =(4.9,0), (4.5,0) or (4.0,0). The red circle in each panel (which corresponds approximately to the nuclear interaction length of Cu) contains 81% of the shower energy in $(x, y)$ space. The black contours show circles in $(\eta, \varphi)$ space with radius $R = 0.6$ centered on $(\eta, \varphi)$ =(4.9,0), (4.5,0) or (4.0,0). The contour for $\eta = 4.9$ captures only a limited fraction of the jet energy, which will generate a large shift in JES (Eq. 14). A larger jet energy fraction is captured by the $R = 0.6$ phase space contour for smaller $\eta$, and correspondingly smaller shift in JES is expected. The following sections explore these effects quantitatively.

### 6.3 Single-particle jet showers

We first consider jet reconstruction for single energetic charged and neutral pions, which are the simplest probes subject to the phase space effects discussion in Sec. 6.2. Samples of charged and neutral pions were generated separately and the jet finder was run on the combination of FoCal-E clusters and FoCal-H tower signals.

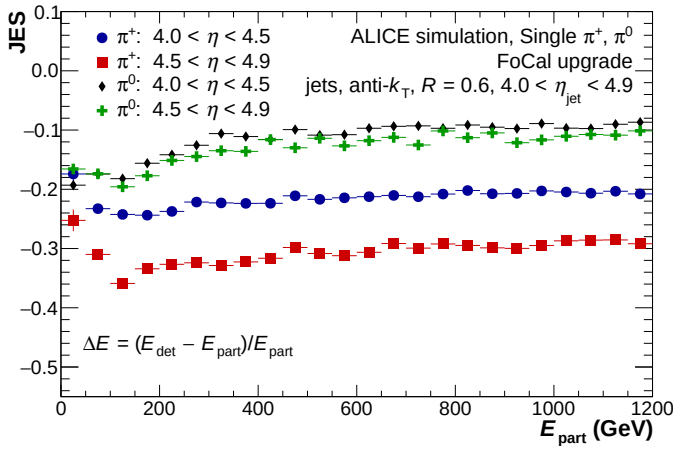


**Fig. 38:** JES for single charged and neutral pions vs. particle-level energy.

Figure 38 shows the JES versus particle-level energy of the reconstructed jets (anti$-k_{\mathrm{T}}$, $R = 0.6$) for single pions in two $\eta^{\mathrm{jet}}$ intervals. A value of JES (Eq. 14) below zero means that a fraction of the total jet energy escapes the jet reconstruction, resulting in a deficit in reported jet energy. The phase-space effects identified in Sec. 6.2 are readily visible:

– Jet reconstruction of EM showers in FoCal-E induced by $\pi^0$ probes misses a moderate fraction of the total energy (10–20%), independent of $\eta$. This is consistent with the FoCal-E Moliere radius being smaller than the spatial extent of jets with resolution parameter $R = 0.6$.

– Jet reconstruction of hadronic showers, largely in FoCal-H, exhibits larger energy deficit (JES about $-25\%$ to $-30\%$), consistent with the larger transverse shower size in FoCal-H. The magnitude of the deficit is largest at high $\eta$, consistent with the exponential spatial contraction of phase-space (Eq. 15).

### 6.4 Jet response in pp collisions

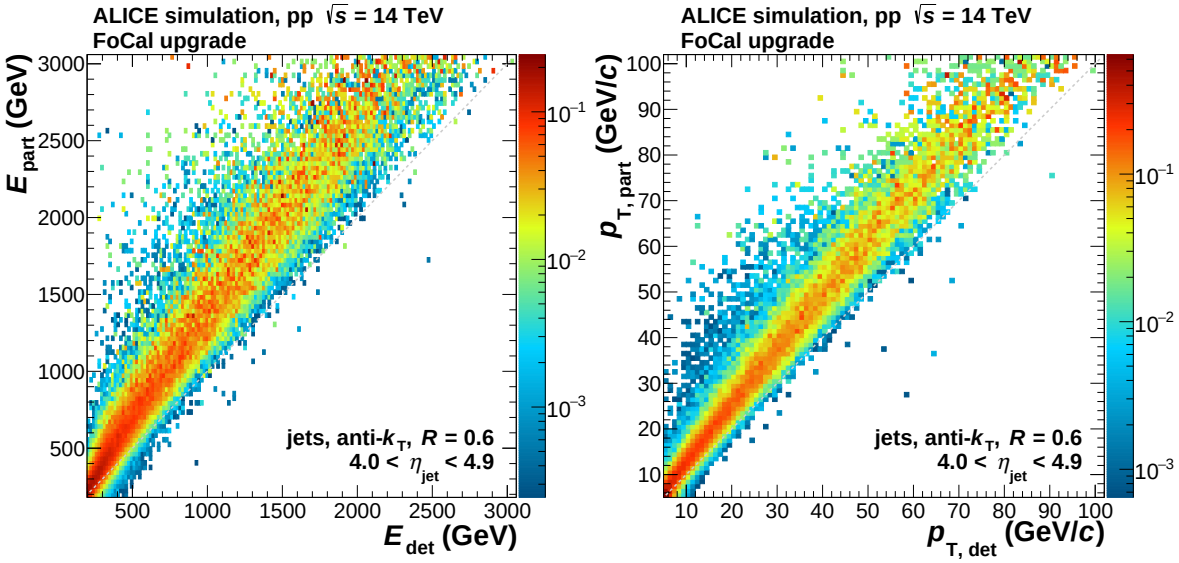


**Fig. 39:** Response matrices in terms of energy (left) and $p_{\mathrm{T}}$ (right) for the matched particle and detector-level jets with $R = 0.6$, generated by PYTHIA and normalized to unity in slices of $p_{\mathrm{T}}^{\mathrm{part}}$and $E^{\mathrm{part}}$.

We now explore the FoCal response to fragmenting jets in pp collisions at $\sqrt{s} = 14$ TeV. Figure 39 shows the FoCal response matrices, which correlate matched particle and detector-level jets as a function of either energy $E$ or transverse momentum $p_{\mathrm{T}}$. The energy is calculated assuming zero mass of the shower-initiating particles. We study the response as a function of both kinematic variables to explore their differences, since one may then be preferred for physics analysis - for instance because its response is more linear over a broader kinematic range.

The two panels are qualitatively similar, with the weight of the distributions above the diagonal, corresponding to a lower value at detector than at particle-level of the kinematic quantity. This is expected, in light of the discussion in the foregoing sections.

Figure 40 provides more detail on the FoCal jet response, showing distributions of $\Delta E$ and $\Delta p_{\mathrm{T}}$ (Eq. 14) for selected intervals in $E^{\mathrm{part}}$ and $p_{\mathrm{T}}^{\mathrm{part}}$. The distributions are largely Gaussian, meaning that the jet response can be meaningfully characterized by two quantities, JES and JER. However, the distributions also exhibit non-Gaussian tails, indicating that precise jet measurements require correction using unfolding of the full response matrix.

Figure 41 shows the JES and JER for both energy and transverse momentum, for jets with $R = 0.6$ and with centroid $4.0 < \eta^{\mathrm{jet}} < 4.9$. The JES values are negative, as noted above. The JES distribution is slightly more uniform for $p_{\mathrm{T}} > 15$ GeV$/c$ than for $E$, though the difference is minor. The impact of this difference on final systematic uncertainties for jet analyses requires detailed study. The JER is below 15% for $p_{\mathrm{T}}^{\mathrm{jet}} > 10$ GeV$/c$ , though its specific value depends upon whether it is calculated from the Gaussian fit or by numerical integration, reflecting the contribution of the non-Gaussian tails seen in Fig. 40.

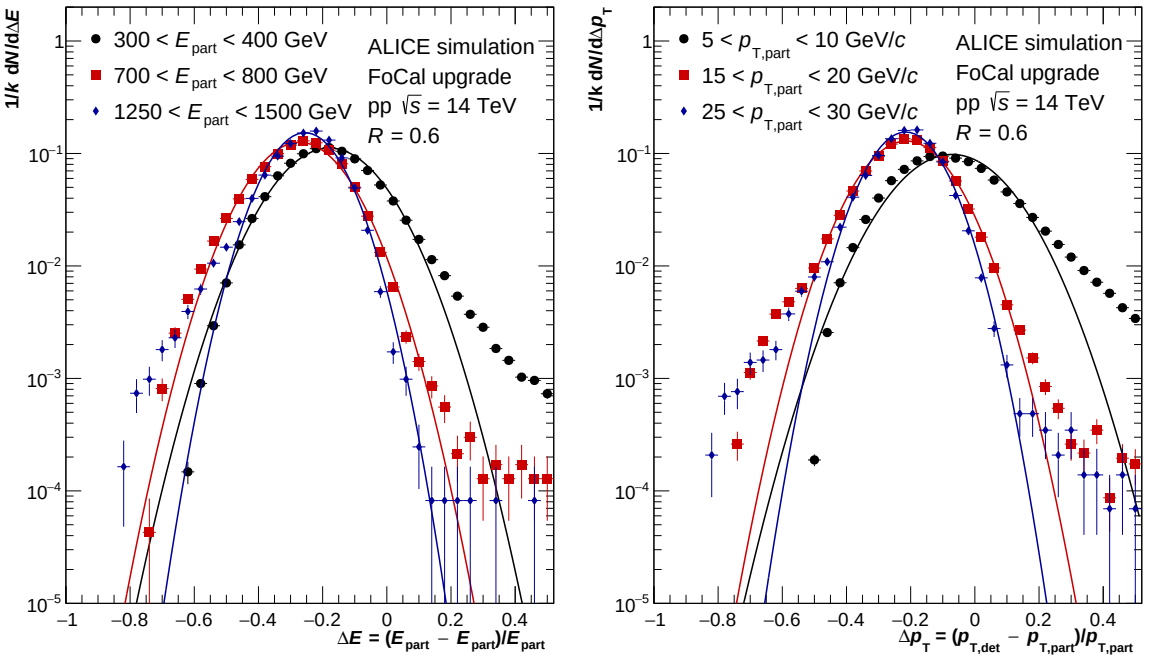


**Fig. 40:** Distributions of $\Delta E$ (left) and $\Delta p_{\mathrm{T}}$ (right) for jets with $R = 0.6$ in pp collisions at $\sqrt{s} = 14$ TeV, in selected intervals of $E^{\mathrm{part}}$ and $p_{\mathrm{T}}^{\mathrm{part}}$. A Gaussian fit is shown for each distribution.

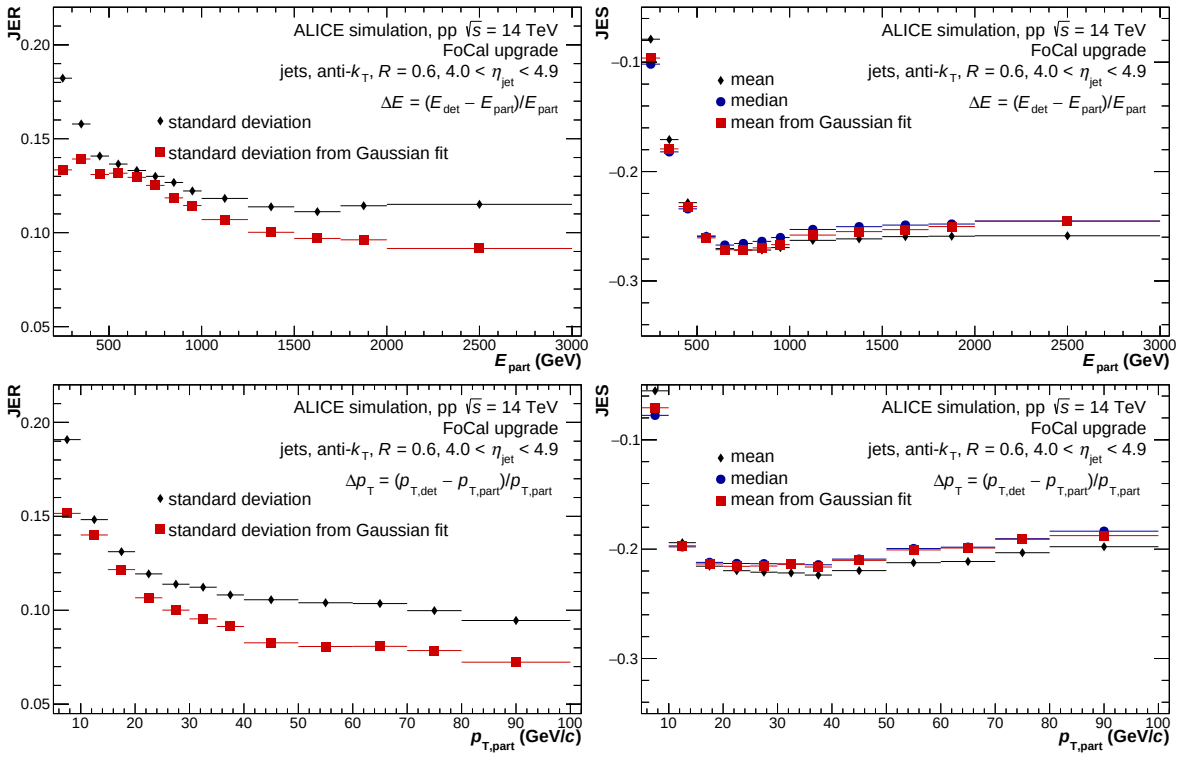


**Fig. 41:** JER (left) and JES (right) for jets with $R = 0.6$ calculated using $\Delta E$ (upper panels) and $\Delta p_{\mathrm{T}}$ (lower panels). The mean and standard deviation were calculated in two ways: numerical integral, and fitting a Gaussian function.

## 6.5 Neutral Energy Fraction

Figure 38 shows that the FoCal response to single EM showers is markedly better than its response to single hadronic showers, due to the spatially much more compact nature of FoCal EM showers and to the

geometric considerations discussed in Sec. 6.2. This raises the question whether the superior response to EM showers can be used in practice in the analysis of FoCal jet data, to improve the JES presented in the previous section.

In order to do so we focus on the distribution of Neutral Energy Fraction (NEF) at the particle and detector levels, and their correlation. At the particle level, NEF is calculated using the particle labels provided by the event generator. At the detector level, NEF is defined as the ratio of the neutral energy measured in FoCal-E to the total FoCal energy, FoCal-E + FoCal-H.

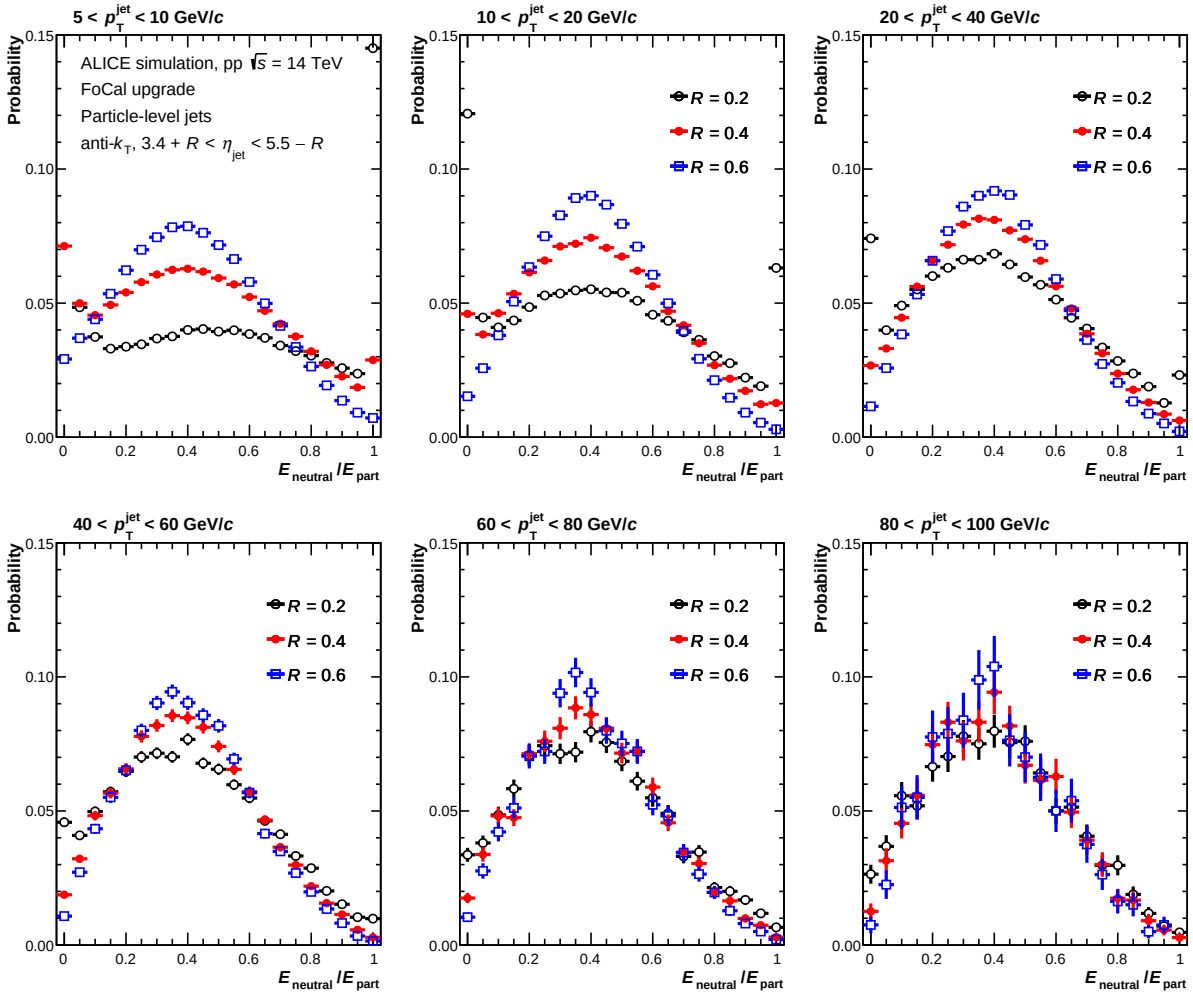


**Fig. 42:** NEF probability distribution calculated by PYTHIA at the particle-level for pp collisions at $\sqrt{s} = 14$ TeV, for jets in the FoCal acceptance with $R = 0.2, 0.4, 0.6$ in bins of $p_{\mathrm{T}}^{\mathrm{jet}}$.

Figure 42 shows NEF probability distributions for particle-level jets with $R = 0.2, 0.4, 0.6$, in bins of $p_{\mathrm{T}}^{\mathrm{jet}}$. The distributions for $R = 0.4$ and 0.6 at all $p_{\mathrm{T}}^{\mathrm{jet}}$ are peaked near 1/3, as expected from isospin symmetry. However, the distributions for $R = 0.2$ at low $p_{\mathrm{T}}^{\mathrm{jet}}$ are broad, with no distinct peak, indicating that such jets are dominated by fluctuations in fragmentation and are less well-defined. This indicates that jet reconstruction with a value for $R$ of 0.4 or larger is preferred for precise measurements in this forward region, especially at low $p_{\mathrm{T}}^{\mathrm{jet}}$. As $p_{\mathrm{T}}^{\mathrm{jet}}$ increases, the $R = 0.2$ NEF distribution approaches that for larger $R$.

Figure 43 shows the NEF distribution for particle level jets with $R$=0.6, comparing different intervals in $p_{\mathrm{T}}^{\mathrm{jet}}$. For this choice of $R$ there is no significant dependence of the NEF distribution on $p_{\mathrm{T}}^{\mathrm{jet}}$. The following figures in this section will be shown for jets with radius $R = 0.6$.

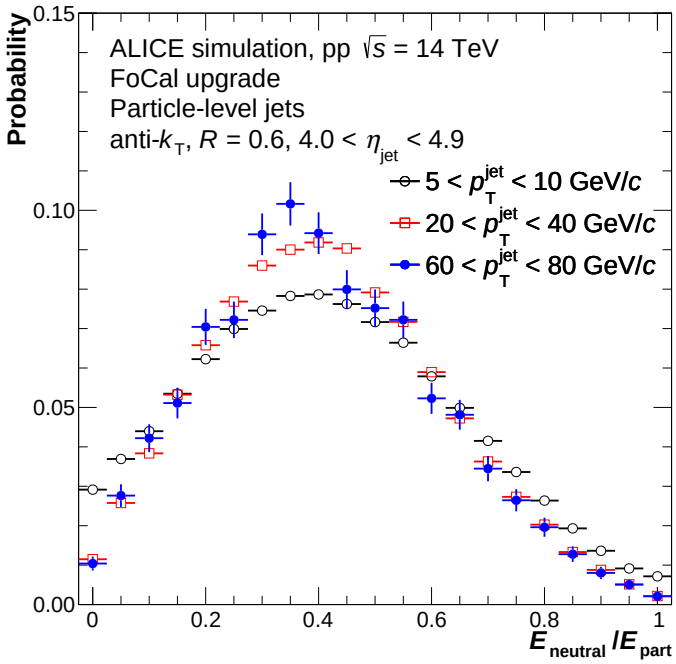


**Fig. 43:** Dependence on $p_T^{jet}$ of the NEF probability distribution calculated by PYTHIA at the particle-level for pp collisions at $\sqrt{s} = 14$ TeV, for jets in the FoCal acceptance with $R = 0.6$.

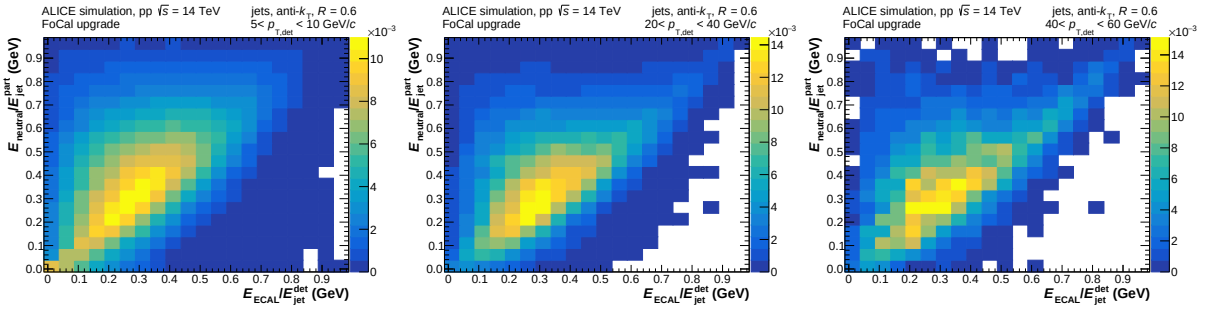


**Fig. 44:** Correlation of NEF at the particle and detector levels, for selected bins in $p_T^{det}$.

Figure 44, shows the correlation of NEF at the particle and detector levels for matched jets, in selected bins of $p_T^{det}$. The NEF distributions are highly correlated between particle and detector levels.

We now address the question whether the JES can be improved by biasing jet jet population towards a larger EM shower component, i.e. larger NEF. Experimentally, NEF can only be determined by comparing overlapping shower energy in FoCal-E and FoCal-H, i.e. at the detector level, denoted $\mathrm{NEF_{det}}$. Since pp and p–Pb events are sparse, we assume for this discussion that effects due to ambiguity in matching jet showers in the two calorimeters are negligible. However, this assumption should be revisited in future.

Figure 45 shows JES and JER based on $\Delta E$, similar to Fig. 41, but in this case with jet populations that are biased by enhanced EM shower fraction relative to the unbiased population ($\mathrm{NEF_{det}} > 2/3$), or suppressed EM shower fraction ($\mathrm{NEF_{det}} < 1/3$). The figure shows that JER is largely insensitive to this bias, whereas JES is markedly improved by enhancing the EM shower fraction.

To explore this enhancement further, Figure 46 compares NEF-biased populations at the detector and particle levels. Since the distributions of $\mathrm{NEF_{part}}$ and $\mathrm{NEF_{det}}$ are not identical, such a comparison cannot use the same numerical value of NER cut for the two populations. Rather, we order events in increasing

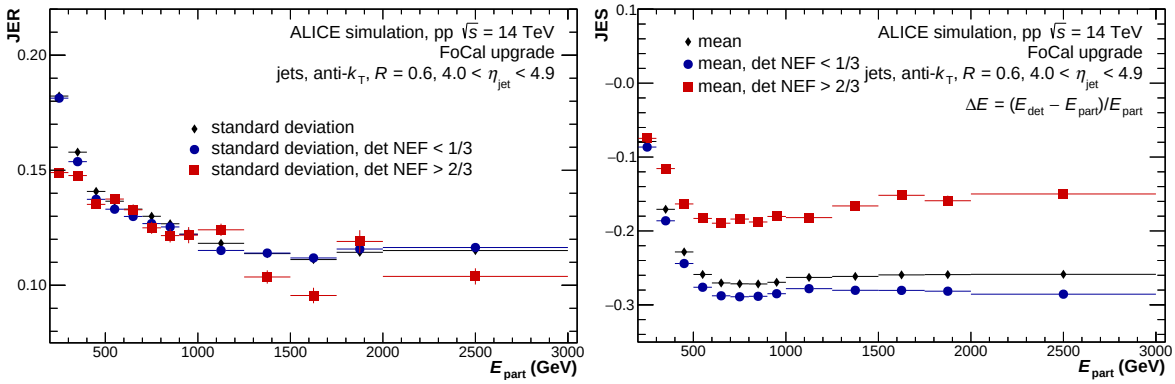


**Fig. 45:** JER (right) and JES (left) for jets (anti $-k_T$, $R = 0.6$) based on $\Delta E$, in pp collisions at $\sqrt{s} = 14$ TeV generated by PYTHIA, for different cuts on $\mathrm{NEF_{det}}$.

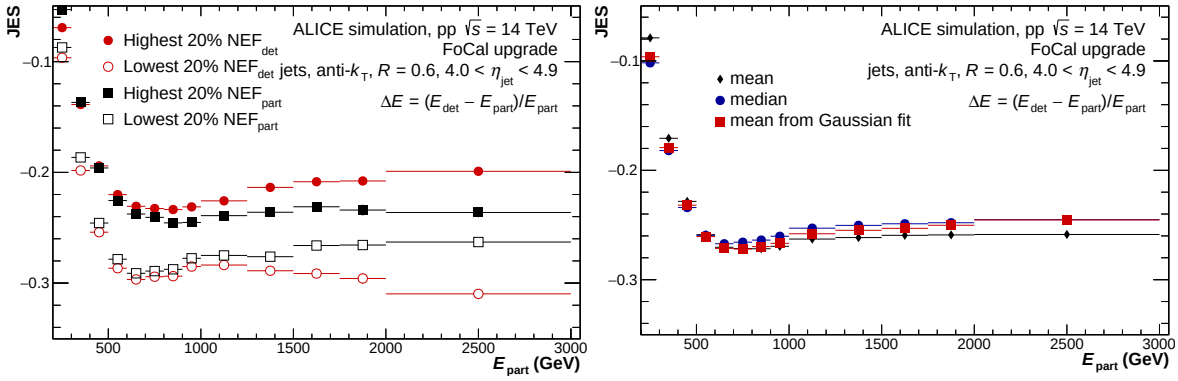


**Fig. 46:** Left: JES for jets in pp collisions with $R = 0.6$ for biased jet populations corresponding to 20% of the unbiased population with highest and lowest $\mathrm{NEF_{det}}$ or $\mathrm{NEF_{part}}$. Right: same as Fig. 41, upper left; copied here for direct comparison.

NEF and compare distributions for the same percentile bins, in this case for the 20% of the population with highest or lowest $\mathrm{NEF_{det}}$ or $\mathrm{NEF_{part}}$. The upper left panel of Figure 41, which contains the unbiased distribution for comparison, is copied here. An improvement in JES for high NEF bias is again observed; the 20% cut corresponds to $\mathrm{NEF_{part}} > 0.63$. The distributions based on cuts in $\mathrm{NEF_{part}}$ are in qualitative agreement. These studies show promise that an NEF-biased jet population with larger EM shower fraction has improved response relative to the unbiased population. However, this requires additional detailed experimental study, as well as theoretical study of factorization-breaking effects, to assess whether a jet population selected on its fragmentation pattern in this way is amenable to precise calculation.

## 7 Di-hadron correlations

Forward correlations of light-flavor di-hadrons have been studied theoretically as a probe of saturation effects in hadronic collisions [29–37]. Such correlations are experimentally robust probes of saturation, due to their large production rate and experimental simplicity relative to photon and jet measurements. Forward di-hadron correlations have been measured in d–Au and pA collisions at RHIC [38, 39].

The physics of forward di-hadron correlations at the LHC is discussed in Ref. [2]. In this section we report the performance of FoCal for forward di-hadron measurements in p–Pb and pp collisions. Here we focus specifically on $\pi^0 + \pi^0$ correlations, which can be measured precisely in FoCal-E.

The simulations for this study utilize a triggered version of PYTHIA6. For detector-level simulations, events are transported through the geometry only if the particle-level event contains a decay photon with $p_{\mathrm{T}} > 2$ GeV/$c$ , which enhances the rate of neutral pions. The version of FoCal geometry used in these simulations does not include the aluminum material between modules where the FoCal-E cooling services will be installed, but is otherwise up-to-date.

The FoCal measurement of $\pi^0$ is presented in Sec. 5. For this study, $\pi^0$ candidates used to build the correlation functions are selected to have an invariant mass in the interval $110 < m_{\gamma\gamma} < 160$ GeV/$c^2$, and $\pi^0$ $\pi^0$ pair candidates are required to have asymmetry $\alpha = (|E_1 - E_2|)/(E_1 + E_2) < 0.8$. While the asymmetry cut suppresses background, especially at high $p_{\mathrm{T}}$, it also suppresses signal. The value chosen optimizes S/B.

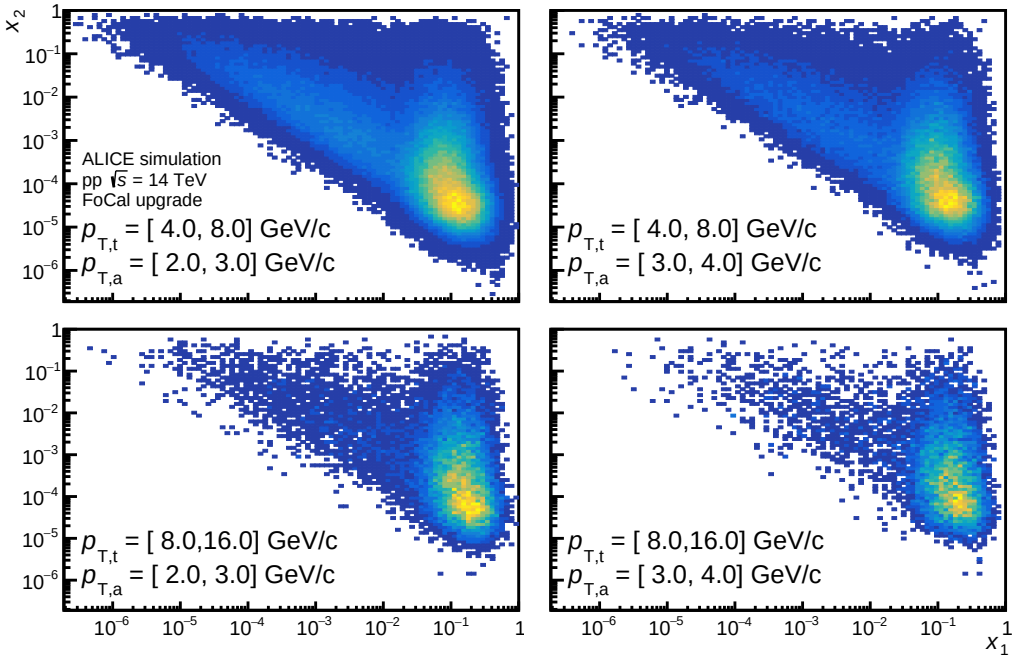


**Fig. 47:** Kinematic coverage in terms of partonic momentum fractions $x_1$ and $x_2$ of accepted generator-level $\pi^0$ pairs in pp collisions at $\sqrt{s}$=14 TeV calculated using a PYTHIA8 for various selections of trigger and associated particle $p_{\mathrm{T}}$. The values of $x_1$ and $x_2$ are determined from the hardest QCD interaction in PYTHIA8 event.

The PYTHIA event record provides momentum fractions $x_1$ and $x_2$ of the partons entering the hardest QCD interaction. Figure 47 shows the two-dimensional distribution ($x_1$,$x_2$) for pp collisions at $\sqrt{s} = 14$ TeV, in events containing $\pi^0$ pairs in the FoCal acceptance for specified trigger and associated $p_{\mathrm{T}}$ ranges, calculated using PYTHIA v8.306 [40]. The value of $x_1$ corresponds to the parton moving towards FoCal, and is typically large compared to the parton going in the opposite direction ($x_2$), to provide a large enough kick to push both final-state pions towards the FoCal. The momentum fraction $x_2$ can reach

values as low as $10^{-6}$ but peaks around $10^{-5}$–$10^{-4}$ for the lower trigger and associated particle $p_{\mathrm{T}}$.

The trigger-normalized correlation function of a $\pi^0$ trigger and $\pi^0$ associated particle is a double–differential distribution in $\Delta\varphi = (\varphi_{\mathrm{trig}} - \varphi_{\mathrm{assoc}})$ and $\Delta\eta = (\eta_{\mathrm{trig}} - \eta_{\mathrm{assoc}})$,

$$S(\Delta\varphi, \Delta\eta) = \frac{1}{N_{\mathrm{trig}}} \frac{\mathrm{d}^2 N_{\mathrm{assoc}}}{\mathrm{d}\Delta\varphi \mathrm{d}\Delta\eta}, \tag{16}$$

where $N_{\mathrm{trig}}$ and $N_{\mathrm{assoc}}$ are the numbers of trigger and associated $\pi^0$ in the same event. Finite acceptance and detector inefficiencies can be corrected using event mixing,

$$f(\Delta\varphi, \Delta\eta) = \frac{S(\Delta\varphi, \Delta\eta)}{B(\Delta\varphi, \Delta\eta)}, \tag{17}$$

where the mixed-event distribution $B(\Delta\varphi, \Delta\eta)$ is constructed in the same way as $S(\Delta\varphi, \Delta\eta)$ but with trigger and associated particles taken from different events. The mixed event distribution is normalized such that $B(0,0) = 1$, since collinear pairs are not affected by the finite acceptance. For high-$p_{\mathrm{T}}$ azimuthal correlations with limited statistics and limited acceptance, the dependence of $S(\Delta\varphi, \Delta\eta)$ on $\Delta\eta$ is sometimes projected away (e.g. [41]). In this section we present azimuthal $\pi^0$–$\pi^0$ correlations without mixed-event correction, i.e. the $\Delta\eta$ projection of $S(\Delta\varphi, \Delta\eta)$. We have checked that the mixed-event distribution does not contain significant structure in $\Delta\varphi$.

Figure 28 shows the invariant mass distribution of photon pairs in simulated pp collisions at $\sqrt{s} = 14$ TeV which have at least one $\pi^0$ in the FoCal acceptance. The figure shows that $\pi^0$ candidates used as trigger and associated particles in a correlation function can arise not only from signal, i.e. photon pairs from decay of the same $\pi^0$, but also from correlated and uncorrelated background sources. The uncorrelated background pairs are combinatorial, while the correlated background can originate from cluster splitting (see Sec. 2.3).

A correlation function constructed from two $\pi^0$ candidates has additional background components which are of physical origin. Correlations among inclusive photons show a two-peak structure, arising from resonances which have photons in their decay chain and which themselves have jet-like correlations. Correlations between purely combinatorial candidates in the $\pi^0$ mass range, reconstructed from clusters which do not originate from a single $\pi^0$, therefore exhibit similar features to true jet-like azimuthal correlations. These background contributions must be corrected for a precise $\pi^0$ correlation measurement.

The measured two-$\pi^0$ correlation function can be modelled as the sum of four components,

$$f_{\pi^0,\pi^0} = f_{\mathrm{true,true}} + f_{\mathrm{true,fake}} + f_{\mathrm{fake,true}} + f_{\mathrm{fake,fake}}, \tag{18}$$

where the first element in the subscript refers to the trigger and the second to the associated particle, "true" is a $\pi^0$ candidate constructed from the decay products of a single $\pi^0$, and "fake" is a candidate that is not a true $\pi^0$.

While the different components of the correlation function cannot be measured directly, because $\pi^0$ candidates cannot be unambiguously separated from the background on an event-by-event basis, their magnitude can be estimated statistically using the yield in the signal and side-mass bands. The sidebands are the regions in the invariant mass distribution adjacent to the mass peak that contain mainly background pairs (Sec. 5). Correlation functions are then constructed using $\pi^0$ candidates drawn from

either the signal region ($\pi^0$ mass window) or from a sideband. There are four classes of correlation functions that can be constructed in this way, containing different contributions of the components defined in Eq. 18:

$$f_{\text{mass,mass}} = f_{\text{true,true}} + f_{\text{true,fake}} + f_{\text{fake,true}} + f_{\text{fake,fake}} \tag{19a}$$
$$f_{\text{mass,side}} = f_{\text{true,fake}} + f_{\text{fake,fake}} \tag{19b}$$
$$f_{\text{side,mass}} = f_{\text{fake,true}} + f_{\text{fake,fake}} \tag{19c}$$
$$f_{\text{side,side}} = f_{\text{fake,fake}}. \tag{19d}$$

The goal of the analysis is to measure $f_{\text{true,true}}$. Eq. (19a) corresponds to the measured correlation function defined in Eq. 18, which, in addition to the signal component, also contains contributions from fake $\pi^0$ candidates. The fake $\pi^0$ component yield can be estimated using the Equations 19b, 19c and 19d.

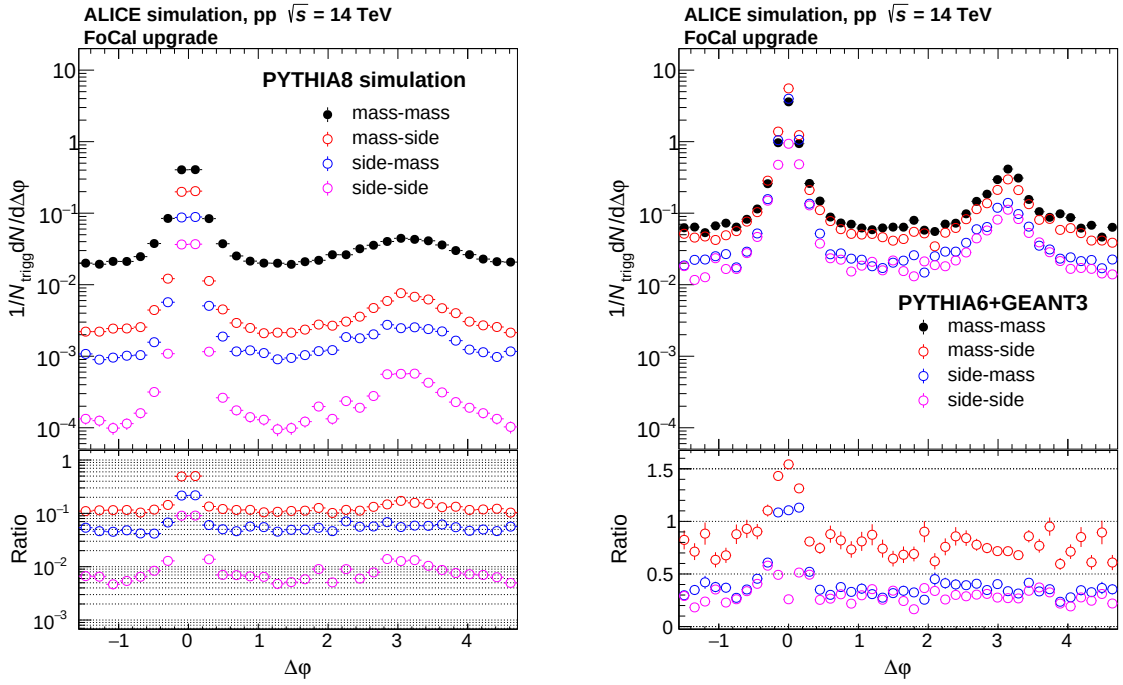


**Fig. 48:** Components of the $\pi^0$-$\pi^0$ correlation function (Eq. 19a-19d) in the FoCal acceptance for pp collisions at $\sqrt{s}$=14 TeV simulated by PYTHIA8 at particle level (left), and PYTHIA6 at detector level (right).

Side-band pairs are used to measure fake correlation components defined in Eqs. 19b, 19c, and 19d. By counting the number of pairs, the true-true component can be expressed as

$$f_{\text{true,true}} = f_{\text{mass,mass}} - \alpha f_{\text{mass,side}} - \beta f_{\text{side,mass}} + \alpha\beta f_{\text{side,side}}, \tag{20}$$

where scaling factors $\alpha$ and $\beta$ account for the normalization of the background components. Assuming that the measured "mass,mass" correlation functions are a linear superposition of the signal and background correlation functions, the scaling factors can be obtained from the fraction candidates in mass and sideband regions of the $\pi^0$ mass peak for trigger and associated particles. The right-hand side of Eq. 20 only contains measurable quantities.

Figure 48 shows the components of Eq. 20 at particle and detector level. All components, including side-side, show jet-like peak structures, indicating the non-trivial combinatorial background correlations

discussed above. The lower panels show the ratio of the purely combinatorial components to the mass-mass contribution, i.e. the measured raw correlation between the candidates. At the particle level the components are clearly separated, while at the detector level their magnitudes are similar. This makes the determination of the true-true component demanding in terms of statistics, because it corresponds to the difference of two distributions of similar magnitude (see Fig. 50).

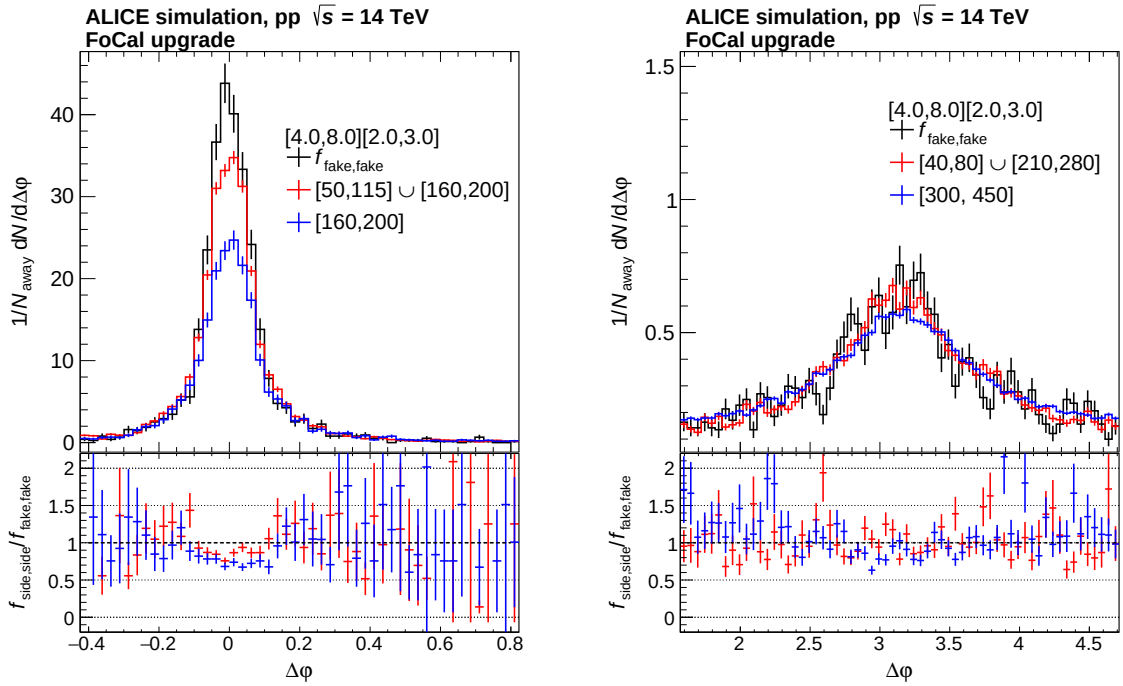


**Fig. 49:** Comparison between the reconstructed sideband correlation $f_{\text{side,side}}$ and the true (from MC matching) background correlation for the measured function ($f_{\text{fake,fake}}$). The near side (left) and away side (right) are shown for the case of two different sideband selections. The ratios on the lower panel correspond to the colors on the upper panel.

Since the side-side component in Eq. 19d should contain only fake-fake contributions, this provides an opportunity to test the validity of this side-band subtraction method, specifically the assumption that non-physical correlations under the mass peak are similar to the correlations in the side-band. Using PYTHIA we can choose combinatorial fake candidates under the mass peak and construct the exact $f_{\text{fake,fake}}$ correlation that is not accessible experimentally. Figure 49 shows the comparison between $f_{\text{fake,fake}}$ and the measured $f_{\text{side,side}}$ for near-side and away-side correlation functions, for various choices of side-band mass range. The side-side correlations are constructed using the $[50,115] \cup [160,200]$ and $[160,200]$ MeV$/c^2$ in the near-side and $[40,80] \cup [210,280]$ and $[300,450]$ MeV$/c^2$ in the away-side. The distributions are normalized such that they have the same integral as the fake-fake component on the away-side.

The figure shows that the shape of the away-side correlation is not sensitive to selection of the mass range in the side-band, which describes the shape of the correlations well. However, the near-side correlation is more sensitive to the selection of the side-band mass window; closer to the peak is preferred. Nevertheless, the shape of the fake-fake correlation on the near-side is as well-reproduced. This is primarily due to the fact that, on the near side, trigger and associated $\pi^0$ candidates overlap spatially in the calorimeter, leading both to fake pairs and to reconstruction inefficiencies due to shower overlap, which affects both $\pi^0$ candidates. At the current stage of the analysis, correction of the near-side correlation function is therefore less reliable, particularly since in the full simulation the $\pi^0$ peaks are fairly wide, and selection of a side-band close to the peak is not possible. In the following we focus on the performance of the

away-side correlation measurement.

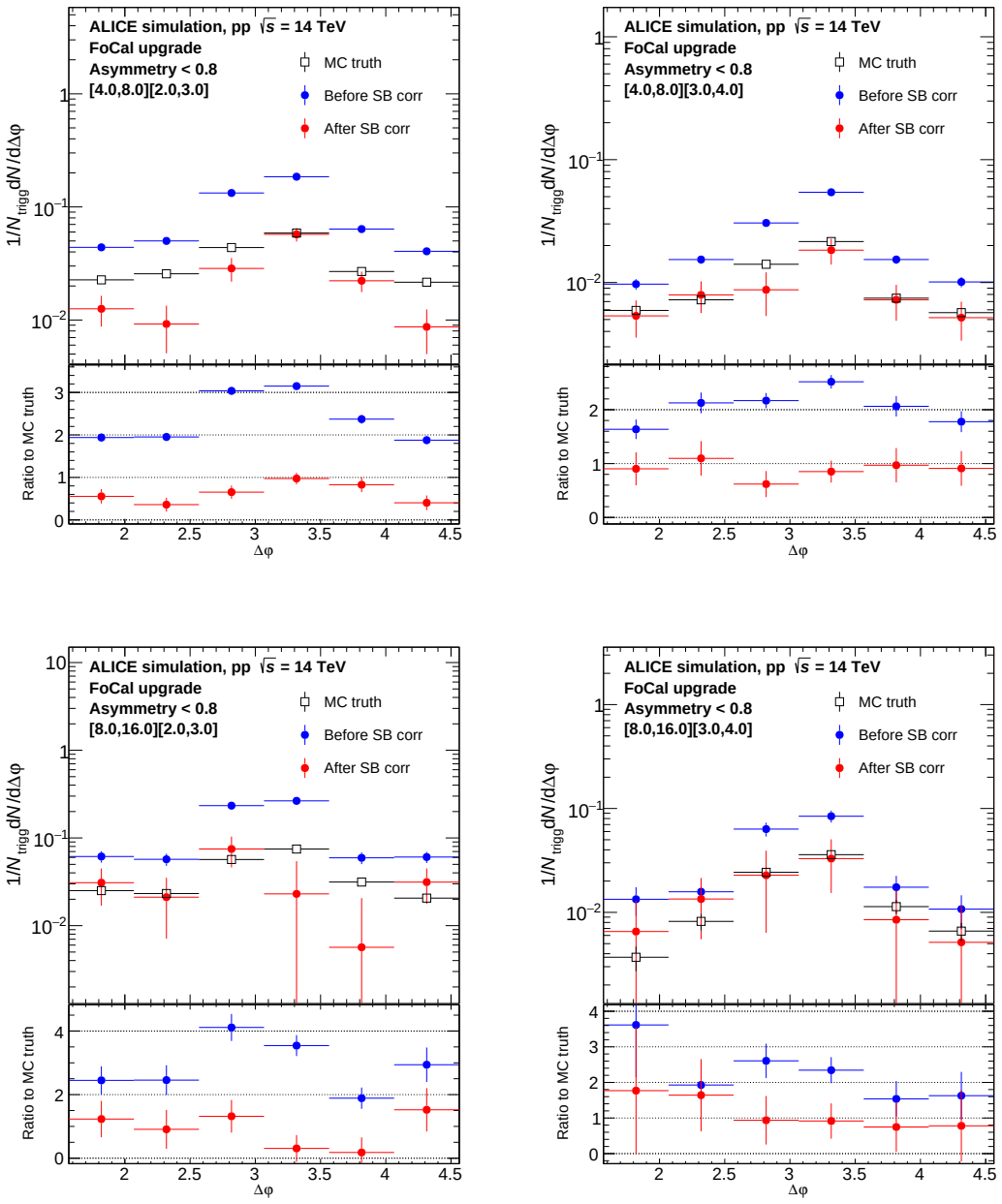


**Fig. 50:** The away side of $\pi^0$–$\pi^0$ correlation in four different $p_{\mathrm{T}}$ bins, calculated from clusters reconstructed in FoCal-E. Statistical errors and jitter of central values reflect the limited statistics of the simulated sample, and not the values of $\mathscr{L}_{\mathrm{int}}$ projected for LHC Run 4.

Figure 50 shows the away-side correlation before and after side-band subtraction, in four kinematic intervals. The associated particles are weighted with the inverse of their rapidity and $p_{\mathrm{T}}$-dependent reconstruction efficiency, as detailed in Sec. 5. In order to increase the size of the $\pi^0$ sample, the candidates are taken from the mass range $m_{\gamma\gamma} = [50, 200]$ MeV$/c^2$. The side-band is taken only from the higher mass region, in window $m_{\gamma\gamma} = [250, 450]$ MeV$/c^2$, to avoid the low mass region which includes a large contribution of pairs from split clusters.

The panels in Figure 50 also show the correlation function for true MC $\pi^0$ pairs ($f_{\mathrm{true,true}}$), compared

to the reconstructed correlation function before (blue) and after (red) the side-band subtraction. The reconstructed correlation functions are in agreement with the generator level correlations except for $[4.0, 8.0][2.0, 3.0]$, which exhibits deviations from the MC-truth correlation function. The error bars are statistical, and are due to the statistical precision of the simulated sample. As discussed above, the side-band subtraction at detector level corresponds to a small difference between two distributions of similar magnitude, so that the raw correlation function (blue markers, before side-band) has significantly smaller statistical error than the final side-band corrected result (red markers). Statistical uncertainties for the cases presented here are expected to be negligible for projected Run 4 $\mathscr{L}_{\text{int}} = 100$ pb$^{-1}$ for pp collisions, and only systematic effects will be important.

## 8 Photon-hadron correlations

The physics of forward direct photon-hadron ($\gamma_{\rm dir}$–h) correlations as a probe of non-linear QCD evolution is discussed in Ref. [2]. Saturation effects are expected to modify the shape of the azimuthal distribution of $\gamma_{\rm dir}$–h correlations, and a key performance metric for the FoCal in this channel is the precision with which the width of such correlation functions can be measured in practice. This section provides a first estimate of that precision.

Section 4 presents the FoCal approach to measuring isolated photons ($\gamma_{\rm iso}$). The isolated photon population contains between 20% and 70% $\gamma_{\rm dir}$, depending on $p_{\rm T}$, which are identified using invariant mass and shower shape cuts. The measurement of $\gamma_{\rm dir}$–$\pi^0$ correlations can be determined from $\gamma_{\rm iso}$–$\pi^0$ correlations, by using additional procedures to suppress the non-$\gamma_{\rm dir}$–$\pi^0$ correlation component.

We first present an estimate of FoCal capabilities to measure the "raw" $\gamma_{\rm iso}$–$\pi^0$ correlations. Various strategies are then available to determine the the $\gamma_{\rm dir}$–$\pi^0$ correlation from this raw distribution. In a recent ALICE analysis of $\gamma_{\rm dir}$–hadron correlations in central barrel [42], a purity-weighted background template was subtracted from the raw correlation function. This method is not applicable here, however, because the associated $\pi^0$ is reconstructed from decay products, and $\pi^0$ candidates contain both true and combinatorial pairs. In section we illustrate an alternative approach, which transforms the experimentally measurable $\gamma_{\rm iso}$–$\pi^0$ candidate correlation to obtain the $\gamma_{\rm dir}$–$\pi^0$ correlation using iterative Bayesian unfolding.

Direct photon – $\pi^0$ correlations for pp collisions at $\sqrt{s}$=14 TeV were simulated using PYTHIA6.4 [8]. Signal and background are generated by PYTHIA, with separate simulation samples triggered on direct photon and jet-jet processes. Events from these samples are summed using a weighting procedure, taking into account the hard scattering cross section for these processes given by PYTHIA. These particle-level events are transported by GEANT through the detector model, and $\gamma_{\rm iso}$ and $\pi^0$ candidates are reconstructed using the same experimental cuts as in Sec. 4 and Sec. 5.

Matching of true photons at the particle level and clusters at the detector level is based on their proximity in $(\eta, \varphi)$ phase space (Sec. 2.4). The filled area in Figure 51 shows the distribution of true MC matched isolated photons. Solid lines are distributions of the number of clusters surviving successive selection criteria: cluster energy threshold $> 50$ GeV, isolation energy $E_{\rm T,iso}^{\rm H+E} < 2\,$GeV, invariant mass tagging, and shower shape. The dashed lines show the number distribution of clusters matched to isolated photons and decay photons from $\pi^0$.

The purity and efficiency and determined from these distributions and are shown in the lower panel. The purity is the ratio of the number of isolated clusters matched to true photons to the total number of isolated clusters. The purity has values in the range 30-60% for $p_{\rm T} > 10$ GeV/$c$ . Correlation measurements for $p_{\rm T} < 10$ GeV/$c$ require further optimization, in order to achieve the required purity while maintaining sufficient efficiency.

### 8.1 Measurement of raw correlation function and projection to full luminosity

The selection of isolated photon and $\pi^0$ candidates uses identical cluster cuts as are used in Sec. 4, 5, and 7, which are not duplicated here. In the correlation analysis, it is essential that the cuts optimize the purity of the isolated clusters. Clusters satisfying $3.5 < \eta < 5.2$ and $p_{\rm T,clust} > 5$ GeV/$c$ are checked for isolation. When an isolated cluster is found, all other clusters in that event with $E_{\rm clus} > 2$ GeV are used to construct $\pi^0$ candidates as follows:

- Calculate the invariant mass for all such cluster pairs;
- Reject pairs that are outside the $\pi^0$ mass window or do not pass shower shape and energy asymmetry cuts;
- Among the remaining cluster pairs, the pair whose invariant mass is closest to the nominal $\pi^0$ mass

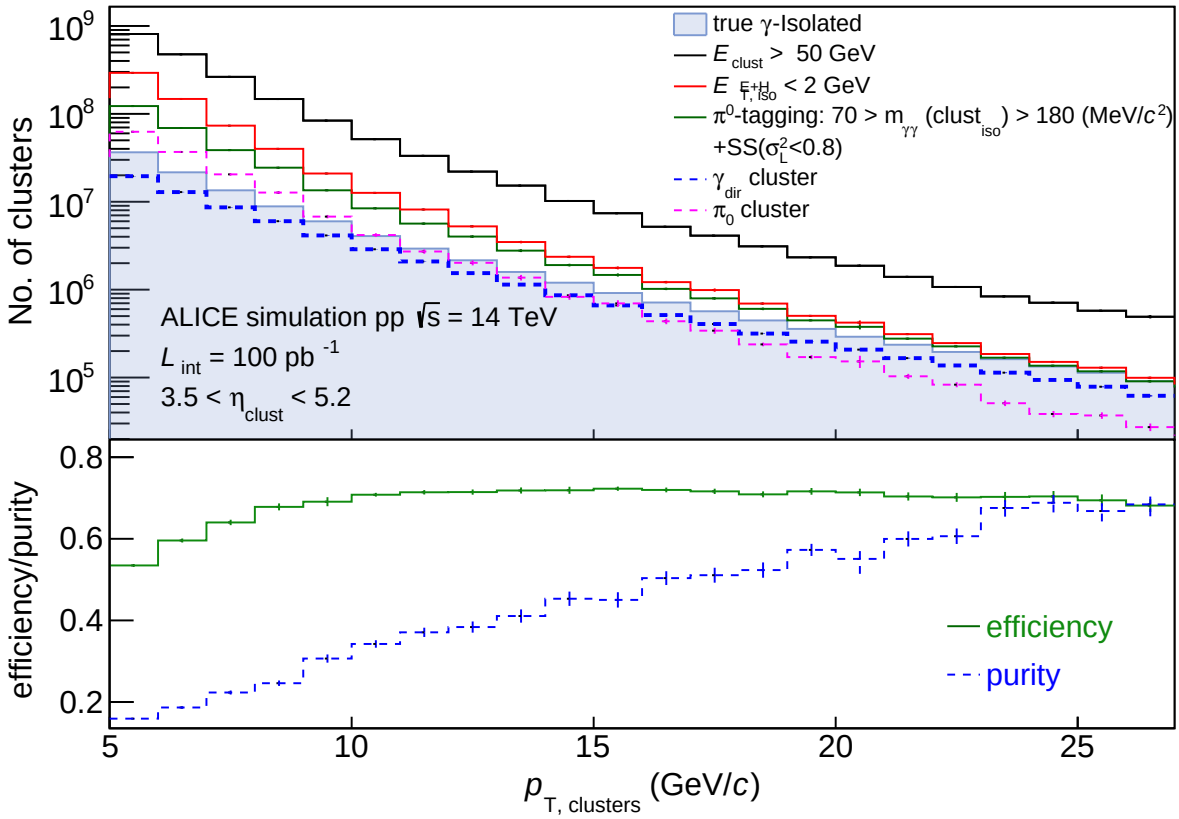


**Fig. 51:** Top: Number of isolated photons or clusters at different analysis stages, as a function of $p_{\mathrm{T}}$, see text for the details. Bottom: Efficiency and purity as a function of $p_{\mathrm{T}}$.

is assigned as a reconstructed $\pi^0$, and this cluster pair is removed from the cluster pool;

– The procedure is repeated until no $\pi^0$ candidates are found in the $\pi^0$ mass window in the event.

Figure 52, red markers, show the raw isolated cluster – $\pi^0$ candidate correlation generated by PYTHIA at the detector level, for pp collisions at $\sqrt{s} = 14$ TeV. In contrast to dihadron correlations (Sec. 7), there is no near-side correlation peak, but rather a small dip, at $\Delta\varphi = 0$ that results from the isolation cut. The statistical error of the red points is that of the simulated dataset.

In order to estimate the statistical precision of this measurement for the projected Run 4 integrated luminosity, $\mathscr{L}_{\mathrm{int}} = 100$ pb$^{-1}$, this distribution is fit with a function consisting of a Gaussian distribution plus a constant,

$$f(\Delta\varphi) = c + \frac{1}{\sigma\sqrt{2\pi}} e^{-(\Delta\varphi-\mu)^2/2\sigma^2} \tag{21}$$

which is used to generate a pseudo–data distribution with the projected statistical erro. First, the number of triggers in a given bin is scaled to correspond that expected for integrated luminosity for pp in Run-4 of 100 pb$^{-1}$. The number of sampled pairs is then estimated, such that the ratio of the isolated trigger clusters and associated $\pi^0$ candidates is the same between the pseudo–data and simulation in every trigger and associated $p_{\mathrm{T}}$ bin.

The black markers in Figure 52 show the pseudo–data for the raw correlation function with statistical error corresponding to $\mathscr{L}_{\mathrm{int}}$=100 pb$^{-1}$. Since the fit does not incorporate a dip structure at $\Delta\varphi = 0$, this structure is not present in the extrapolated distribution; in any case it is not of physical interest.

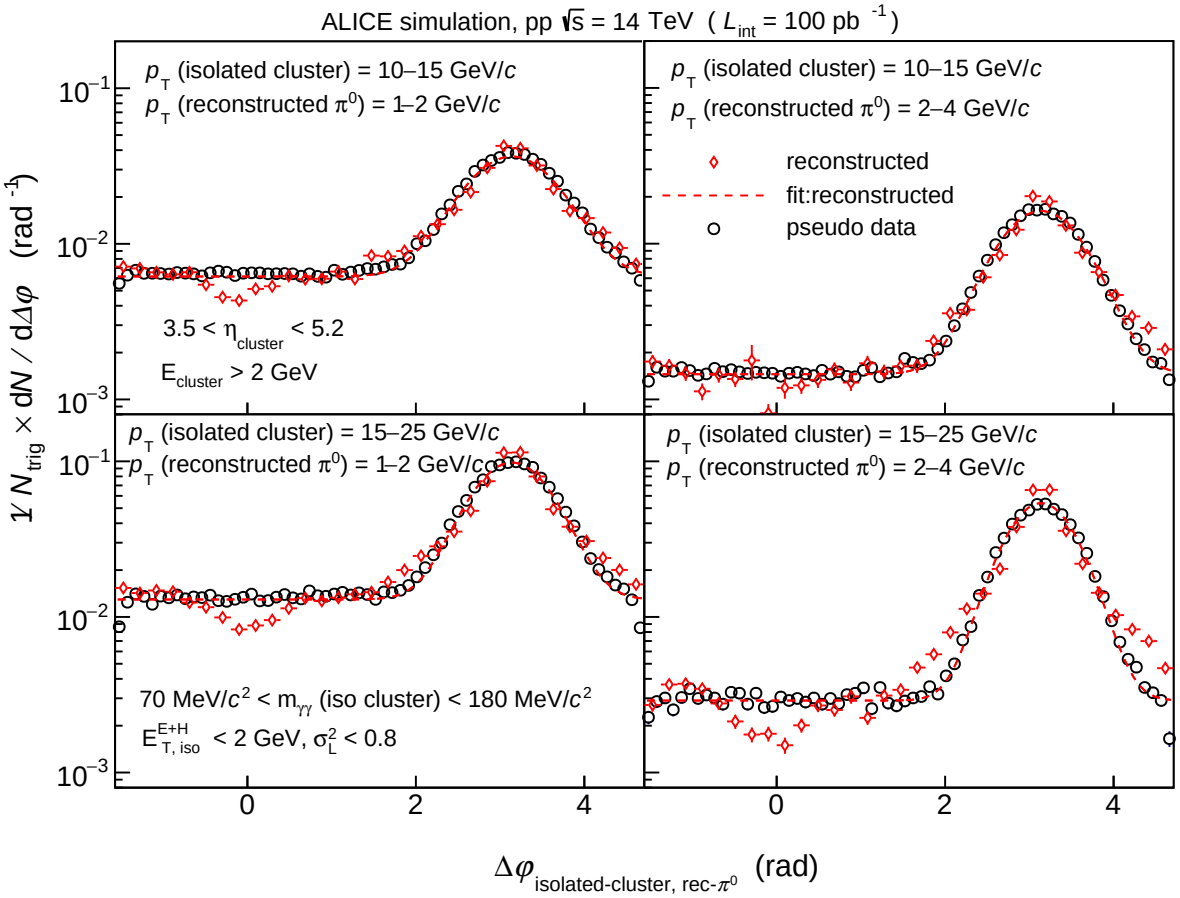


**Fig. 52:** Azimuthal distribution of isolated cluster–$\pi^0$ correlation functions in the FoCal acceptance in pp collisions at $\sqrt{s} = 14$ TeV, simulated by PYTHIA. Red markers show the correlation functions calculated by PYTHIA for selected bins in $p_{\mathrm{T}}^{\mathrm{trig}}$ and $p_{\mathrm{T}}^{\mathrm{assoc}}$. Uncertainties are those of the simulated data-set. Black markers show pseudo–data wiyth uncertainties corresponding to integrated luminosity $\mathscr{L}_{\mathrm{int}} = 100$ pb$^{-1}$, whose shape is obtained from a fit to the simulated data.

The shape of the fit function does not describe the simulation well in the highest trigger and associated bin (lower-right panel) which results significant deviation between simulation and pseudo–data in this bin.

The pseudo–data are then refit using Eq. 21. Figure 53, upper panel, shows the width and its uncertainty from this fit, in selected trigger and associated $p_{\mathrm{T}}$ bins. The distributions are narrower in azimuth for larger trigger and associated $p_{\mathrm{T}}$, reflecting the expected collimation of the recoil jet peak. The lower panel shows the relative statistical error, which is 1% or smaller for all choices of kinematics considered here.

The colored bands show the uncertainty of the width extracted from the fit for $\mathscr{L}_{\mathrm{int}} = 1$, 10, and 100 pb$^{-1}$. As noted in Sec. 1, the FoCal scientific program includes several collision systems with a range of project $\mathscr{L}_{\mathrm{int}}$. The case explored in this study, pp collisions at $\sqrt{s} = 14$, has both the largest production cross section for hard processes and the highest $\mathscr{L}_{\mathrm{int}}$ compared to the other systems, and its projections therefore have the highest statistical precision; consideration of lower $\mathscr{L}_{\mathrm{int}}$ values in Figure 53 indicate the precision achievable by the other collision systems. The bands in Figure 53, lower panel, provide estimates of the sensitivity of this measurement to modifications in the $\gamma_{\mathrm{dir}}$–$\pi^0$ azimuthal distribution due to saturation effects.

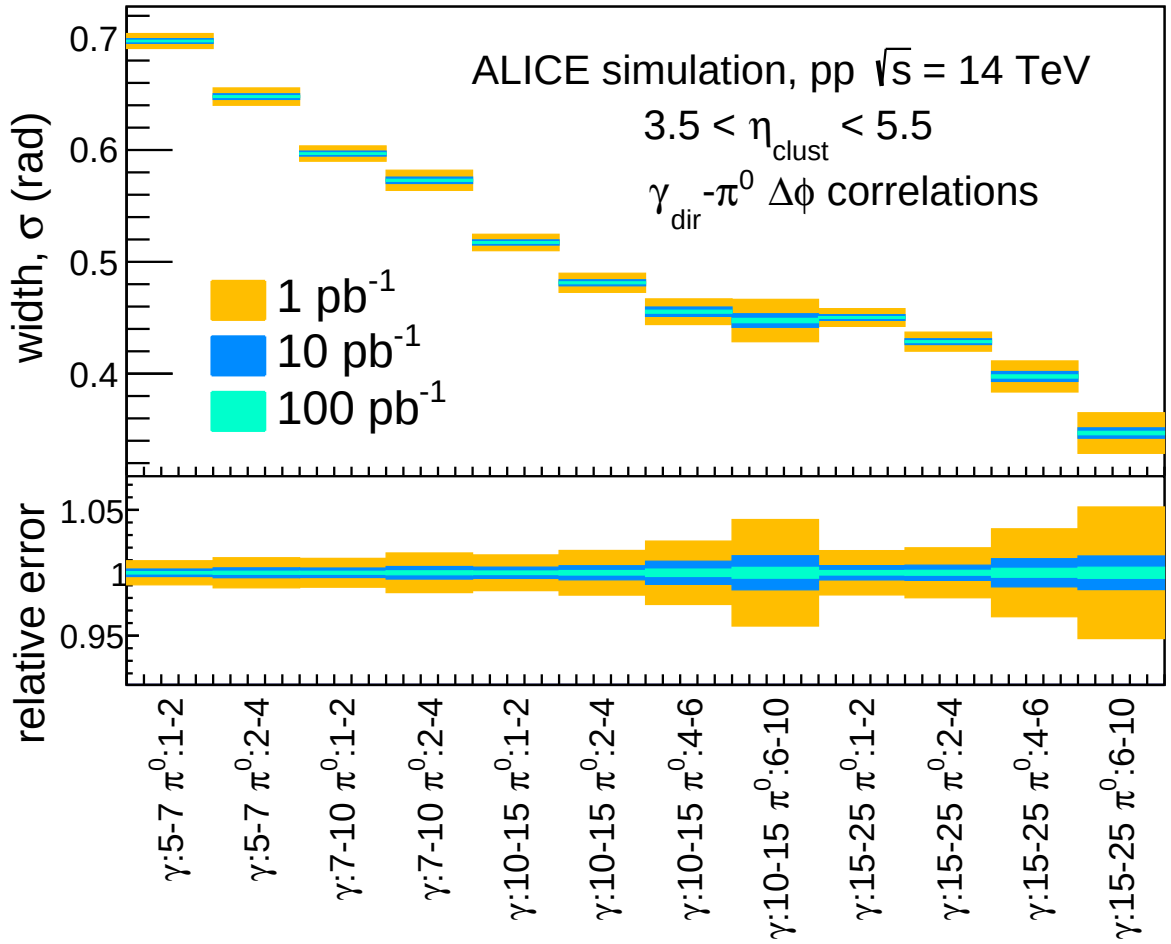


**Fig. 53:** Upper panel: width $\sigma$ and its uncertainty from a fit to $\gamma_{\rm iso}$–$\pi^0$ correlation functions in pp collisions at $\sqrt{s} = 14$ TeV for selected trigger and associated $p_{\rm T}$, from pseudo–data with statistical error corresponding to $\mathscr{L}_{\rm int} = 100$ pb$^{-1}$. Lower panel: relative error. See text for details.

### 8.2 Extraction of direct photon-$\pi^0$ correlations

The physical quantity of greatest interest in this area is the $\gamma_{\rm dir}$–$\pi^0$ correlation function. However, the measured $\gamma_{\rm iso}$–$\pi^0$ correlation function discussed in the previous section contains additional contributions from fragmentation photon and from $\pi^0$ triggers. For the inclusive $\gamma_{\rm dir}$ measurement such contributions can be suppressed directly using shower shape and invariant mass tagging, as described in Sec. 4. However, correlation observables are more complex, and additional techniques must be developed to discriminate the $\gamma_{\rm dir}$–$\pi^0$ correlation of interest from background processes. In this note we present an initial study for such discrimination based on iterative Bayesian unfolding, as implemented in the RooUnfold package [43].

Figure 54 shows the raw correlation function in $10 < p_{\rm T}^{\rm trig} < 15$ GeV/$c$ and $1 < p_{\rm T}^{\rm assoc} < 2$ GeV/$c$ (black open squares), also shown in Fig. 52, and which we label "detector level." The Monte Carlo truth is the $\gamma_{\rm dir}$– true $\pi^0$ correlation calculated by PYTHIA ("particle–level," blue open circles). Note that the particle-level distribution does not have a dip at $\Delta\varphi = 0$, because does not incorporate an isolation cut. The difference in overall normalization of the results originate mainly from finite $\pi^0$ reconstruction efficiency.

A response matrix is also calculated, representing the transformation between particle and detector-level distributions. Figure 54, red open triangles, shows the result of unfolding the raw correlation function

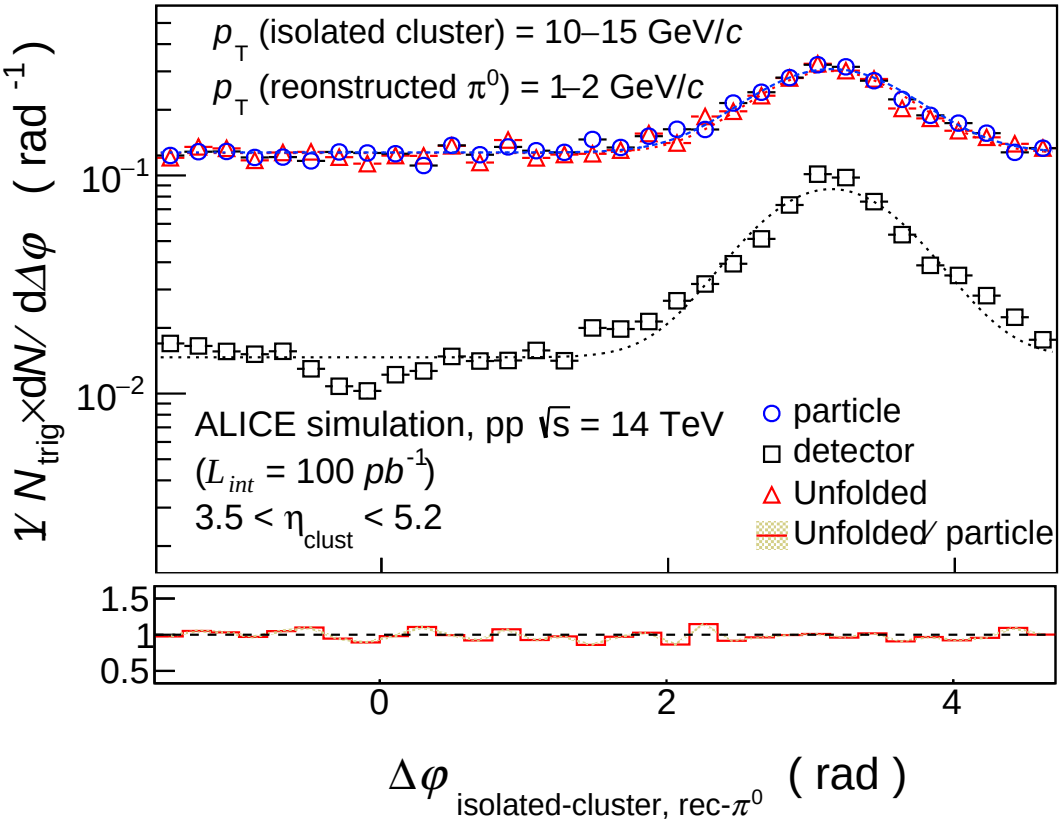


**Fig. 54:** Unfolding of measured isolated cluster triggered correlation function into true direct photon triggered correlations using iterative Bayesian unfolding in pp collisions at $\sqrt{s}$=14 TeV. The ratio between unfolded result and Monte Carlo truth demonstrates successful closure of the unfolding. See text for details.

from a sample of detector-level events that is statistically independent from the detector-level input. Good convergence of the unfolding is obtained after three iterations.

This study demonstrates closure of the unfolding process, which as such is the expected outcome. The application of this approach to data analysis requires detailed assessment of the systematic effects and uncertainties of unfolding. In particular, transformation between the correlation function of $\gamma_{\text{iso}}$–$\pi^0$ at the detector level and $\gamma_{\text{dir}}$–$\pi^0$ at the particle level may have a strong dependence on MC modeling. Other, more data-driven approaches should also be explored.

## 9 Vector meson photoproduction in ultra-peripheral collisions

The study of photoproduction in ultra-peripheral collisions (UPC) is one of the topics highlighted in the FoCal science note [2] and which is expected to significantly extend the kinematic reach of the current ALICE measurements and also complement the program foreseen at the Electron Ion Collider [44]. Since at least at the leading order in pQCD, the photoproduction cross sections of heavy vector mesons are proportional to the gluon density in the target nucleon or nucleus, these can be used to constrain the PDFs or observe eventual non-linear behaviour in gluon densities. In UPC, the target and projectile have an impact parameter larger than the sum of their radii, which strongly suppresses strong interactions. The interaction is purely electromagnetic, with the projectile emitting a photon that fluctuates into a quark dipole which then interacts with the gluon field of the target. Since in this interaction there is no net colour flow, the result is a vector meson in an otherwise empty event. When the target is a nucleus, the vector meson production can be accompanied by the emission of one or more soft neutrons, while if the target is a proton, the proton can dissociate. Both the soft neutrons and the proton dissociation products can be measured in the far forward direction, typically with Zero Degree Calorimeters. The FoCal detector provides a unique kinematic coverage, contributing to several key measurements, such as: extending the measurement of the $J/\psi$ and $\psi(2S)$ photo-production cross section off protons in p–Pb collisions up to about $W_{\gamma p} = 2$ TeV in both dissociative and exclusive events; extending the rapidity coverage of $J/\psi$ coherent photoproduction in Pb–Pb collisions up to about 5.5; and covering the very low $W_{\gamma p}$ energy range down to about 10 GeV which overlaps with the results from fixed target experiments such as E401, E516 and E687. Projections for all of these topics and their impact on the search for gluon saturation are discussed in Ref. [45] together with the expected number of vector mesons ($\rho^0$, $\phi$, $J/\psi$, $\psi$(2S), $\Upsilon$) to be produced in p–Pb and Pb–Pb collisions in the FoCal acceptance with the expected integrated luminosity in Run 4.

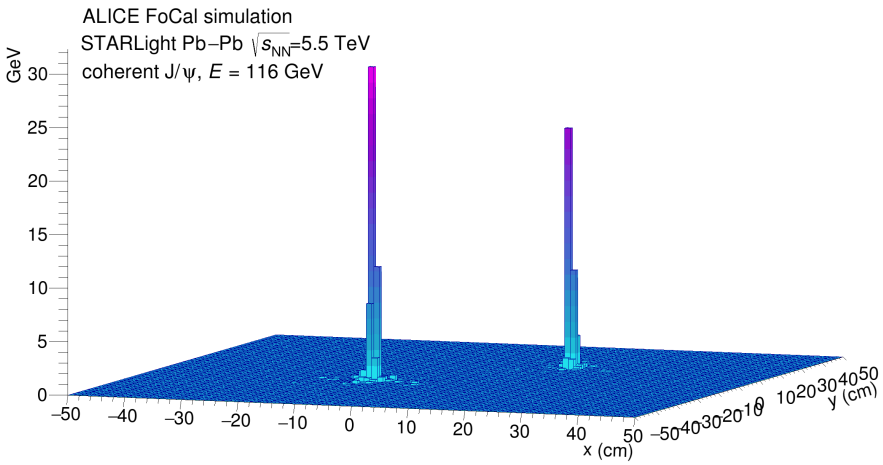


**Fig. 55:** Event display of an ultra-peripheral Pb–Pb collision at $\sqrt{s} = 5.5$ TeV simulated using the coherent $J/\psi$ photoproduction process in StarLight. The two dimensional distribution represents calibrated cell energy obtained after summing the cell energy in all the pad layers. The simulated $J/\psi$ has a total energy of 116 GeV, and decayed into a pair of electrons each having an energy of roughly 68 and 47 GeV.

The production of a very small number of primary particles in pp, p–Pb, and Pb–Pb UPC makes the measurements of electromagnetically decaying vector mesons particularly suitable for FoCal. In the following, the reconstruction performance for the photoproduced charmonium states $J/\psi$ and $\psi(2S)$, decaying into the dielectron channel, is presented. Their production and decay to dielectrons is simulated using the STARlight model [46], followed by the transport through the detector setup which is performed using GEANT3. An event display of a simulated coherent $J/\psi$ event is shown in Figure 55 as the $(x,y)$

distribution of the calibrated cell energy obtained by summing the cell energy in all the FoCal pad layers. The distribution exhibits two very distinct peaks separated by about 40 cm, with no other significant activity around. The large separation between the two showers is typical to photoproduction events due to the very low transverse momentum of the produced quarkonia ($\approx 50$ MeV in coherent and $\approx 500$ MeV in incoherent events) and the relatively large decay energy of heavy quarkonia to dielectrons. The $p_{\mathrm{T}}$ and

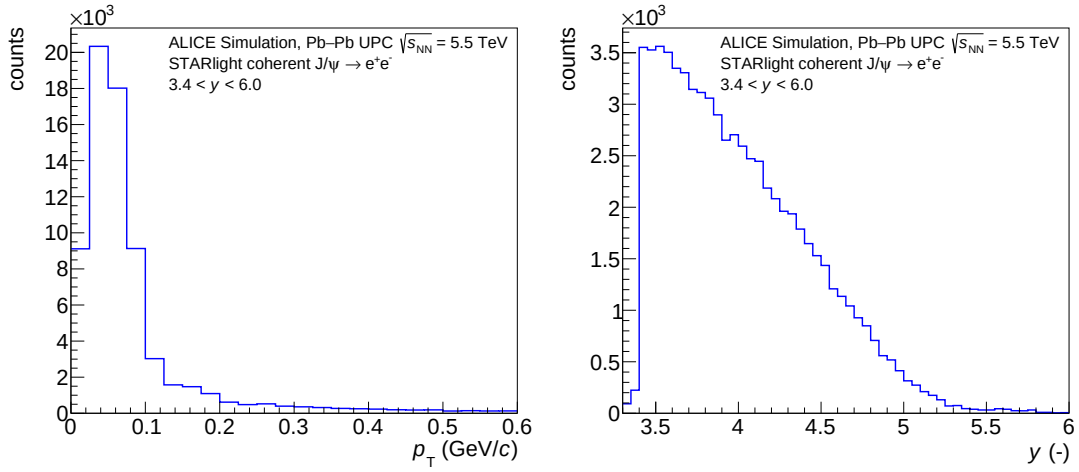


**Fig. 56:** Transverse momentum (left) and rapidity (right) distributions of generated coherent $\mathrm{J}/\psi$ by StarLight.

rapidity distributions for generated coherent $\mathrm{J}/\psi$ in Pb–Pb collisions at $\sqrt{s_{\mathrm{NN}}} = 5.5$ TeV are shown in Figure 56. It can be observed that most of the generated $\mathrm{J}/\psi$ population is at $p_{\mathrm{T}} < 200$ MeV, while the rapidity distributions drops fast with very little $\mathrm{J}/\psi$ being produced at $y > 5.5$.

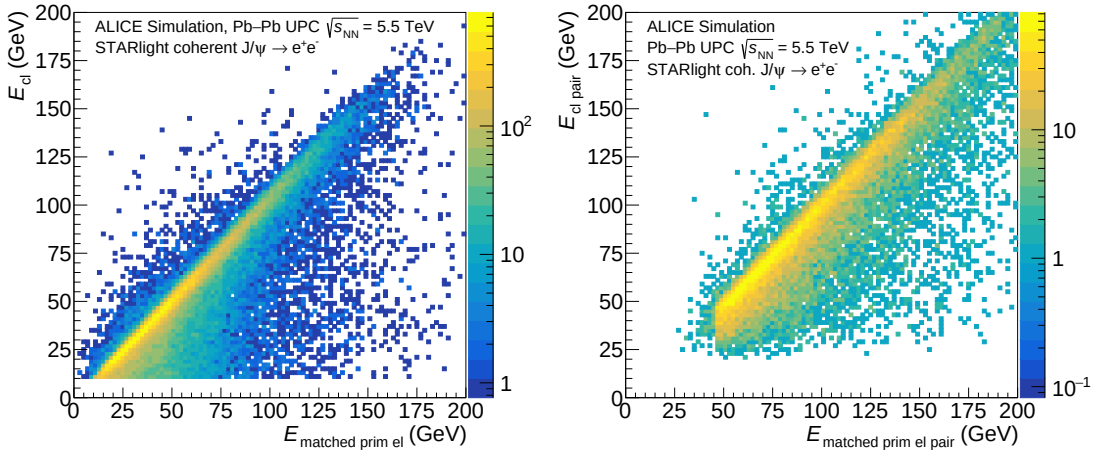


**Fig. 57:** Left: Energy of the matched primary electron from $\mathrm{J}/\psi$ decay as a function of the reconstructed supercluster energy. Right: Energy of the matched electron pair from a $\mathrm{J}/\psi$ decay as a function of the reconstructed supercluster pair energy.

The clusters, reconstructed from the hits generated in the STARlight + GEANT3 simulations, are selected to have a minimum energy of 10 GeV for this analysis. The correlation between the generator and detector level for a single primary electron and an electron pair ($\mathrm{J}/\psi$ candidate) is shown in Figure 57 in the left and right panels, respectively. The distribution shows a good correlation in both cases.

The kinematical acceptance, reconstruction and signal extraction efficiency are shown in Figure 58 and are computed as the fraction of cluster pairs matched to a true pair of $\mathrm{J}/\psi$ decay electrons from the total amount of generated $\mathrm{J}/\psi$ mesons. Since the coherent $\mathrm{J}/\psi$ are generated in a narrow interval in $p_{\mathrm{T}}$, their efficiency is shown here only as a function of rapidity, $y$, and integrated over $p_{\mathrm{T}}$. The total reconstruction

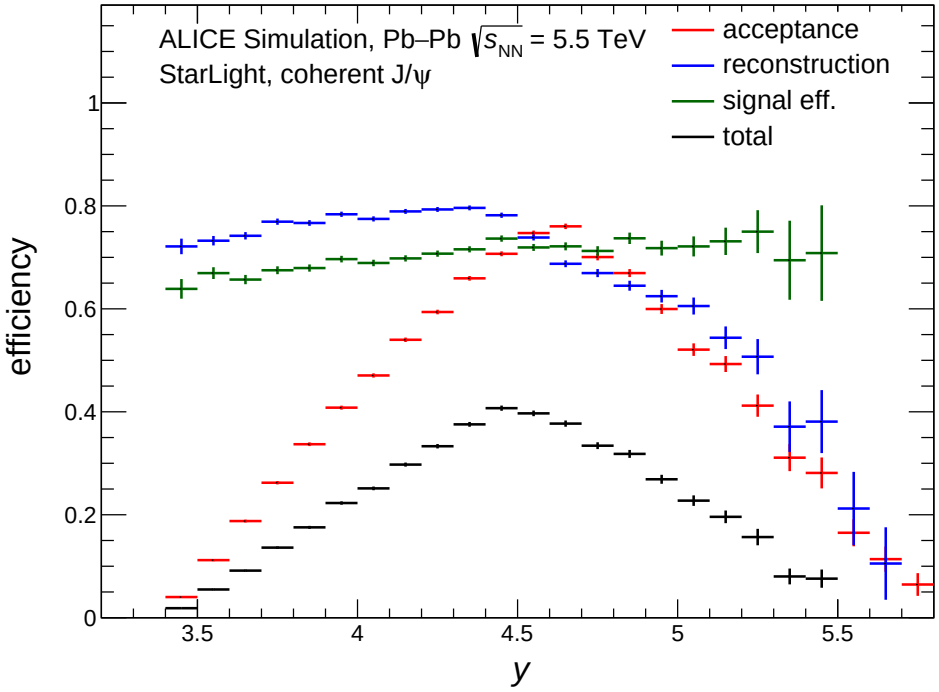


**Fig. 58:** Acceptance and reconstruction efficiency for coherent $J/\psi$ in ultra-peripheral Pb–Pb collisions at $\sqrt{s_{NN}}$=5.5 TeV. The signal efficiency is computed using the fraction of reconstructed cluster pairs in the invariant mass range $[2.5, 3.5]$ GeV$/c^2$.

efficiency is the product of the kinematical acceptance, reconstruction efficiency and signal efficiency. The kinematical acceptance, which is the fraction of $J/\psi$ which emits both the decay electrons in the FoCal acceptance, shows a maximum of nearly 75% which then drops to zero towards the edges of the FoCal acceptance. The reconstruction efficiency, defined as the fraction of reconstructed $J/\psi$ electron pairs out of all the pairs emitted in the FoCal acceptance, has a maximum of about 80% at the lowest rapidity and drops monotonically towards the most forward rapidity, with a sharp drop for $y > 5.3$. The signal efficiency, defined as the fraction of $J/\psi$ candidates reconstructed in the invariant mass range $[2.5, 3.5]$ GeV$/c^2$, is about 60% at $y = 3.4$ and grows nearly linearly towards high rapidity up to about 70%. The reason for the growth is due to the increasing energy of the $J/\psi$ decay electrons towards high rapidity which have a better energy resolution in a calorimeter like FoCal. This is then leading to a narrower $J/\psi$ invariant mass distribution. The total efficiency has a maximum of about 40%, falling to zero towards the FoCal acceptance edges, but is non-zero up to $y \approx 5.5$.

The invariant mass distribution for cluster pairs with $p_T < 200$ MeV$/c$ obtained from summing the coherent $J/\psi$ and $\psi(2S)$ STARlight Pb–Pb simulations is shown in Figure 59. The two panels show the same distribution, but in linear (left) and logarithmic (right) vertical scales, for better visibility of both resonances. The two contributions are scaled such that they are in agreement with the $\psi(2S)/J/\psi$ ratio measured in data. The signal extraction is performed using the sum of two double-sided Crystal Ball functions, one for each meson. In order to improve the fit stability, the mass pole parameters are constrained to be close to the PDG values, and the tail parameters of the $\psi(2S)$ are constrained to be similar to the ones of the $J/\psi$. The fit shows clearly that the $J/\psi$ and $\psi(2S)$ states can be well separated with FoCal. Also, the amount of charmonium states to be seen in the FoCal acceptance with the expected integrated luminosity in Run 4, $\mathscr{L}_{\text{int}} = 7$ nb$^{-1}$, is about 370000 $J/\psi$ and 7500 $\psi(2S)$ states which would provide a very good dataset for detailed differential studies. An important aspect of the measurement of photoproduced vector mesons is the capability of separating the different production processes, which have characteristic $p_T$ distributions. Figure 60 shows the transverse momentum distribution of cluster

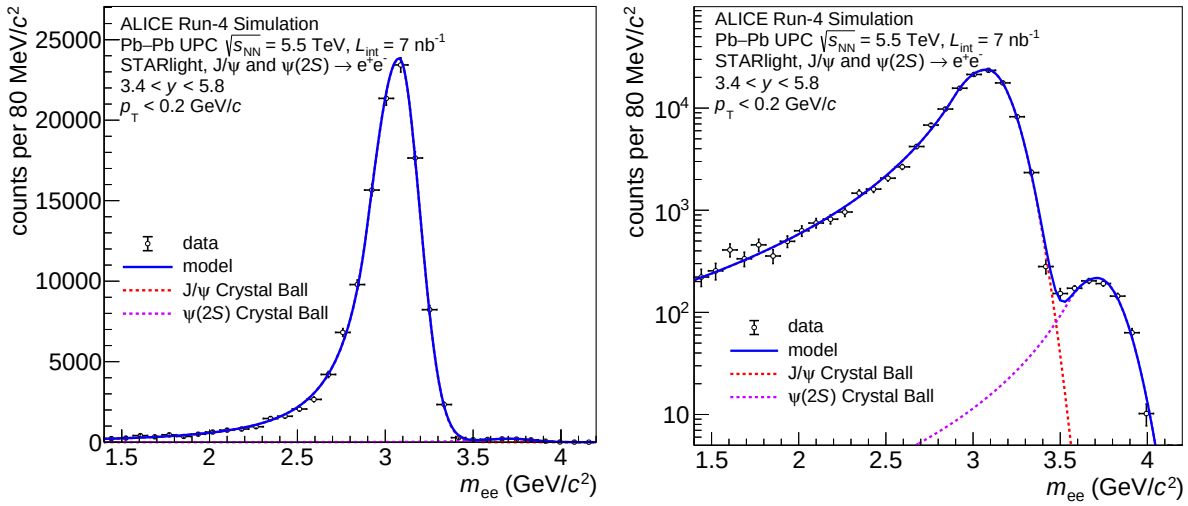


**Fig. 59:** Invariant mass distribution from cluster pairs reconstructed with a $p_{\mathrm{T}}$ in the interval $[0, 0.2]$ GeV$/c$ . The distribution is fitted with two Crystall Ball functions [12], one for J$/\psi$ and another for $\psi(2\mathrm{S})$.

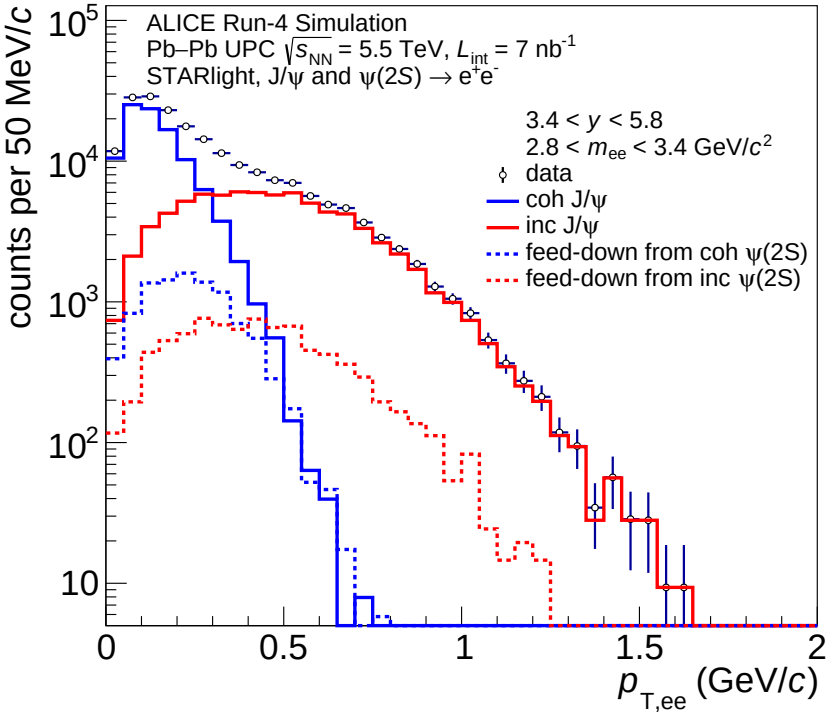


**Fig. 60:** Transverse momentum distribution for cluster pairs reconstructed with an invariant mass in the interval $[2.8, 3.4]$ GeV$/c^2$. The histogram shows the total distribution, while the colored lines show the coherent (blue) and incoherent (red) J$/\psi$ components, with solid lines for the direct J$/\psi$ and dashed lines for the feed-down from $\psi(2\mathrm{S})$ decays.

pairs in the invariant mass range $[2.8, 3.4]$ GeV$/c^2$ as the sum (black) of both coherent (blue) and incoherent (red) distributions including the corresponding feed-down contribution from $\psi(2S)$. The relative normalization is the one predicted by STARLight. The coherent and incoherent contributions maintain a very distinct shape, with most of the coherent yield being reconstructed at a $p_{\mathrm{T}}$ below 300 MeV$/c$, where it is the dominant component.

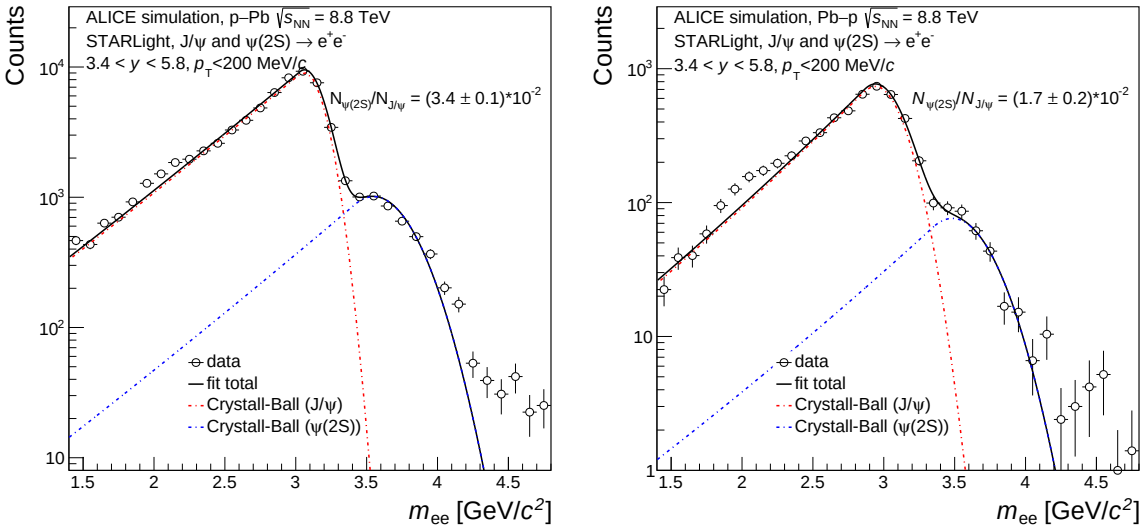


**Fig. 61:** Invariant mass distribution from cluster pairs reconstructed with a $p_{\mathrm{T}}$ in the interval $[0,0.2]$ GeV$/c$ in p–Pb (left) and Pb-p (right) collisions. The distribution is fitted with two Crystal Ball functions, one for J$/\psi$ and another for $\psi(2\mathrm{S})$. The simulated samples are selected to reflect the expected integrated luminosity for Run 4.

In Run 4, the LHC is expected to provide also a p–Pb collisions run at $\sqrt{s_{\mathrm{NN}}}$=8.8 TeV with an integrated luminosity of 150 nb$^{-1}$ for the case when the proton beam moves towards FoCal and a similar run with reversed beams, when the Pb ion moves towards FoCal. The two beam configurations, dubbed p–Pb and Pb–p, provide in the case of UPCs coverage for extreme values for the photon-proton center of mass energy, $W_{\gamma p}$. In the case of p–Pb, the $W_{\gamma p}$ goes up to about 2 TeV, while in the case of Pb–p, the coverage extends to as low as 10 GeV. The projected number of photoproduced charmonia from Ref. [45] were simulated and reconstructed and the obtained invariant mass distributions are shown in Figure 61 for both beam configurations. For the p–Pb case, the expected statistical uncertainty is negligible for J$/\psi$ and a few percent in the case of $\psi(2S)$. In particular, the $\psi(2S)/\mathrm{J}/\psi$ ratio is highlighted in Ref. [45] and is expected to provide a good separation power for models assuming linear gluon PDF evolution from the ones assuming saturation. In the case of Pb–p collisions, the $\psi(2S)/\mathrm{J}/\psi$ ratio is expected to be measured with a statistical uncertainty of about 15% while the effects of saturation are predicted to be at the level of 50% in this kinematic range.

## 10 Summary

The FoCal detector is a highly-granular Si+W electromagnetic calorimeter combined with a conventional sampling hadronic calorimeter, covering the pseudorapidity interval of $3.2 < \eta < 5.8$. The FoCal detector will be installed during the LHC Long-Shutdown 3 (LS3), and take data during LHC Run 4 for pp, p–Pb, and Pb–Pb collisions. The focus of the FoCal physics program is the study of the low-$x$ structure of matter and the search for evidence of non-linear QCD evolution. The FoCal design is optimized to measure isolated photons at very forward rapidity for $p_{\mathrm{T}} \gtrsim 4$ GeV/$c$, as well as neutral hadrons, vector mesons, and jets.

This note presents projections of the performance of FoCal for key observables in this program. Performance projections are presented for isolated photons (Fig. 20 and Fig. 21), for $\pi^0$ and $\eta$ mesons (Fig. 30 and Fig. 32), jets in (Fig. 41), and J/$\psi$ in UPCs (Fig. 58 and Fig. 60). Studies are also shown of $\pi^0$–$\pi^0$ correlations (Fig. 50) and $\gamma$–$\pi^0$ correlations (Fig. 52).

These projections are our current assessment ofFoCal performance. The note will be updated periodically, when additional studies provide further insight into FoCal physics performance.

## Acknowledgments

The ALICE Collaboration would like to thank all its engineers and technicians for their invaluable contributions to the construction of the experiment and the CERN accelerator teams for the outstanding performance of the LHC complex. The ALICE Collaboration gratefully acknowledges the resources and support provided by all Grid centres and the Worldwide LHC Computing Grid (WLCG) collaboration. The ALICE Collaboration acknowledges the following funding agencies for their support in building and running the ALICE detector: A. I. Alikhanyan National Science Laboratory (Yerevan Physics Institute) Foundation (ANSL), State Committee of Science and World Federation of Scientists (WFS), Armenia; Austrian Academy of Sciences, Austrian Science Fund (FWF): [M 2467-N36] and Nationalstiftung für Forschung, Technologie und Entwicklung, Austria; Ministry of Communications and High Technologies, National Nuclear Research Center, Azerbaijan; Conselho Nacional de Desenvolvimento Científico e Tecnológico (CNPq), Financiadora de Estudos e Projetos (Finep), Fundação de Amparo à Pesquisa do Estado de São Paulo (FAPESP) and Universidade Federal do Rio Grande do Sul (UFRGS), Brazil; Bulgarian Ministry of Education and Science, within the National Roadmap for Research Infrastructures 2020¿2027 (object CERN), Bulgaria; Ministry of Education of China (MOEC) , Ministry of Science & Technology of China (MSTC) and National Natural Science Foundation of China (NSFC), China; Ministry of Science and Education and Croatian Science Foundation, Croatia; Centro de Aplicaciones Tecnológicas y Desarrollo Nuclear (CEADEN), Cubaenergía, Cuba; Ministry of Education, Youth and Sports of the Czech Republic, Czech Republic; The Danish Council for Independent Research — Natural Sciences, the VILLUM FONDEN and Danish National Research Foundation (DNRF), Denmark; Helsinki Institute of Physics (HIP), Finland; Commissariat à l'Energie Atomique (CEA) and Institut National de Physique Nucléaire et de Physique des Particules (IN2P3) and Centre National de la Recherche Scientifique (CNRS), France; Bundesministerium für Bildung und Forschung (BMBF) and GSI Helmholtzzentrum für Schwerionenforschung GmbH, Germany; General Secretariat for Research and Technology, Ministry of Education, Research and Religions, Greece; National Research, Development and Innovation Office, Hungary; Department of Atomic Energy Government of India (DAE), Department of Science and Technology, Government of India (DST), University Grants Commission, Government of India (UGC) and Council of Scientific and Industrial Research (CSIR), India; National Research and Innovation Agency - BRIN, Indonesia; Istituto Nazionale di Fisica Nucleare (INFN), Italy; Japanese Ministry of Education, Culture, Sports, Science and Technology (MEXT) and Japan Society for the Promotion of Science (JSPS) KAKENHI, Japan; Consejo Nacional de Ciencia (CONACYT) y Tecnología, through Fondo de Cooperación Internacional en Ciencia y Tecnología (FONCICYT) and Dirección General de Asuntos del Personal Academico (DGAPA), Mexico; Nederlandse Organisatie voor Wetenschappelijk Onderzoek (NWO), Netherlands; The Research Council of Norway, Norway; Com-

mission on Science and Technology for Sustainable Development in the South (COMSATS), Pakistan; Pontificia Universidad Católica del Perú, Peru; Ministry of Education and Science, National Science Centre and WUT ID-UB, Poland; Korea Institute of Science and Technology Information and National Research Foundation of Korea (NRF), Republic of Korea; Ministry of Education and Scientific Research, Institute of Atomic Physics, Ministry of Research and Innovation and Institute of Atomic Physics and University Politehnica of Bucharest, Romania; Ministry of Education, Science, Research and Sport of the Slovak Republic, Slovakia; National Research Foundation of South Africa, South Africa; Swedish Research Council (VR) and Knut & Alice Wallenberg Foundation (KAW), Sweden; European Organization for Nuclear Research, Switzerland; Suranaree University of Technology (SUT), National Science and Technology Development Agency (NSTDA) and National Science, Research and Innovation Fund (NSRF via PMU-B B05F650021), Thailand; Turkish Energy, Nuclear and Mineral Research Agency (TENMAK), Turkey; National Academy of Sciences of Ukraine, Ukraine; Science and Technology Facilities Council (STFC), United Kingdom; National Science Foundation of the United States of America (NSF) and United States Department of Energy, Office of Nuclear Physics (DOE NP), United States of America. In addition, individual groups or members have received support from: European Research Council, Strong 2020 - Horizon 2020 (grant nos. 950692, 824093), European Union; Academy of Finland (Center of Excellence in Quark Matter) (grant nos. 346327, 346328), Finland.

## References

[1] **ALICE** Collaboration, "Letter of Intent: A Forward Calorimeter (FoCal) in the ALICE experiment", tech. rep., CERN, Geneva, 2020. `https://cds.cern.ch/record/2719928`.

[2] **ALICE** Collaboration, A. S. *et al.*, "Physics of the ALICE Forward Calorimeter upgrade",. `https://inspirehep.net/literature/2661418`. ALICE-PUBLIC-2023-001.

[3] **CMS** Collaboration, F. Bouyjou *et al.*, "HGCROC3: the front-end readout ASIC for the CMS High Granularity Calorimeter", *JINST* **17** (2022) C03015.

[4] **ALICE** Collaboration, G. Aglieri Rinella, "The ALPIDE pixel sensor chip for the upgrade of the ALICE Inner Tracking System", *Nucl. Instrum. Meth.* **A845** (2017) 583–587.

[5] R. Brun, P. Buncic, F. Carminati, A. Morsch, F. Rademakers, and K. Safarik, "Computing in ALICE", *Nucl. Instrum. Meth. A* **502** (2003) 339–346.

[6] R. Brun *et al.*, *GEANT: Detector Description and Simulation Tool; Oct 1994*. CERN Program Library. CERN, Geneva, 1993. `http://cds.cern.ch/record/1082634`. Long Writeup W5013.

[7] **GEANT4** Collaboration, S. Agostinelli *et al.*, "GEANT4–a simulation toolkit", *Nucl. Instrum. Meth. A* **506** (2003) 250–303.

[8] T. Sjostrand, S. Mrenna, and P. Z. Skands, "PYTHIA 6.4 Physics and Manual", *JHEP* **0605** (2006) 026, `arXiv:hep-ph/0603175 [hep-ph]`.

[9] X.-N. Wang and M. Gyulassy, "HIJING: A Monte Carlo model for multiple jet production in pp, pA and AA collisions", *Phys. Rev. D* **44** (1991) 3501–3516.

[10] **ALICE** Collaboration, W. H. Trzaska, "New Fast Interaction Trigger for ALICE", *Nucl. Instrum. Meth.* **A845** (2017) 463–466.

[11] F. collaboraion, "Performance of the electromagnetic and hadronic prototype segments of the ALICE FoCal", `arXiv:in preparation [physics.ins-det]`.

[12] J. E. Gaiser, "Charmonium Spectroscopy From Radiative Decays of the $J/\psi$ and $\psi'$", ph.d. thesis, 8, 1982.

[13] G. David, "Direct real photons in relativistic heavy ion collisions", *Rept. Prog. Phys.* **83** (2020) 046301, arXiv:1907.08893 [nucl-ex].

[14] **ALICE** Collaboration, S. Acharya *et al.*, "Measurement of the inclusive isolated photon production cross section in pp collisions at $\sqrt{s} = 7$ TeV", *Eur. Phys. J. C* **79** (2019) 896, arXiv:1906.01371 [nucl-ex].

[15] M. van Leeuwen, "Constraining nuclear Parton Density Functions with forward photon production at the LHC", arXiv:1909.05338 [hep-ph].

[16] INCNLO, "Incnlo-direct photon and inclusive hadron production code - incnlo version 1.4", 2002. https://lapth.cnrs.fr/PHOX_FAMILY/readme_inc.html, accessed 09/04/2023.

[17] F. Aversa, P. Chiappetta, M. Greco, and J. P. Guillet, "QCD Corrections to Parton-Parton Scattering Processes", *Nucl. Phys. B* **327** (1989) 105.

[18] P. Aurenche, R. Baier, M. Fontannaz, and D. Schiff, "Prompt Photon Production at Large p(T) Scheme Invariant QCD Predictions and Comparison with Experiment", *Nucl. Phys. B* **297** (1988) 661–696.

[19] P. Aurenche, M. Fontannaz, J. P. Guillet, B. A. Kniehl, E. Pilon, and M. Werlen, "A Critical phenomenological study of inclusive photon production in hadronic collisions", *Eur. Phys. J. C* **9** (1999) 107–119, arXiv:hep-ph/9811382.

[20] P. Aurenche, M. Fontannaz, J. P. Guillet, B. A. Kniehl, and M. Werlen, "Large p(T) inclusive pi0 cross-sections and next-to-leading-order QCD predictions", *Eur. Phys. J. C* **13** (2000) 347–355, arXiv:hep-ph/9910252.

[21] R. A. Khalek, R. Gauld, T. Giani, E. R. Nocera, T. R. Rabemananjara, and J. Rojo, "nNNPDF3.0: Evidence for a modified partonic structure in heavy nuclei", arXiv:2201.12363 [hep-ph].

[22] **LHCb** Collaboration, R. Aaij *et al.*, "Study of prompt $D^0$ meson production in *p*Pb collisions at $\sqrt{s_{NN}} = 5$ TeV", *JHEP* **10** (2017) 090, arXiv:1707.02750 [hep-ex].

[23] **CMS** Collaboration, A. M. Sirunyan *et al.*, "Studies of charm and beauty hadron long-range correlations in pp and pPb collisions at LHC energies", *Phys. Lett. B* **813** (2021) 136036, arXiv:2009.07065 [hep-ex].

[24] J.-w. Qiu, "QCD factorization and rescattering in proton nucleus collisions", arXiv:hep-ph/0305161.

[25] A. Accardi *et al.*, "Hard probes in heavy ion collisions at the lhc: pdfs, shadowing and pa collisions", in *3rd Workshop on Hard Probes in Heavy Ion Collisions: 3rd Plenary Meeting*. 10, 2004. arXiv:hep-ph/0308248.

[26] K. Kovarik *et al.*, "nCTEQ15 - Global analysis of nuclear parton distributions with uncertainties in the CTEQ framework", *Phys. Rev. D* **93** (2016) 085037, arXiv:1509.00792 [hep-ph].

[27] M. Cacciari, G. P. Salam, and G. Soyez, "The anti-$k_t$ jet clustering algorithm", *JHEP* **04** (2008) 063, arXiv:0802.1189 [hep-ph].

[28] http://fastjet.fr/repo/doxygen-3.1.3/.

[29] K. Tuchin, "Rapidity and centrality dependence of azimuthal correlations in deuteron-gold collisions at RHIC", *Nucl. Phys. A* **846** (2010) 83–94, arXiv:0912.5479 [hep-ph].

[30] J. L. Albacete and C. Marquet, "Azimuthal correlations of forward di-hadrons in d+Au collisions at RHIC in the Color Glass Condensate", *Phys. Rev. Lett.* **105** (2010) 162301, arXiv:1005.4065 [hep-ph].

[31] Z.-B. Kang, I. Vitev, and H. Xing, "Dihadron momentum imbalance and correlations in d–Au collisions", *Phys. Rev. D* **85** (2012) 054024, arXiv:1112.6021 [hep-ph].

[32] A. Stasto, B.-W. Xiao, and F. Yuan, "Back-to-back correlations of di-hadrons in d–Au collisions at RHIC", *Phys. Lett. B* **716** (2012) 430–434, arXiv:1109.1817 [hep-ph].

[33] T. Lappi and H. Mantysaari, "Forward dihadron correlations in deuteron-gold collisions with the Gaussian approximation of JIMWLK", *Nucl. Phys. A* **908** (2013) 51–72, arXiv:1209.2853 [hep-ph].

[34] L. Zheng, E. C. Aschenauer, J. H. Lee, and B.-W. Xiao, "Probing Gluon Saturation through dihadron correlations at an Electron-Ion Collider", *Phys. Rev. D* **89** (2014) 074037, arXiv:1403.2413 [hep-ph].

[35] J. L. Albacete, G. Giacalone, C. Marquet, and M. Matas, "Forward dihadron back-to-back correlations in pA collisions", *Phys. Rev.* **D99** (2019) 014002, arXiv:1805.05711 [hep-ph].

[36] A. Stasto, S.-Y. Wei, B.-W. Xiao, and F. Yuan, "On the dihadron angular correlations in forward pA collisions", *Phys. Lett.* **B784** (2018) 301–306, arXiv:1805.05712 [hep-ph].

[37] A. K. Kohara, C. Marquet, and V. Vila, "Low projectile density contributions in the dilute-dense CGC framework for two-particle correlations", arXiv:2303.08711 [hep-ph].

[38] **PHENIX** Collaboration, A. Adare *et al.*, "Suppression of back-to-back hadron pairs at forward rapidity in d–Au collisions at $\sqrt{s_{\rm NN}} = 200$ GeV", *Phys. Rev. Lett.* **107** (2011) 172301, arXiv:1105.5112 [nucl-ex].

[39] **STAR** Collaboration, M. S. Abdallah *et al.*, "Evidence for nonlinear gluon effects in QCD and their mass number dependence at STAR", *Phys. Rev. Lett.* **129** (2022) 092501, arXiv:2111.10396 [nucl-ex].

[40] C. Bierlich *et al.*, "A comprehensive guide to the physics and usage of PYTHIA 8.3", arXiv:2203.11601 [hep-ph].

[41] **PHENIX** Collaboration, S. S. Adler *et al.*, "Jet properties from dihadron correlations in $p^+p$ collisions at $\sqrt{s}$ = 200-GeV", *Phys. Rev. D* **74** (2006) 072002, arXiv:hep-ex/0605039.

[42] **ALICE** Collaboration, S. Acharya *et al.*, "Measurement of isolated photon-hadron correlations in $\sqrt{s_{\rm NN}}$ = 5.02 TeV $pp$ and $p$-Pb collisions", *Phys. Rev. C* **102** (2020) 044908, arXiv:2005.14637 [nucl-ex].

[43] T. Adye, "Unfolding algorithms and tests using RooUnfold", in *PHYSTAT 2011*, pp. 313–318. CERN, Geneva, 2011. arXiv:1105.1160 [physics.data-an].

[44] R. Abdul Khalek *et al.*, "Science Requirements and Detector Concepts for the Electron-Ion Collider: EIC Yellow Report", *Nucl. Phys. A* **1026** (2022) 122447, arXiv:2103.05419 [physics.ins-det].

[45] A. Bylinkin, J. Nystrand, and D. Tapia Takaki, "Vector meson photoproduction in UPCs with FoCal", arXiv:2211.16107 [nucl-ex].

[46] S. R. Klein, J. Nystrand, J. Seger, Y. Gorbunov, and J. Butterworth, "STARlight: A Monte Carlo simulation program for ultra-peripheral collisions of relativistic ions", *Comput. Phys. Commun.* **212** (2017) 258–268, arXiv:1607.03838 [hep-ph].

[47] T. Sjöstrand, S. Ask, J. R. Christiansen, R. Corke, N. Desai, P. Ilten, S. Mrenna, S. Prestel, C. O. Rasmussen, and P. Z. Skands, "An Introduction to PYTHIA 8.2", *Comput. Phys. Commun.* **191** (2015) 159–177, arXiv:1410.3012 [hep-ph].

# A Event generators

In order to simulate the physics processes to be reconstructed with FoCal, so called event generators which are C++ classes inheriting from the virtual AliGenerator class are being configured using the AliRoot libraries. These generators have an interface allowing them to be configured and be combined with other generators using a standardized framework. Within the whole simulation chain, they are the first component to be run, leading to the creation of a particle list which will contain the final state particles that are taken over for particle transport through the detector setup, but may contain also already decayed particles typically used to identify the physics origin of final state particles.

Several event generators were employed for the performance studies described in the later sections. Some event generators do not contain any physics, but are just designed to generate one or more particles with a specified kinematics in order to test various aspects of the detector performance. Other generators rely on known physics models, such as PYTHIA [47] or HIJING [9]. The generators frequently employed in the later sections are the following:

- *gun*: a generator used to simulate single particle events of a given species and at a fixed momentum and pseudorapidity;
- *box*: a generator which simulate single particle events of a specified particle species, but in a predefined kinematics interval, such as the energy or $p_{\mathrm{T}}$;
- *min bias pp collisions*: PYTHIA generated minimum bias pp collisions;
- *physics triggered pp collisions*: PYTHIA generated pp collisions selected such that it fulfills a given condition, such as a $p_{\mathrm{T}}$-hard condition or a particle with a given $p_{\mathrm{T}}$ is generated within the FoCal acceptance;
- *min bias p–Pb collisions*: HIJING generated minimum bias p–Pb collisions;
- *physics triggered p–Pb collisions*: a cocktail of a minimum bias p–Pb event generated with HIJING and a triggered pp collision generated with PYTHIA;
- *min bias Pb–Pb collisions*: HIJING generated Pb–Pb minimum bias collisions;
- *ultra-peripheral p–Pb and ultra-peripheral Pb–Pb collisions*: Ultra-peripheral collisions generated using STARLight [46] for the photo-production of vector mesons, such as $\mathrm{J}/\psi$ and $\psi(2S)$;
- *pp and p–Pb collisions with pile-up*: a cocktail of a pp or p–Pb triggered event (see above) and a number of minimum bias pp or p–Pb collisions, respectively.

# B Clusterization algorithm performance

## B.1 Single-photon performance

The performance of this shower clustering algorithm is studied using box simulations where a single photon per event is simulated. For this simulation, the photon energy spectrum is artificially chosen to be constant as a function of the photon energy between zero and 1.5 TeV and to cover the entire sensitive area of the detector. Ideally, the reconstruction / clusterisation algorithm performed for these simulated events would lead to one cluster per event. However, due to the presence of detector material in front of FoCal, imperfections of the clustering algorithm (e.g. cluster splitting), and insensitive areas, one can reconstruct zero, one or multiple clusters for every given event. The left panel of Fig. B.1 shows the distribution of the number of clusters per event reconstructed for the single photon box simulations. The distribution peaks at one cluster per event, however, about 10% of events do not have any reconstructed cluster and about 15% of events have more than one cluster. The right panel of Fig. B.1 shows the transversal spatial $(x,y)$ distribution of the reconstructed clusters in FoCal-E. The transverse position of the cluster is computed as an energy-weighted sum over the cells belonging to a given cluster. Overall, the distribution has a radial symmetry peaking at small radii where the generated photon density is

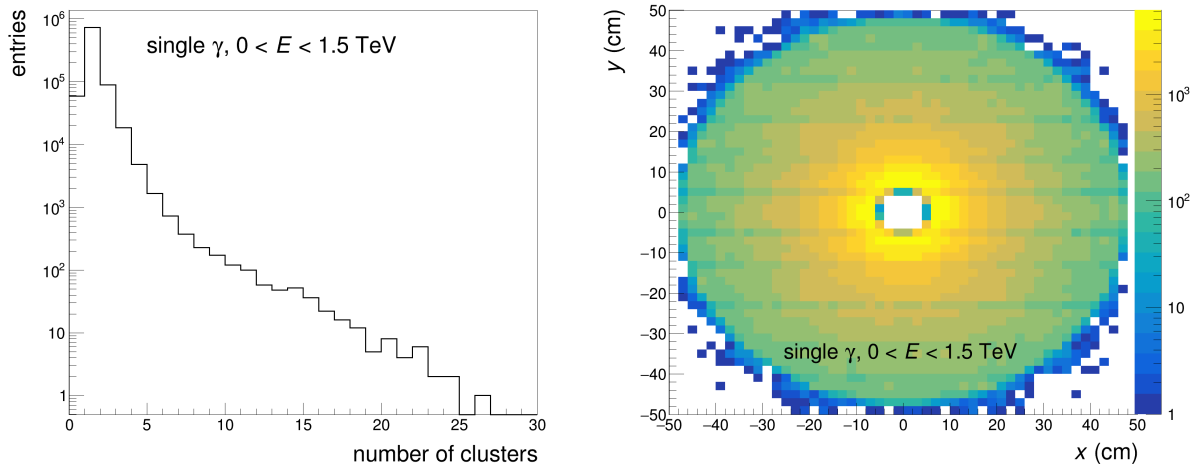


**Fig. B.1:** Left: Distribution of the number of reconstructed clusters per event in single photon simulations. Right: Spatial $(x,y)$ distribution of the reconstructed FoCal-E clusters.

largest. However, non-uniformities in the distribution can be observed which are due to inefficiencies at inter-module regions.

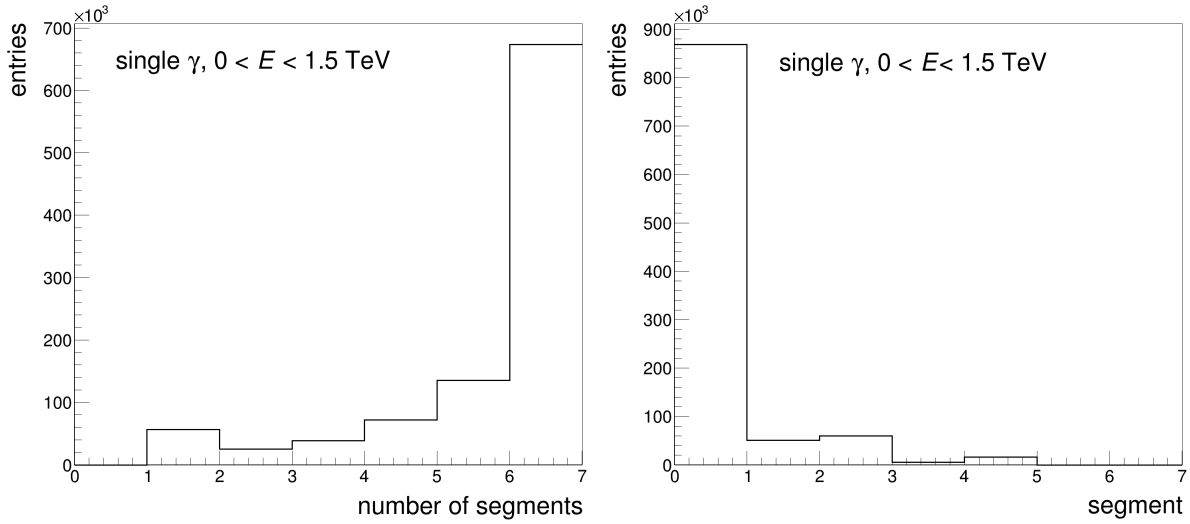


**Fig. B.2:** Left: Distribution of the number of longitudinal segments contributing to a FoCal-E cluster. Right: Distribution of the first segment in a FoCal-E cluster.

The deposited energy of a shower is deposited longitudinally in FoCal-E being spread over the six logical segments. An ideal electro-magnetic shower (initiated by a photon or electron hitting FoCal) starts very early and, for the energy range expected at the LHC in the relevant FoCal kinematics, should extend typically over all the six segments while showers initiated by hadrons are affected by large fluctuations in both the deposited energy and the position where the shower starts. For the case of photon initiated showers, the distributions of the number of segments and of the first segment in the shower are illustrated in Figure B.2 in the left and right panels, respectively. The distributions are integrated over the whole simulated photon sample. The majority of the reconstructed clusters have the maximum number of segments and the shower initiated in the first segment, as expected for a photon shower.

In order to understand the origin of events with multiple reconstructed clusters, the clusters are combined into pairs and their characteristics are studied as a function of pair observables. The combinatorics is performed using the energy-ordered list of clusters, starting with the highest energy cluster. The

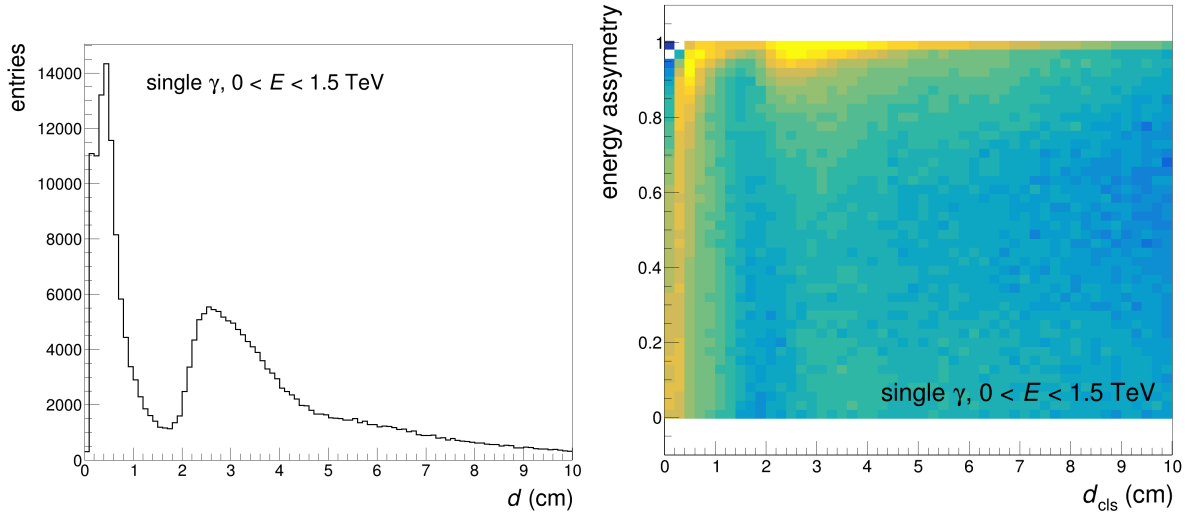


**Fig. B.3:** Left: Distribution of the inter-cluster distance for the single photon simulations (see text for details). Right: Energy asymmetry between cluster pairs as a function of the inter-cluster distance.

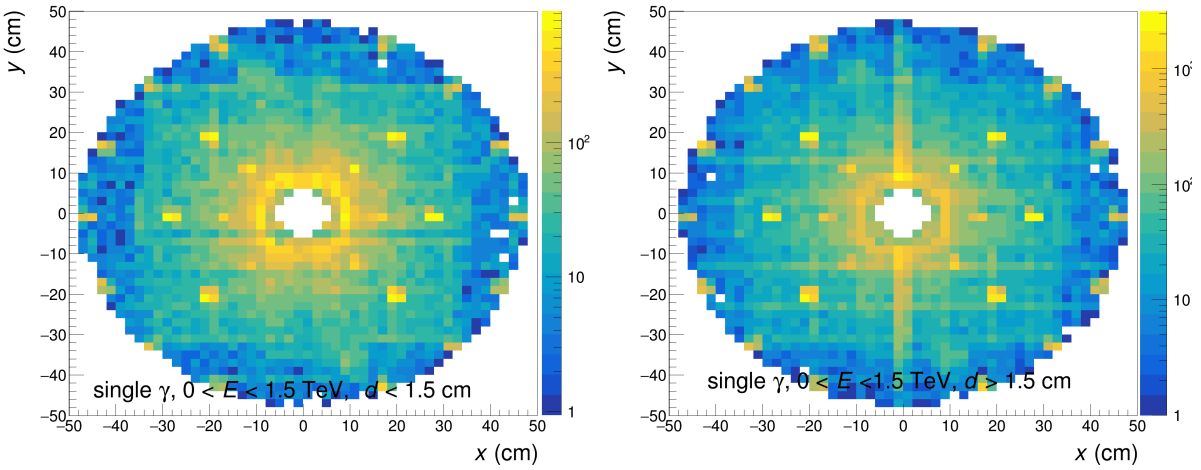


**Fig. B.4:** Spatial $(x, y)$ distribution for clusters in events where more than one cluster was reconstructed, and the inter-cluster distance is below 1.5 cm (left) or above 1.5 cm (right).

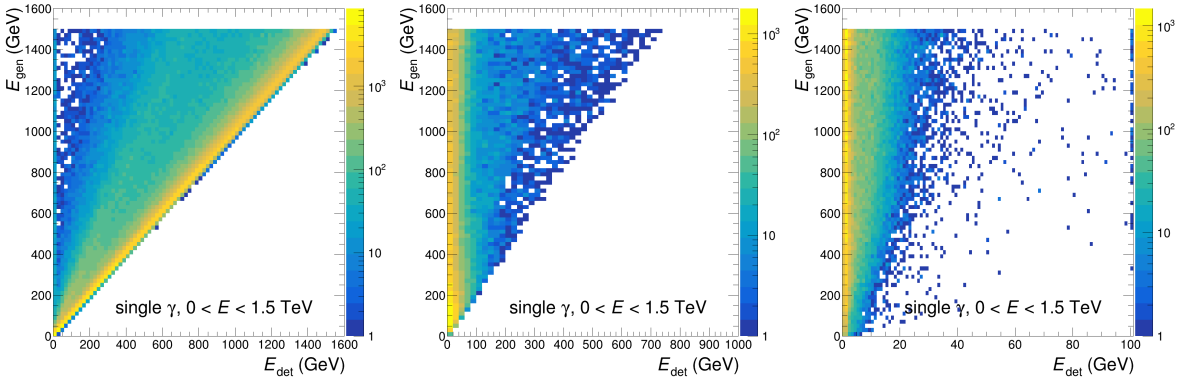


**Fig. B.5:** Reconstructed cluster energy ($E_{\mathrm{det}}$) as a function of the generator-level photon energy ($E_{\mathrm{gen}}$) for event where a single cluster was reconstructed (left) and events where multiple clusters were reconstructed for cluster with inter-cluster distance below 1.5 cm (middle) and above 1.5 cm (right).

distribution of the inter-cluster distance is shown in the left panel of Fig. B.3 and exhibits a double peaked structure indicating at least two distinct sources for the clusters in multiple-cluster events. The first source, is characterized by a small inter-cluster distance, below 1 cm, which is expected to originate from cluster splitting. The second source, dominating at large inter-cluster distances, originates from secondary particles which branched out from the primary photon at a very early stage, most likely in the material in between the nominal interaction vertex and the entrance into FoCal. In support of this classification, the right panel of Fig. B.3, shows the energy asymmetry of the cluster pairs as a function of the inter-cluster distance. An energy asymmetry of zero signifies that the energy of the clusters in the pair is perfectly balanced, while unity is for a completely unbalanced pair. It can be observed that for pairs with small inter-cluster distance, the energy asymmetry distribution is relatively uniform, while for large distances, the pairs are very unbalanced, with one of the clusters carrying the large majority of the pair energy. Moreover, in Fig. B.4, the transverse two-dimensional spatial distributions for clusters in multi-cluster events are shown. For both cases, small and large distance cluster pairs, the distributions exhibit several hot regions which correspond to the shadows of the thickest materials in front of FoCal, namely the beam pipe (circular region at small radii), the beam pipe flange screws (hot spots at a radius of approximately 20cm), FV0 detector PMTs (hot spots at radii of 30 and 50cm) and the FT0 scintillator array (square area between $(-30, +30)$cm).

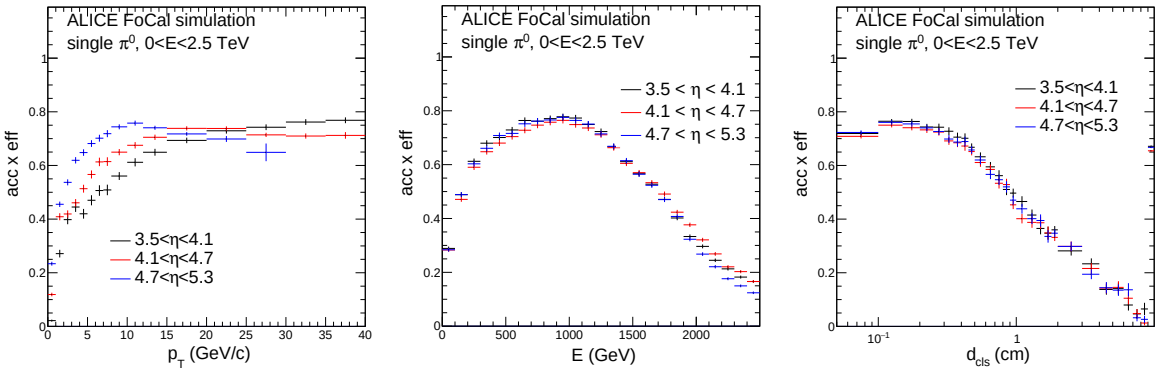


**Fig. B.6:** $\pi^0$ reconstruction efficiency using a set of clusterization parameters optimized for improved efficiency at high $\pi^0$ energy.

Finally, the quality of the clusterization procedure is checked via the correlation between the generator level primary photon energy and the energy of the reconstructed cluster. Figure B.5 shows this correlation for the case of events where one single cluster was reconstructed (left panel) and for the case with multiple clusters with small inter-cluster distance (middle panel) and large inter-cluster distance (right panel). In the single-cluster case, a very good diagonal correlation is observed with a relatively small tail towards lower reconstructed energy which is due to losses at edges and energy leakage. For the events where multiple clusters were reconstructed, the distributions show small fractions of reconstructed energy out of the energy of the generated photon.

### B.2 Neutral pion performance

The clusterization parameters can be optimized to improve performance in different kinematic regions. Figure B.6 shows the $\pi^0$ reconstruction efficiency as a function of $p_{\mathrm{T}}$, energy and the distance between the two photon showers. These efficiency are obtained with a set of parameters designed to split more the clusters. As the plots show, the $\pi^0$ reconstruction efficiency is improved at high $p_{\mathrm{T}}$, high energy and small $d_{cls}$.

## C The ALICE Collaboration

S. Acharya [126], D. Adamová [86], G. Aglieri Rinella [33], M. Agnello [30], N. Agrawal [51], Z. Ahammed [134], S. Ahmad[16], S.U. Ahn [71], I. Ahuja [38], A. Akindinov [142], M. Al-Turany [97], D. Aleksandrov [142], B. Alessandro [56], H.M. Alfanda [6], R. Alfaro Molina [67], B. Ali [16], A. Alici [26], N. Alizadehvandchali [115], A. Alkin [33], J. Alme [21], G. Alocco [52], T. Alt [64], A.R. Altamura [50], I. Altsybeev [95], M.N. Anaam [6], C. Andrei [46], N. Andreou [114], A. Andronic [137], V. Anguelov [94], F. Antinori [54], P. Antonioli [51], N. Apadula [74], L. Aphecetche [103], H. Appelshäuser [64], C. Arata [73], S. Arcelli [26], M. Aresti [23], R. Arnaldi [56], J.G.M.C.A. Arneiro [110], I.C. Arsene [20], M. Arslandok [139], A. Augustinus [33], R. Averbeck [97], M.D. Azmi[16], H. Baba[123], A. Badalà [53], J. Bae [104], Y.W. Baek [41], X. Bai [119], R. Bailhache [64], Y. Bailung [48], A. Balbino [30], A. Baldisseri [129], B. Balis [2], D. Banerjee [4], Z. Banoo [91], R. Barbera [27], F. Barile [32], L. Barioglio [95], M. Barlou[78], B. Barman[42], G.G. Barnaföldi [138], L.S. Barnby [85], V. Barret [126], L. Barreto [110], C. Bartels [118], K. Barth [33], E. Bartsch [64], N. Bastid [126], S. Basu [75], G. Batigne [103], D. Battistini [95], B. Batyunya [143], D. Bauri[47], J.L. Bazo Alba [101], I.G. Bearden [83], C. Beattie [139], P. Becht [97], D. Behera [48], I. Belikov [128], A.D.C. Bell Hechavarria [137], F. Bellini [26], R. Bellwied [115], S. Belokurova [142], Y.A.V. Beltran [45], G. Bencedi [138], S. Beole [25], Y. Berdnikov [142], A. Berdnikova [94], L. Bergmann [94], M.G. Besoiu [63], L. Betev [33], P.P. Bhaduri [134], A. Bhasin [91], M.A. Bhat [4], B. Bhattacharjee [42], L. Bianchi [25], N. Bianchi [49], J. Bielčík [36], J. Bielčíková [86], J. Biernat [107], A.P. Bigot [128], A. Bilandzic [95], G. Biro [138], S. Biswas [4], N. Bize [103], J.T. Blair [108], D. Blau [142], M.B. Blidaru [97], N. Bluhme[39], C. Blume [64], G. Boca [22,55], F. Bock [87], T. Bodova [21], A. Bogdanov[142], S. Boi [23], J. Bok [58], L. Boldizsár [138], M. Bombara [38], P.M. Bond [33], G. Bonomi [133,55], H. Borel [129], A. Borissov [142], A.G. Borquez Carcamo [94], H. Bossi [139], E. Botta [25], Y.E.M. Bouziani [64], L. Bratrud [64], P. Braun-Munzinger [97], M. Bregant [110], M. Broz [36], G.E. Bruno [96,32], M.D. Buckland [24], D. Budnikov [142], H. Buesching [64], S. Bufalino [30], P. Buhler [102], N. Burmasov [142], Z. Buthelezi [68,122], A. Bylinkin [21], S.A. Bysiak[107], M. Cai [6], H. Caines [139], A. Caliva [29], E. Calvo Villar [101], J.M.M. Camacho [109], P. Camerini [24], F.D.M. Canedo [110], M. Carabas [125], A.A. Carballo [33], F. Carnesecchi [33], R. Caron [127], L.A.D. Carvalho [110], J. Castillo Castellanos [129], F. Catalano [33,25], C. Ceballos Sanchez [143], I. Chakaberia [74], P. Chakraborty [47], S. Chandra [134], S. Chapeland [33], M. Chartier [118], S. Chattopadhyay [134], S. Chattopadhyay [99], T.G. Chavez [45], T. Cheng [97,6], C. Cheshkov [127], B. Cheynis [127], V. Chibante Barroso [33], D.D. Chinellato [111], E.S. Chizzali [I,95], J. Cho [58], S. Cho [58], P. Chochula [33], D. Choudhury[42], P. Christakoglou [84], C.H. Christensen [83], P. Christiansen [75], T. Chujo [124], M. Ciacco [30], C. Cicalo [52], F. Cindolo [51], M.R. Ciupek[97], G. Clai[II,51], F. Colamaria [50], J.S. Colburn[100], D. Colella [96,32], M. Colocci [26], M. Concas [III,33], G. Conesa Balbastre [73], Z. Conesa del Valle [130], G. Contin [24], J.G. Contreras [36], M.L. Coquet [129], P. Cortese [132,56], M.R. Cosentino [112], F. Costa [33], S. Costanza [22,55], C. Cot [130], J. Crkovská [94], P. Crochet [126], R. Cruz-Torres [74], P. Cui [6], A. Dainese [54], M.C. Danisch [94], A. Danu [63], P. Das [80], P. Das [4], S. Das [4], A.R. Dash [137], S. Dash [47], R.M.H. David[45], A. De Caro [29], G. de Cataldo [50], J. de Cuveland[39], A. De Falco [23], D. De Gruttola [29], N. De Marco [56], C. De Martin [24], S. De Pasquale [29], R. Deb [133], R. Del Grande [95], L. Dello Stritto [29], W. Deng [6], P. Dhankher [19], D. Di Bari [32], A. Di Mauro [33], B. Diab [129], R.A. Diaz [143,7], T. Dietel [113], Y. Ding [6], J. Ditzel [64], R. Divià [33], D.U. Dixit [19], Ø. Djuvsland[21], U. Dmitrieva [142], A. Dobrin [63], B. Dönigus [64], J.M. Dubinski [135], A. Dubla [97], S. Dudi [90], P. Dupieux [126], M. Durkac[106], N. Dzalaiova[13], T.M. Eder [137], R.J. Ehlers [74], F. Eisenhut [64], R. Ejima[92], D. Elia [50], B. Erazmus [103], F. Ercolessi [26], B. Espagnon [130], G. Eulisse [33], D. Evans [100], S. Evdokimov [142], L. Fabbietti [95], M. Faggin [28], J. Faivre [73], F. Fan [6], W. Fan [74], A. Fantoni [49], M. Fasel [87], A. Feliciello [56], G. Feofilov [142], A. Fernández Téllez [45], L. Ferrandi [110], M.B. Ferrer [33], A. Ferrero [129], C. Ferrero [56], A. Ferretti [25], V.J.G. Feuillard [94], V. Filova [36], D. Finogeev [142], F.M. Fionda [52], E. Flatland[33], F. Flor [115], A.N. Flores [108], S. Foertsch [68], I. Fokin [94], S. Fokin [142], E. Fragiacomo [57], E. Frajna [138], U. Fuchs [33], N. Funicello [29], C. Furget [73], A. Furs [142], T. Fusayasu [98], J.J. Gaardhøje [83], M. Gagliardi [25], A.M. Gago [101], T. Gahlaut[47], C.D. Galvan [109], D.R. Gangadharan [115], P. Ganoti [78], C. Garabatos [97], A.T. Garcia [130], J.R.A. Garcia [45], E. Garcia-Solis [9], C. Gargiulo [33], P. Gasik [97], A. Gautam [117], M.B. Gay Ducati [66], M. Germain [103], A. Ghimouz[124], C. Ghosh[134], M. Giacalone [51], G. Gioachin [30], P. Giubellino [97,56], P. Giubilato [28], A.M.C. Glaenzer [129], P. Glässel [94], E. Glimos [121], D.J.Q. Goh[76], V. Gonzalez [136], P. Gordeev[142], M. Gorgon [2], K. Goswami [48], S. Gotovac[34], V. Grabski [67], L.K. Graczykowski [135], E. Grecka [86], A. Grelli [59], C. Grigoras [33], V. Grigoriev [142], S. Grigoryan [143,1], F. Grosa [33], J.F. Grosse-Oetringhaus [33], R. Grosso [97], D. Grund [36], N.A. Grunwald[94], G.G. Guardiano [111], R. Guernane [73], M. Guilbaud [103], K. Gulbrandsen [83], T. Gündem [64], T. Gunji [123],

W. Guo [6], A. Gupta [91], R. Gupta [91], R. Gupta [48], S.P. Guzman [45], K. Gwizdziel [135], L. Gyulai [138], C. Hadjidakis [130], F.U. Haider [91], S. Haidlova [36], H. Hamagaki [76], A. Hamdi [74], Y. Han [140], B.G. Hanley [136], R. Hannigan [108], J. Hansen [75], M.R. Haque [135], J.W. Harris [139], A. Harton [9], H. Hassan [116], D. Hatzifotiadou [51], P. Hauer [43], L.B. Havener [139], S.T. Heckel [95], E. Hellbär [97], H. Helstrup [35], M. Hemmer [64], T. Herman [36], G. Herrera Corral [8], F. Herrmann[137], S. Herrmann [127], K.F. Hetland [35], B. Heybeck [64], H. Hillemanns [33], B. Hippolyte [128], F.W. Hoffmann [70], B. Hofman [59], G.H. Hong [140], M. Horst [95], A. Horzyk[2], Y. Hou [6], P. Hristov [33], C. Hughes [121], P. Huhn[64], L.M. Huhta [116], T.J. Humanic [88], A. Hutson [115], D. Hutter [39], R. Ilkaev[142], H. Ilyas [14], M. Inaba [124], G.M. Innocenti [33], M. Ippolitov [142], A. Isakov [84,86], T. Isidori [117], M.S. Islam [99], M. Ivanov [97], M. Ivanov[13], V. Ivanov [142], K.E. Iversen [75], M. Jablonski [2], B. Jacak [74], N. Jacazio [26], P.M. Jacobs [74], S. Jadlovska[106], J. Jadlovsky[106], S. Jaelani[82], C. Jahnke [110], M.J. Jakubowska [135], M.A. Janik [135], T. Janson[70], S. Ji [17], S. Jia [10], A.A.P. Jimenez [65], F. Jonas [87], D.M. Jones [118], J.M. Jowett [33,97], J. Jung [64], M. Jung [64], A. Junique [33], A. Jusko [100], M.J. Kabus [33,135], J. Kaewjai[105], P. Kalinak [60], A.S. Kalteyer [97], A. Kalweit [33], V. Kaplin [142], A. Karasu Uysal [72], D. Karatovic [89], O. Karavichev [142], T. Karavicheva [142], P. Karczmarczyk [135], E. Karpechev [142], U. Kebschull [70], R. Keidel [141], D.L.D. Keijdener[59], M. Keil [33], B. Ketzer [43], S.S. Khade [48], A.M. Khan [119], S. Khan [16], A. Khanzadeev [142], Y. Kharlov [142], A. Khatun [117], A. Khuntia [36], B. Kileng [35], B. Kim [104], C. Kim [17], D.J. Kim [116], E.J. Kim [69], J. Kim [140], J.S. Kim [41], J. Kim [58], J. Kim [69], M. Kim [19], S. Kim [18], T. Kim [140], K. Kimura [92], S. Kirsch [64], I. Kisel [39], S. Kiselev [142], A. Kisiel [135], J.P. Kitowski [2], J.L. Klay [5], J. Klein [33], S. Klein [74], C. Klein-Bösing [137], M. Kleiner [64], T. Klemenz [95], A. Kluge [33], A.G. Knospe [115], C. Kobdaj [105], T. Kollegger[97], A. Kondratyev [143], N. Kondratyeva [142], E. Kondratyuk [142], J. Konig [64], S.A. Konigstorfer [95], P.J. Konopka [33], G. Kornakov [135], M. Korwieser [95], S.D. Koryciak [2], A. Kotliarov [86], V. Kovalenko [142], M. Kowalski [107], V. Kozhuharov [37], I. Králik [60], A. Kravčáková [38], L. Krcal [33,39], M. Krivda [100,60], F. Krizek [86], K. Krizkova Gajdosova [33], M. Kroesen [94], M. Krüger [64], D.M. Krupova [36], E. Kryshen [142], V. Kučera [58], C. Kuhn [128], P.G. Kuijer [84], T. Kumaoka[124], D. Kumar[134], L. Kumar [90], N. Kumar[90], S. Kumar [32], S. Kundu [33], P. Kurashvili [79], A. Kurepin [142], A.B. Kurepin [142], A. Kuryakin [142], S. Kushpil [86], V. Kuskov[142], M.J. Kweon [58], Y. Kwon [140], S.L. La Pointe [39], P. La Rocca [27], A. Lakrathok[105], M. Lamanna [33], A.R. Landou [73,114], R. Langoy [120], P. Larionov [33], E. Laudi [33], L. Lautner [33,95], R. Lavicka [102], R. Lea [133,55], H. Lee [104], I. Legrand [46], G. Legras [137], J. Lehrbach [39], T.M. Lelek[2], R.C. Lemmon [85], I. León Monzón [109], M.M. Lesch [95], E.D. Lesser [19], P. Lévai [138], X. Li[10], J. Lien [120], R. Lietava [100], I. Likmeta [115], B. Lim [25], S.H. Lim [17], V. Lindenstruth [39], A. Lindner[46], C. Lippmann [97], D.H. Liu [6], J. Liu [118], G.S.S. Liveraro [111], I.M. Lofnes [21], C. Loizides [87], S. Lokos [107], J. Lomker [59], P. Loncar [34], X. Lopez [126], E. López Torres [7], P. Lu [97,119], F.V. Lugo [67], J.R. Luhder [137], M. Lunardon [28], G. Luparello [57], Y.G. Ma [40], M. Mager [33], A. Maire [128], M.V. Makariev [37], M. Malaev [142], G. Malfattore [26], N.M. Malik [91], Q.W. Malik[20], S.K. Malik [91], L. Malinina [VI,143], D. Mallick [130,80], N. Mallick [48], G. Mandaglio [31,53], S.K. Mandal [79], V. Manko [142], F. Manso [126], V. Manzari [50], Y. Mao [6], R.W. Marcjan [2], G.V. Margagliotti [24], A. Margotti [51], A. Marín [97], C. Markert [108], P. Martinengo [33], M.I. Martínez [45], G. Martínez García [103], M.P.P. Martins [110], S. Masciocchi [97], M. Masera [25], A. Masoni [52], L. Massacrier [130], O. Massen [59], A. Mastroserio [131,50], O. Matonoha [75], S. Mattiazzo [28], A. Matyja [107], C. Mayer [107], A.L. Mazuecos [33], F. Mazzaschi [25], M. Mazzilli [33], J.E. Mdhluli [122], Y. Melikyan [44], A. Menchaca-Rocha [67], J.E.M. Mendez [65], E. Meninno [102,29], A.S. Menon [115], M. Meres [13], S. Mhlanga[113,68], Y. Miake[124], L. Micheletti [33], D.L. Mihaylov [95], K. Mikhaylov [143,142], A.N. Mishra [138], D. Miśkowiec [97], A. Modak [4], B. Mohanty[80], M. Mohisin Khan[IV,16], M.A. Molander [44], S. Monira [135], C. Mordasini [116], D.A. Moreira De Godoy [137], I. Morozov [142], A. Morsch [33], T. Mrnjavac [33], V. Muccifora [49], S. Muhuri [134], J.D. Mulligan [74], A. Mulliri[23], M.G. Munhoz [110], R.H. Munzer [64], H. Murakami [123], S. Murray [113], L. Musa [33], J. Musinsky [60], J.W. Myrcha [135], B. Naik [122], A.I. Nambrath [19], B.K. Nandi [47], R. Nania [51], E. Nappi [50], A.F. Nassirpour [18], A. Nath [94], C. Nattrass [121], M.N. Naydenov [37], A. Neagu[20], A. Negru[125], E. Nekrasova[142], L. Nellen [65], R. Nepeivoda [75], S. Nese [20], G. Neskovic [39], N. Nicassio [50], B.S. Nielsen [83], E.G. Nielsen [83], S. Nikolaev [142], S. Nikulin [142], V. Nikulin [142], F. Noferini [51], S. Noh [12], P. Nomokonov [143], J. Norman [118], N. Novitzky [87], P. Nowakowski [135], A. Nyanin [142], J. Nystrand [21], M. Ogino [76], S. Oh [18], A. Ohlson [75], V.A. Okorokov [142], J. Oleniacz [135], A.C. Oliveira Da Silva [121], A. Onnerstad [116], C. Oppedisano [56], A. Ortiz Velasquez [65], J. Otwinowski [107], M. Oya[92], K. Oyama [76], Y. Pachmayer [94], S. Padhan [47], D. Pagano [133,55], G. Paić [65], A. Palasciano [50], S. Panebianco [129],

H. Park [124], H. Park [104], J. Park [58], J.E. Parkkila [33], Y. Patley [47], R.N. Patra[91], B. Paul [23], H. Pei [6], T. Peitzmann [59], X. Peng [11], M. Pennisi [25], S. Perciballi [25], D. Peresunko [142], G.M. Perez [7], Y. Pestov[142], V. Petrov [142], M. Petrovici [46], R.P. Pezzi [103,66], S. Piano [57], M. Pikna [13], P. Pillot [103], O. Pinazza [51,33], L. Pinsky[115], C. Pinto [95], S. Pisano [49], M. Płoskoń [74], M. Planinic[89], F. Pliquett[64], M.G. Poghosyan [87], B. Polichtchouk [142], S. Politano [30], N. Poljak [89], A. Pop [46], S. Porteboeuf-Houssais [126], V. Pozdniakov [143], I.Y. Pozos [45], K.K. Pradhan [48], S.K. Prasad [4], S. Prasad [48], R. Preghenella [51], F. Prino [56], C.A. Pruneau [136], I. Pshenichnov [142], M. Puccio [33], S. Pucillo [25], Z. Pugelova[106], S. Qiu [84], L. Quaglia [25], S. Ragoni [15], A. Rai [139], A. Rakotozafindrabe [129], L. Ramello [132,56], F. Rami [128], S.A.R. Ramirez [45], T.A. Rancien[73], M. Rasa [27], S.S. Räsänen [44], R. Rath [51], M.P. Rauch [21], I. Ravasenga [84], K.F. Read [87,121], C. Reckziegel [112], A.R. Redelbach [39], K. Redlich [V,79], C.A. Reetz [97], A. Rehman[21], F. Reidt [33], H.A. Reme-Ness [35], Z. Rescakova[38], K. Reygers [94], A. Riabov [142], V. Riabov [142], R. Ricci [29], M. Richter [20], A.A. Riedel [95], W. Riegler [33], A.G. Riffero [25], C. Ristea [63], M.V. Rodriguez [33], M. Rodríguez Cahuantzi [45], K. Røed [20], R. Rogalev [142], E. Rogochaya [143], T.S. Rogoschinski [64], D. Rohr [33], D. Röhrich [21], P.F. Rojas[45], S. Rojas Torres [36], P.S. Rokita [135], G. Romanenko [26], F. Ronchetti [49], A. Rosano [31,53], E.D. Rosas[65], K. Roslon [135], A. Rossi [54], A. Roy [48], S. Roy [47], N. Rubini [26], D. Ruggiano [135], R. Rui [24], P.G. Russek [2], R. Russo [84], A. Rustamov [81], E. Ryabinkin [142], Y. Ryabov [142], A. Rybicki [107], H. Rytkonen [116], J. Ryu [17], W. Rzesa [135], O.A.M. Saarimaki [44], S. Sadhu [32], S. Sadovsky [142], J. Saetre [21], K. Šafařík [36], P. Saha[42], S.K. Saha [4], S. Saha [80], B. Sahoo [47], B. Sahoo [48], R. Sahoo [48], S. Sahoo[61], D. Sahu [48], P.K. Sahu [61], J. Saini [134], K. Sajdakova[38], S. Sakai [124], M.P. Salvan [97], S. Sambyal [91], D. Samitz [102], I. Sanna [33,95], T.B. Saramela[110], P. Sarma [42], V. Sarritzu [23], V.M. Sarti [95], M.H.P. Sas [33], S. Sawan[80], J. Schambach [87], H.S. Scheid [64], C. Schiaua [46], R. Schicker [94], F. Schlepper [94], A. Schmah[97], C. Schmidt [97], H.R. Schmidt[93], M.O. Schmidt [33], M. Schmidt[93], N.V. Schmidt [87], A.R. Schmier [121], R. Schotter [128], A. Schröter [39], J. Schukraft [33], K. Schweda [97], G. Scioli [26], E. Scomparin [56], J.E. Seger [15], Y. Sekiguchi[123], D. Sekihata [123], M. Selina [84], I. Selyuzhenkov [97], S. Senyukov [128], J.J. Seo [94,58], D. Serebryakov [142], L. Šerkšnytė [95], A. Sevcenco [63], T.J. Shaba [68], A. Shabetai [103], R. Shahoyan[33], A. Shangaraev [142], A. Sharma[90], B. Sharma [91], D. Sharma [47], H. Sharma [54], M. Sharma [91], S. Sharma [76], S. Sharma [91], U. Sharma [91], A. Shatat [130], O. Sheibani[115], K. Shigaki [92], M. Shimomura[77], J. Shin[12], S. Shirinkin [142], Q. Shou [40], Y. Sibiriak [142], S. Siddhanta [52], T. Siemiarczuk [79], T.F. Silva [110], D. Silvermyr [75], T. Simantathammakul[105], R. Simeonov [37], B. Singh[91], B. Singh [95], K. Singh [48], R. Singh [80], R. Singh [91], R. Singh [48], S. Singh [16], V.K. Singh [134], V. Singhal [134], T. Sinha [99], B. Sitar [13], M. Sitta [132,56], T.B. Skaali[20], G. Skorodumovs [94], M. Slupecki [44], N. Smirnov [139], R.J.M. Snellings [59], E.H. Solheim [20], J. Song [17], C. Sonnabend [33,97], F. Soramel [28], A.B. Soto-hernandez [88], R. Spijkers [84], I. Sputowska [107], J. Staa [75], J. Stachel [94], I. Stan [63], P.J. Steffanic [121], S.F. Stiefelmaier [94], D. Stocco [103], I. Storehaug [20], P. Stratmann [137], S. Strazzi [26], A. Sturniolo [31,53], C.P. Stylianidis[84], A.A.P. Suaide [110], C. Suire [130], M. Sukhanov [142], M. Suljic [33], R. Sultanov [142], V. Sumberia [91], S. Sumowidagdo [82], S. Swain[61], I. Szarka [13], M. Szymkowski [135], S.F. Taghavi [95], G. Taillepied [97], J. Takahashi [111], G.J. Tambave [80], S. Tang [6], Z. Tang [119], J.D. Tapia Takaki [117], N. Tapus[125], L.A. Tarasovicova [137], M.G. Tarzila [46], G.F. Tassielli [32], A. Tauro [33], G. Tejeda Muñoz [45], A. Telesca [33], L. Terlizzi [25], C. Terrevoli [115], S. Thakur [4], D. Thomas [108], A. Tikhonov [142], N. Tiltmann [33,137], A.R. Timmins [115], M. Tkacik[106], T. Tkacik [106], A. Toia [64], R. Tokumoto[92], K. Tomohiro[92], N. Topilskaya [142], M. Toppi [49], T. Tork [130], P.V. Torres[65], V.V. Torres [103], A.G. Torres Ramos [32], A. Trifiró [31,53], A.S. Triolo [33,31,53], S. Tripathy [51], T. Tripathy [47], S. Trogolo [33], V. Trubnikov [3], W.H. Trzaska [116], T.P. Trzcinski [135], A. Tumkin [142], R. Turrisi [54], T.S. Tveter [20], K. Ullaland [21], B. Ulukutlu [95], A. Uras [127], G.L. Usai [23], M. Vala[38], N. Valle [22], L.V.R. van Doremalen[59], M. van Leeuwen [84], C.A. van Veen [94], R.J.G. van Weelden [84], P. Vande Vyvre [33], D. Varga [138], Z. Varga [138], M. Vasileiou [78], A. Vasiliev [142], O. Vázquez Doce [49], O. Vazquez Rueda [115], V. Vechernin [142], E. Vercellin [25], S. Vergara Limón[45], R. Verma[47], L. Vermunt [97], R. Vértesi [138], M. Verweij [59], L. Vickovic[34], Z. Vilakazi[122], O. Villalobos Baillie [100], A. Villani [24], A. Vinogradov [142], T. Virgili [29], M.M.O. Virta [116], V. Vislavicius[75], A. Vodopyanov [143], B. Volkel [33], M.A. Völkl [94], K. Voloshin[142], S.A. Voloshin [136], G. Volpe [32], B. von Haller [33], I. Vorobyev [95], N. Vozniuk [142], J. Vrláková [38], J. Wan[40], C. Wang [40], D. Wang[40], Y. Wang [40], Y. Wang [6], A. Wegrzynek [33], F.T. Weiglhofer[39], S.C. Wenzel [33], J.P. Wessels [137], S.L. Weyhmiller [139], J. Wiechula [64], J. Wikne [20], G. Wilk [79], J. Wilkinson [97], G.A. Willems [137], B. Windelband [94], M. Winn [129], J.R. Wright [108], W. Wu[40], Y. Wu [119], R. Xu [6], A. Yadav [43], A.K. Yadav [134],

S. Yalcin [72], Y. Yamaguchi [92], S. Yang[21], S. Yano [92], E.R. Yeats[19], Z. Yin [6], I.-K. Yoo [17], J.H. Yoon [58], H. Yu[12], S. Yuan[21], A. Yuncu [94], V. Zaccolo [24], C. Zampolli [33], F. Zanone [94], N. Zardoshti [33], A. Zarochentsev [142], P. Závada [62], N. Zaviyalov[142], M. Zhalov [142], B. Zhang [6], C. Zhang [129], L. Zhang [40], S. Zhang [40], X. Zhang [6], Y. Zhang[119], Z. Zhang [6], M. Zhao [10], V. Zherebchevskii [142], Y. Zhi[10], D. Zhou [6], Y. Zhou [83], J. Zhu [97,6], Y. Zhu[6], S.C. Zugravel [56], N. Zurlo [133,55]

## Affiliation Notes

[I] Also at: Max-Planck-Institut für Physik, Munich, Germany
[II] Also at: Italian National Agency for New Technologies, Energy and Sustainable Economic Development (ENEA), Bologna, Italy
[III] Also at: Dipartimento DET del Politecnico di Torino, Turin, Italy
[IV] Also at: Department of Applied Physics, Aligarh Muslim University, Aligarh, India
[V] Also at: Institute of Theoretical Physics, University of Wroclaw, Poland
[VI] Also at: An institution covered by a cooperation agreement with CERN

## Collaboration Institutes

[1] A.I. Alikhanyan National Science Laboratory (Yerevan Physics Institute) Foundation, Yerevan, Armenia
[2] AGH University of Krakow, Cracow, Poland
[3] Bogolyubov Institute for Theoretical Physics, National Academy of Sciences of Ukraine, Kiev, Ukraine
[4] Bose Institute, Department of Physics and Centre for Astroparticle Physics and Space Science (CAPSS), Kolkata, India
[5] California Polytechnic State University, San Luis Obispo, California, United States
[6] Central China Normal University, Wuhan, China
[7] Centro de Aplicaciones Tecnológicas y Desarrollo Nuclear (CEADEN), Havana, Cuba
[8] Centro de Investigación y de Estudios Avanzados (CINVESTAV), Mexico City and Mérida, Mexico
[9] Chicago State University, Chicago, Illinois, United States
[10] China Institute of Atomic Energy, Beijing, China
[11] China University of Geosciences, Wuhan, China
[12] Chungbuk National University, Cheongju, Republic of Korea
[13] Comenius University Bratislava, Faculty of Mathematics, Physics and Informatics, Bratislava, Slovak Republic
[14] COMSATS University Islamabad, Islamabad, Pakistan
[15] Creighton University, Omaha, Nebraska, United States
[16] Department of Physics, Aligarh Muslim University, Aligarh, India
[17] Department of Physics, Pusan National University, Pusan, Republic of Korea
[18] Department of Physics, Sejong University, Seoul, Republic of Korea
[19] Department of Physics, University of California, Berkeley, California, United States
[20] Department of Physics, University of Oslo, Oslo, Norway
[21] Department of Physics and Technology, University of Bergen, Bergen, Norway
[22] Dipartimento di Fisica, Università di Pavia, Pavia, Italy
[23] Dipartimento di Fisica dell'Università and Sezione INFN, Cagliari, Italy
[24] Dipartimento di Fisica dell'Università and Sezione INFN, Trieste, Italy
[25] Dipartimento di Fisica dell'Università and Sezione INFN, Turin, Italy
[26] Dipartimento di Fisica e Astronomia dell'Università and Sezione INFN, Bologna, Italy
[27] Dipartimento di Fisica e Astronomia dell'Università and Sezione INFN, Catania, Italy
[28] Dipartimento di Fisica e Astronomia dell'Università and Sezione INFN, Padova, Italy
[29] Dipartimento di Fisica 'E.R. Caianiello' dell'Università and Gruppo Collegato INFN, Salerno, Italy
[30] Dipartimento DISAT del Politecnico and Sezione INFN, Turin, Italy
[31] Dipartimento di Scienze MIFT, Università di Messina, Messina, Italy
[32] Dipartimento Interateneo di Fisica 'M. Merlin' and Sezione INFN, Bari, Italy
[33] European Organization for Nuclear Research (CERN), Geneva, Switzerland
[34] Faculty of Electrical Engineering, Mechanical Engineering and Naval Architecture, University of Split, Split, Croatia
[35] Faculty of Engineering and Science, Western Norway University of Applied Sciences, Bergen, Norway
[36] Faculty of Nuclear Sciences and Physical Engineering, Czech Technical University in Prague, Prague, Czech Republic
[37] Faculty of Physics, Sofia University, Sofia, Bulgaria

[38] Faculty of Science, P.J. Šafárik University, Košice, Slovak Republic
[39] Frankfurt Institute for Advanced Studies, Johann Wolfgang Goethe-Universität Frankfurt, Frankfurt, Germany
[40] Fudan University, Shanghai, China
[41] Gangneung-Wonju National University, Gangneung, Republic of Korea
[42] Gauhati University, Department of Physics, Guwahati, India
[43] Helmholtz-Institut für Strahlen- und Kernphysik, Rheinische Friedrich-Wilhelms-Universität Bonn, Bonn, Germany
[44] Helsinki Institute of Physics (HIP), Helsinki, Finland
[45] High Energy Physics Group, Universidad Autónoma de Puebla, Puebla, Mexico
[46] Horia Hulubei National Institute of Physics and Nuclear Engineering, Bucharest, Romania
[47] Indian Institute of Technology Bombay (IIT), Mumbai, India
[48] Indian Institute of Technology Indore, Indore, India
[49] INFN, Laboratori Nazionali di Frascati, Frascati, Italy
[50] INFN, Sezione di Bari, Bari, Italy
[51] INFN, Sezione di Bologna, Bologna, Italy
[52] INFN, Sezione di Cagliari, Cagliari, Italy
[53] INFN, Sezione di Catania, Catania, Italy
[54] INFN, Sezione di Padova, Padova, Italy
[55] INFN, Sezione di Pavia, Pavia, Italy
[56] INFN, Sezione di Torino, Turin, Italy
[57] INFN, Sezione di Trieste, Trieste, Italy
[58] Inha University, Incheon, Republic of Korea
[59] Institute for Gravitational and Subatomic Physics (GRASP), Utrecht University/Nikhef, Utrecht, Netherlands
[60] Institute of Experimental Physics, Slovak Academy of Sciences, Košice, Slovak Republic
[61] Institute of Physics, Homi Bhabha National Institute, Bhubaneswar, India
[62] Institute of Physics of the Czech Academy of Sciences, Prague, Czech Republic
[63] Institute of Space Science (ISS), Bucharest, Romania
[64] Institut für Kernphysik, Johann Wolfgang Goethe-Universität Frankfurt, Frankfurt, Germany
[65] Instituto de Ciencias Nucleares, Universidad Nacional Autónoma de México, Mexico City, Mexico
[66] Instituto de Física, Universidade Federal do Rio Grande do Sul (UFRGS), Porto Alegre, Brazil
[67] Instituto de Física, Universidad Nacional Autónoma de México, Mexico City, Mexico
[68] iThemba LABS, National Research Foundation, Somerset West, South Africa
[69] Jeonbuk National University, Jeonju, Republic of Korea
[70] Johann-Wolfgang-Goethe Universität Frankfurt Institut für Informatik, Fachbereich Informatik und Mathematik, Frankfurt, Germany
[71] Korea Institute of Science and Technology Information, Daejeon, Republic of Korea
[72] KTO Karatay University, Konya, Turkey
[73] Laboratoire de Physique Subatomique et de Cosmologie, Université Grenoble-Alpes, CNRS-IN2P3, Grenoble, France
[74] Lawrence Berkeley National Laboratory, Berkeley, California, United States
[75] Lund University Department of Physics, Division of Particle Physics, Lund, Sweden
[76] Nagasaki Institute of Applied Science, Nagasaki, Japan
[77] Nara Women's University (NWU), Nara, Japan
[78] National and Kapodistrian University of Athens, School of Science, Department of Physics , Athens, Greece
[79] National Centre for Nuclear Research, Warsaw, Poland
[80] National Institute of Science Education and Research, Homi Bhabha National Institute, Jatni, India
[81] National Nuclear Research Center, Baku, Azerbaijan
[82] National Research and Innovation Agency - BRIN, Jakarta, Indonesia
[83] Niels Bohr Institute, University of Copenhagen, Copenhagen, Denmark
[84] Nikhef, National institute for subatomic physics, Amsterdam, Netherlands
[85] Nuclear Physics Group, STFC Daresbury Laboratory, Daresbury, United Kingdom
[86] Nuclear Physics Institute of the Czech Academy of Sciences, Husinec-Řež, Czech Republic
[87] Oak Ridge National Laboratory, Oak Ridge, Tennessee, United States
[88] Ohio State University, Columbus, Ohio, United States
[89] Physics department, Faculty of science, University of Zagreb, Zagreb, Croatia
[90] Physics Department, Panjab University, Chandigarh, India

[91] Physics Department, University of Jammu, Jammu, India
[92] Physics Program and International Institute for Sustainability with Knotted Chiral Meta Matter (SKCM2), Hiroshima University, Hiroshima, Japan
[93] Physikalisches Institut, Eberhard-Karls-Universität Tübingen, Tübingen, Germany
[94] Physikalisches Institut, Ruprecht-Karls-Universität Heidelberg, Heidelberg, Germany
[95] Physik Department, Technische Universität München, Munich, Germany
[96] Politecnico di Bari and Sezione INFN, Bari, Italy
[97] Research Division and ExtreMe Matter Institute EMMI, GSI Helmholtzzentrum für Schwerionenforschung GmbH, Darmstadt, Germany
[98] Saga University, Saga, Japan
[99] Saha Institute of Nuclear Physics, Homi Bhabha National Institute, Kolkata, India
[100] School of Physics and Astronomy, University of Birmingham, Birmingham, United Kingdom
[101] Sección Física, Departamento de Ciencias, Pontificia Universidad Católica del Perú, Lima, Peru
[102] Stefan Meyer Institut für Subatomare Physik (SMI), Vienna, Austria
[103] SUBATECH, IMT Atlantique, Nantes Université, CNRS-IN2P3, Nantes, France
[104] Sungkyunkwan University, Suwon City, Republic of Korea
[105] Suranaree University of Technology, Nakhon Ratchasima, Thailand
[106] Technical University of Košice, Košice, Slovak Republic
[107] The Henryk Niewodniczanski Institute of Nuclear Physics, Polish Academy of Sciences, Cracow, Poland
[108] The University of Texas at Austin, Austin, Texas, United States
[109] Universidad Autónoma de Sinaloa, Culiacán, Mexico
[110] Universidade de São Paulo (USP), São Paulo, Brazil
[111] Universidade Estadual de Campinas (UNICAMP), Campinas, Brazil
[112] Universidade Federal do ABC, Santo Andre, Brazil
[113] University of Cape Town, Cape Town, South Africa
[114] University of Derby, Derby, United Kingdom
[115] University of Houston, Houston, Texas, United States
[116] University of Jyväskylä, Jyväskylä, Finland
[117] University of Kansas, Lawrence, Kansas, United States
[118] University of Liverpool, Liverpool, United Kingdom
[119] University of Science and Technology of China, Hefei, China
[120] University of South-Eastern Norway, Kongsberg, Norway
[121] University of Tennessee, Knoxville, Tennessee, United States
[122] University of the Witwatersrand, Johannesburg, South Africa
[123] University of Tokyo, Tokyo, Japan
[124] University of Tsukuba, Tsukuba, Japan
[125] University Politehnica of Bucharest, Bucharest, Romania
[126] Université Clermont Auvergne, CNRS/IN2P3, LPC, Clermont-Ferrand, France
[127] Université de Lyon, CNRS/IN2P3, Institut de Physique des 2 Infinis de Lyon, Lyon, France
[128] Université de Strasbourg, CNRS, IPHC UMR 7178, F-67000 Strasbourg, France, Strasbourg, France
[129] Université Paris-Saclay, Centre d'Etudes de Saclay (CEA), IRFU, Départment de Physique Nucléaire (DPhN), Saclay, France
[130] Université Paris-Saclay, CNRS/IN2P3, IJCLab, Orsay, France
[131] Università degli Studi di Foggia, Foggia, Italy
[132] Università del Piemonte Orientale, Vercelli, Italy
[133] Università di Brescia, Brescia, Italy
[134] Variable Energy Cyclotron Centre, Homi Bhabha National Institute, Kolkata, India
[135] Warsaw University of Technology, Warsaw, Poland
[136] Wayne State University, Detroit, Michigan, United States
[137] Westfälische Wilhelms-Universität Münster, Institut für Kernphysik, Münster, Germany
[138] Wigner Research Centre for Physics, Budapest, Hungary
[139] Yale University, New Haven, Connecticut, United States
[140] Yonsei University, Seoul, Republic of Korea
[141] Zentrum für Technologie und Transfer (ZTT), Worms, Germany
[142] Affiliated with an institute covered by a cooperation agreement with CERN
[143] Affiliated with an international laboratory covered by a cooperation agreement with CERN.